NANOIMPRINTED TRANSPARENT METAL ELECTRODES AND THEIR APPLICATIONS IN ORGANIC OPTOELECTRONIC DEVICES

by

Myung-Gyu Kang

A dissertation submitted in partial fulfillment
of the requirements for the degree of
Doctor of Philosophy
(Electrical Engineering)
in The University of Michigan
2009

Doctoral Committee:

   Associate Professor L Jay Guo, Chair
   Associate Professor Jinsang Kim
   Associate Professor Jamie Dean Phillips
   Assistant Professor Max Shtein

To my family: Your love and dedication made this possible

Acknowledgements

It is a great pleasure to thank those who made this thesis possible. First and foremost, I would like to show my gratitude to my advisor, Prof. L. Jay Guo, who has supported me throughout Ph. D study with his patience, encouragement and guidance. Without his supports, this thesis would not have been possible, and I can not thank him enough for what he has done for me in the past five years. I am also highly thankful to my committee members, Prof. Jinsang Kim, Prof. Jamie Phillips, and Prof. Max Shtein for their valuable suggestions throughout this study.

I would like to acknowledge all current and past nanogroup members, Phillip, Brandon, Carlos, Se Hyun, Tao, Yi-Hao, Sung-Liang, Hyoung Won, Abram, Hui Joon, Yazeed, Alex, Yi-Kuei, Prof. Xing Cheng, Dr. Chung-Yen Chao, Prof. Dawen Li, Dr, Larry Cheng for their kindness and help for my study. I would also like to acknowledge the staff and student members of Lurie Nanofabrication Facility and Solid State Laboratory for their kind help during my study. It was a great luck for me to work with wonderful facility and people. My special thanks go to Ting Xu in the Chinese Academy of Science and Dr. Sanghyun Lee for their help in simulation and experimental works for my thesis.

I am greatly indebted to my parents for their love and supports throughout my life. I also wish to thank my wife, Hoo-Hee for her love and sacrifice; and my beloved

sons, Phillip and Alex. Without my family's love and dedication, this thesis would not have been possible.

Lastly, I offer my regards and blessings to all of those who supported me in any respect during the completion of Ph. D study.

Table of Contents

List of Figures

List of Tables

ABSTRACT

NANOIMPRINTED TRANSPARENT METAL ELECTRODES AND THEIR APPLICATIONS IN ORGANIC OPTOELECTRONIC DEVICES

by

Myung-Gyu Kang

Chair: L Jay Guo

A new type of transparent and conductive electrode (TCE) in the form of a nanoscale periodically perforated metal mesh film by nanoimprint lithography (NIL) has been developed. The developed transparent metal electrodes have the characteristics of the high optical transmittance and electrical conductivity, a combination of properties that makes them suitable as a replacement for indium-doped tin oxide (ITO), a predominant choice as a TCE for organic optoelectronic device applications. Not only do metals provide different work functions, but also nanoscale metallic gratings exhibit unique optical properties due to the excitation of surface plasmon resonance (SPR), which can be exploited in specially designed solar cells to achieve enhanced light absorption. The future low-cost and high performance organic optoelectronic devices will need a TCE which should be available with low-cost and high mechanical stability, the properties

which ITO does not have. This work shows that transparent metal (e.g. Cu) electrode on flexible plastic substrate exhibits not only high transmittance and conductivity, but also a superior mechanical strength to compared ITO electrode.

Organic light emitting diodes (OLEDs) have been demonstrated using transparent Cu electrodes as a TCE. The electrical characteristic of the fabricated OLED is similar to that of the OLED using ITO electrode.

Organic solar cells (OSCs) have been demonstrated using transparent metal (Au, Ag, and Cu) electrodes as a TCE on both hard (glass) and soft (PET) substrates. The characteristics such as open circuit voltage (Voc), short circuit current density (Jsc), fill-factor (FF), and power conversion efficiency (PCE) are comparable to those of ITO device when high transparency metal electrodes were used. To demonstrate the possibility of PCE enhancement of OSCs using the developed metal electrode, OSCs have been fabricated with a periodic (220 nm) Ag grating electrode, acting as not only a transparent electrode but also to support surface plasmon modes with localized and concentrated light distribution. The absolute PCE enhancement of about 35 % for the device with an Ag electrode relative to the ITO reference device was achieved. It has also been demonstrated that the SPR enhances the external quantum efficiency (EQE) by about 2.5 times for the Ag device compared to the ITO device. The experimental results suggested that higher enhancement would be possible for a thinner organic layer. Therefore, the use of transparent metal electrodes as a TCE instead of ITO could help to realize low-cost, high performance, large-area, flexible organic optoelectronic devices such as OSCs and OLEDs.

Additionally, a number of fabrication methods based on metal transfer have been developed during this research, which have become useful techniques that can be used in

solar cell and other device fabrications.

Chapter 1

Introduction

Organic optoelectronic devices, specifically, organic light emitting diodes (OLEDs)[1-3] and organic solar cells (OSCs)[4] are promising for use in future flat-panel and flexible displays and as a renewable energy source, respectively. They have several advantages such as low cost, easy fabrication, and compatibility with flexible substrates over large areas, compared to their inorganic counterparts. In particular, OSCs are considered a promising source of clean and carbon-neutral energy as the issue of global warming from fossil fuel combustion continues to raise our concerns. However, their mass production has still yet to be achieved because of the low (4~5%) efficiency and durability of organic materials. OLED displays have already entered the display market with superb performance but much more expensive prices. Many researchers have been working on new efficient organic materials for organic optoelectronic device applications which might become available with improved properties and lower prices. However, very little research has been done on the transparent electrodes that these devices use for proper operation of OLEDs and OSCs.

1.1 Basic organic device structure

Figure 1-1 shows the basic organic device structure. It consists of a number of

organic semiconductor layers sandwiched between two electrodes. Most of the organic devices fabricated today use a thick, conductive metal layer as the rear electrode and a transparent, conductive electrode (TCE) as the front electrode, which receives (OSCs) or emits (OLEDs) light.
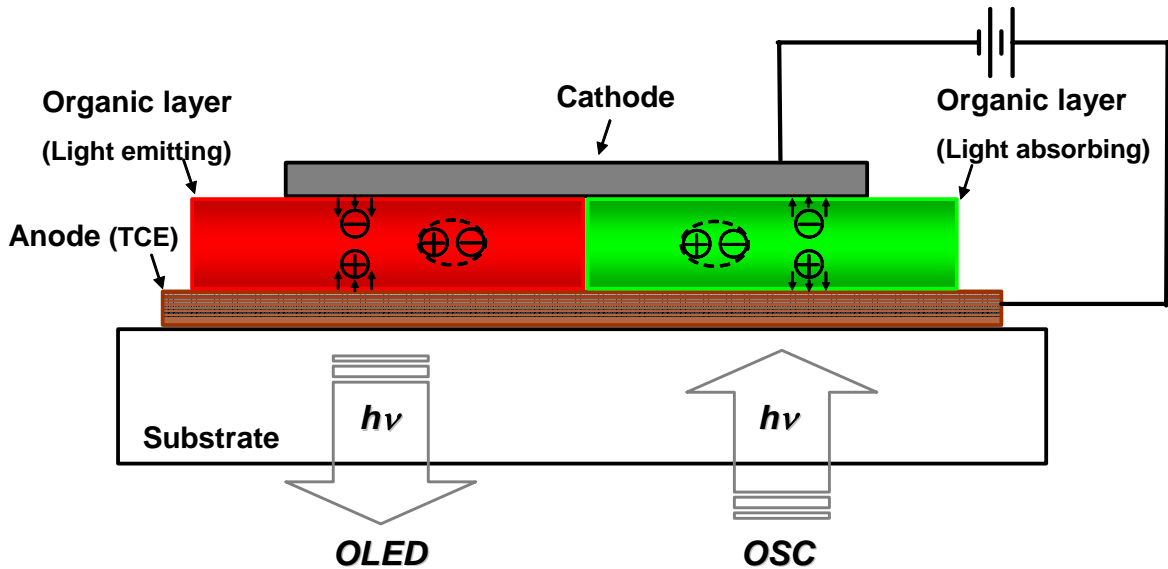
Figure 1-1 Basic organic device (OLED or OSC) structure

Transparent, conductive electrodes (TCEs) are very important components in any photosensitive optoelectronic devices such as OLEDs and OSCs. An ideal TCE must be highly transparent to allow the maximum amount of light through, and it must also be conductive to provide uniform electrical current distribution. In addition to these properties, it must be mechanically and chemically stable, and should not cause the degradation of the active materials it contacts in the device.

1.2 Transparent and conductive electrodes

In this section, commonly used transparent, conductive electrodes are reviewed, focusing on their optical, electrical, mechanical properties for the use in organic optoelectronic device applications.

1.2.1 Transparent conducting oxide semiconductors

For a material to be transparent in the visible range, it must not absorb light in this region. Thus, the optical band-gap of a material must be greater than about 3 eV. Transparent materials are generally insulators. For a material to be conductive, it must have sufficient free carriers (electrons or holes) like metals or highly doped semiconductors. Conductive materials are generally very opaque in visible range. Fortunately, there is a special class of semiconductors, called transparent conducting oxide semiconductors (TCOs), such as impurity doped In_2O_3, SnO_2, and ZnO. They have optical band-gaps greater than 3 eV, and carrier concentrations up to 10^{21} cm^{-3}, a combination of properties that makes them both highly transparent in the visible range and conductive.

Among these materials, tin-doped indium oxide (commonly called indium-tin-oxide, or ITO) (In_2O_3: Sn) has shown promise for use as TCE in display industry and optoelectronic devices. It is a highly doped degenerate semiconductor with optical band-gap above 3 eV; these features make it both transparent to wavelengths greater than approximately 400nm[5-9] and conductive. As a result, ITO is the most common material as a TCE, and shows good performance in organic optoelectronic devices such as OLEDs and OSCs. However, several aspects of ITO are far from optimum for such high

performance devices. First, the migration of indium and oxygen from ITO into organic semiconductors during the operation of the OLED causes device degradation[10, 11]. The electrical properties of ITO are sensitive to the condition of the film preparation[12, 13]. Its rough surface limits the efficiency of the hole injection as does its low work function, ~4.7 eV[14]. The typical sheet resistance of ITO, 20~80 $\Omega/\square$, is so high that it causes a voltage drop along the addressing line, which limits the operation of large area passive matrix OLED array[15]. It has been recently reported that ITO is not an optimum electrode for organic solar cell applications because the band structure of the ITO hinders efficient photocurrent generation[16]. Moreover, the poor mechanical stability of ITO can cause device failure when an ITO-coated flexible substrate is bent[17]. Figure 1-2 shows the SEM image of the commercial ITO electrode on PET substrate after bending test with a radius of ~15 mm. The poor mechanical stability as shown in Fig. 1-2 will make the ITO electrode not suitable for flexible applications.
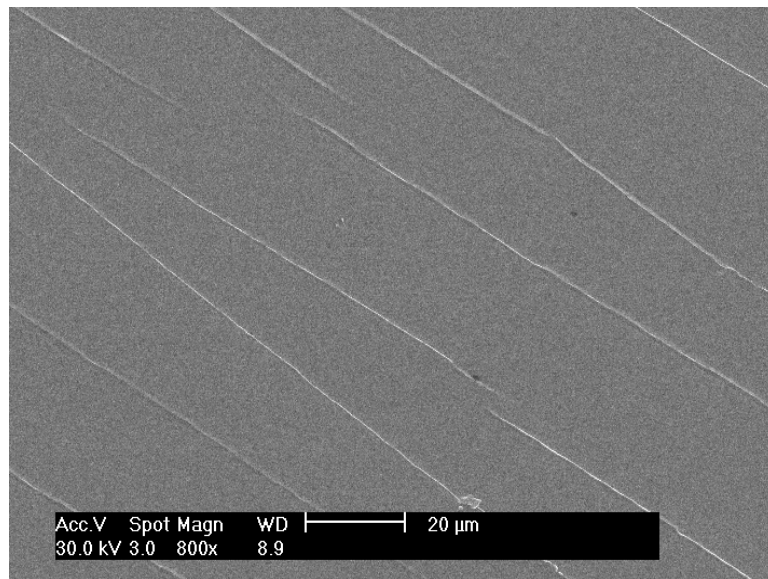
Figure 1-2 SEM image of the commercial ITO electrode on PET substrate after bending test (radius ~15 mm).

The most significant is its cost which is increasing drastically because of the limited supply of indium and the increasing demand from the rapidly expanding display market, which potentially prevents the realization of low cost and large scale organic optoelectronic device fabrication. Therefore, there is a strong need to find alternative materials to replace ITO as a high transparency electrode.

Fluorine doped tin oxide (FTO), another commercially available TCO, is also used for transparent electrode for OLEDs and OSCs[18-20] instead of ITO, mainly because of its lower cost. Even though it shows relatively good results for device applications, several problems prevent its use for high performance device applications. First, its low work function limits efficient hole injection, especially in the OLEDs. Second, its rough surface causes high leakage current in organic devices, leading to low efficiencies. Third, the properties of FTO films are strongly dependent on the fabrication method.

Al doped ZnO (AZO), another promising alternative to ITO, is showing promise for transparent electrode applications because it uses Zn and O, which are inexpensive, and because it can achieve resistivity comparable to that of ITO. It has been investigated as a transparent anode in OLEDs instead of ITO. However, optimum performance has yet to be achieved because its work function and conductivity are lower than those of ITO[21, 22]. Further development of the deposition technique is also required before practical use because the electrical properties of AZO films are strongly dependent on the deposition methods and conditions[23].

Besides the above mentioned TCOs, other ternary or quaternary transparent conducting oxides such as Ga-In-Sn-O ((GITO), Zn-In-Sn-O (ZITO), Ga-In-O (GIO), and Zn-In-O (ZIO) have been studied, all of these have higher work function than ITO

and electrical conductivity similar to that of ITO and have shown promising results as anodes for OLEDs. However, they are potentially problematic because of the indium element, which may diffuse into the organic layer in OLEDs and also makes those electrodes expensive.

Even though TCOs show promising characteristics such as high optical transmittance and electrical conductivity, none of them is the best choice as a TCE for future flexible applications because of the limitations in high temperature processing and the poor mechanical properties that these materials exhibit. They, especially ITO, need high temperature annealing of around 600°C to achieve high transmittance and conductivity, which is not compatible with a flexible plastic substrate. Also, they are easily cracked under bending stress, resulting in device failure. Thus, a new TCE other than TCOs must be developed.

1.2.2 Carbon nanotube networks

Carbon nanotube networks (CNTs) are another newly-emerging class of transparent, conductive electrode that can potentially replace ITO. CNTs are molecular-scale tubes of carbon molecules with outstanding properties. They are one of the stiffest and strongest materials known; also they have excellent electronic properties and many other unique characteristics. General information on CNTs can be found in elsewhere[24-28]. Besides the unique mechanical and electronic features of CNTs, recent research has demonstrated that they can be applied to optoelectronic devices as transparent, conductive electrodes[27, 29, 30]. Various methods such as spin coating, transfer printing, and vacuum filtration have been developed to control thickness, and optical and electrical characteristics.

Organic solar cells and light emitting diodes were recently demonstrated with transparent CNTs instead of ITO and showed performance (e.g. power conversion efficiency of OSCs) similar to that of ITO devices. Furthermore, CNTs are very promising for high reliability touch screens and flexible displays because they are substantially more mechanically robust than ITO films. Even though they have promising characteristics such as high transmittance and excellent mechanical strength, high performance large area organic devices are hard to achieve because of their high sheet resistance, resulting from the contact resistance of each carbon nanotube. The sheet resistance of carbon nanotube films is several times higher than that of conventional ITO films. Therefore, a new fabrication method that can reduce the sheet resistance of carbon nanotube films has to be developed.

1.2.3 Thin metal film

In most cases, highly conducting metal films are used as the rear electrode in organic devices. When transparent frontal electrodes using metal films are required, the metal film thickness must be reduced. Metallic films that are sufficiently thin (i.e. a few nm) compared to the wavelength of light can be optically transparent; if the film is continuous over a macroscopic distance, then the electrical resistivity of the film can remain usefully low. However, the fabrication of ultra thin and continuous metal films over large areas is difficult so the use of a thin metal film itself is limited in organic device applications.

Several metals with high work functions such as Au[14], Ni[31], and Pt[32] have been investigated as anodes for OLEDs. In these cases, metal was used to modify the surface of the ITO electrode or as the anode for top emitting devices. Surface modified

thin Ag films[33, 34] were used as semi-transparent electrodes instead of ITO but their degree of transmission was shown to be low.

1.3 Goal of research

To overcome the above mentioned problems, my research focuses on the development of a new type of transparent and conductive electrode based on metallic nanostructures; Such an electrode will make possible the production of truly low cost and high performance optoelectronic devices like OLEDs and OSCs. The proposed transparent metal electrode (TME)[35] is in the form of a periodic nanoscale metal wire grid fabricated by nanoimprint lithography (NIL)[36], which is an emerging lithographic technique and well-suited to the area of organic electronics that requires low-cost and high-throughput.

The fabricated transparent metal electrodes have high optical transparency and good electrical conductivity, and those properties are adjusted independently by changing the metal line width and thickness in the metal grid structure. It is shown that the proposed transparent metal electrode can serve as an alternative to conventional ITO electrodes for OLEDs and OSCs with the equally high performance[37]. To increase the efficiency, an organic solar cell device structures utilizing surface plasmon phenomenon has been investigated.

1.4 Organization of thesis

The organization of the thesis is as follows:

Chapter 2 presents the transparent metal electrode using Au, Al, Ag, and Cu on a rigid

substrate, such as glass, fabricated by conventional NIL (hot pressing). These electrodes display both high optical transparency and good electrical conductivity.

Chapter 3 describes the metal transfer printing process to realize TMEs on a flexible plastic substrates such as PET.

Chapter 4 describes metal transfer assisted nanolithography. This lithography technique can be used for not only the fabrication of TMEs on any substrate (rigid or flexible), but also for the fabrication of various shapes of nanoscale metal particle arrays, such as squares, diamonds, and nanobars.

Chapter 5 presents OLEDs device with transparent metal electrodes as an anode and shows the first working device using this electrode.

Chapter 6 presents OSCs with transparent metal electrodes as a frontal TCE and shows the performance of OSCs made with the TME is comparable to that of the device with a conventional high performance ITO electrode. Also, an OSC on a flexible substrate is demonstrated.

Chapter 7 proposes and investigates a scheme by which the power conversion efficiency of OSCs can be enhanced using TMEs. Surface plasmon resonance (SPR) is utilized to increase light absorption in organic layer by concentrating the light in the OSC structure.

Chapter 8 summarizes all the work done so far and discusses the future experiments to be done.

Chapter 2

Transparent Metal Electrodes on Glass substrates by Conventional Nanoimprint Lithography

2.1 Introduction

2.1.1 Nanostructured transparent metal electrode (TME)

Transparent metal electrode[35] is in the form of nanoscale periodically perforated dense metal mesh films on glass substrate. Such structures are fabricated based on two design considerations: 1) the line-width of the metal mesh is designed to be sub-wavelength to provide sufficient transparency and to minimize light scattering; 2) the period of the mesh is chosen to be submicron to ensure the uniformity of the current injection (collection) into (from) the organic semiconductors. Such large area dense nanostructures are fabricated by nanoimprint lithography (NIL)[36, 38], which is ideal for this application due to its inherent high resolution and high throughput features. A unique property of such electrodes in that their optical transparency and the electrical conductivity can be tuned separately by changing the aperture ratio and the metal thickness, thereby making it possible to tailor the structures for different applications is shown.

2.1.2 Nanoimprint lithography (NIL)

NIL is a thermal molding process where the pattern on the mold is physically imprinted into the resist layer at elevated temperature and under high pressure. The schematic of NIL process is shown in Fig. 2-1.

1. Imprint
Press Mold
+
Heat

Mold
Resist
Substrate

Remove Mold

2. Pattern Transfer
RIE
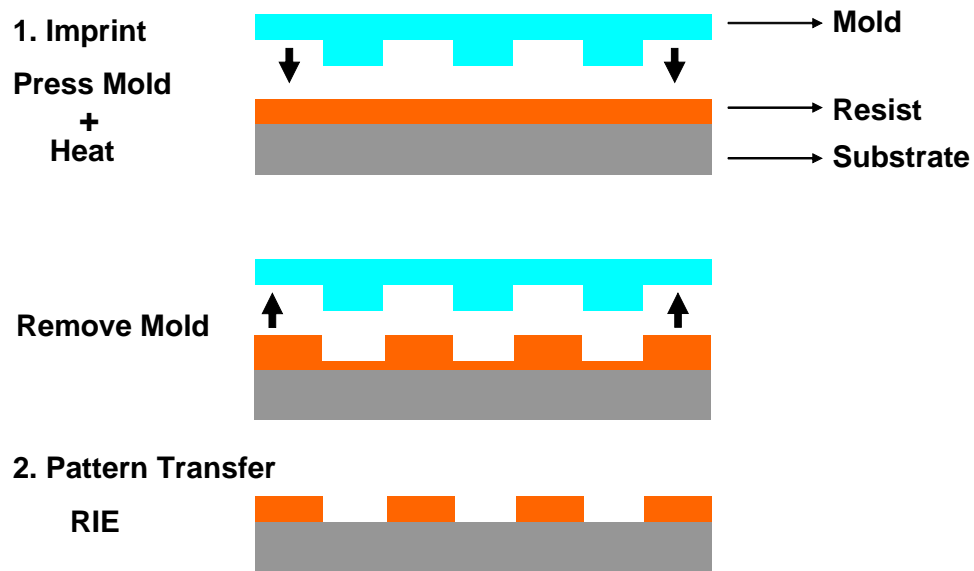
Figure 2-1 Schematic diagram of NIL process

A mold with relief patterns is first fabricated by conventional lithography techniques (photolithography, laser interference lithography or electron beam lithography) and reactive ion etching (RIE). The mold surface is then coated with surfactant to avoid polymer sticking during nanoimprint. On the substrate, a thin layer of thermal plastic polymer is spun to serve as the resist layer. The mold and the polymer-coated substrate are then brought into intimate contact. The whole assembly is then heated up to an elevated temperature at which the polymer melts. Then a high pressure is applied to the assembly, and the mold relief pattern is physically imprinted into the

polymer layer because polymer melts flows under the pressure. After a certain hold time to allow sufficient polymer flow to accurately replicate the pattern on the mold, the mold-substrate assembly is cooled to room temperature and the polymer solidifies. Due to the molding nature of the NIL process, there is always a thin layer of polymer left underneath the mold protrusions during nanoimprint. This thin layer, commonly referred as residual layer, need to be removed prior to further pattern transfer. This residual layer removal process is usually done by short time oxygen RIE. Once the residual layer is removed, the polymer layer can serve as the resist to transfer the pattern to the substrate. Depends on the methods of the pattern transfer used, both positive and negative mold pattern can be achieved on the substrate. If the polymer layer is used as etching mask in substrate etching, a reverse mold pattern is achieved on the substrate. If the polymer layer is used for metal lift-off, and then used the metal layer as the etching mask, the same mold pattern can be replicated exactly on the substrate. This NIL is promising as the solution for future lithography because it integrates high-resolution, low-cost, high-throughput and easy-to-operate all together. Therefore, NIL is well suited for the area of organic electronics that requires low cost and high throughput fabrication with high resolution.

2.2 Transmission simulation using G-solver

To show that nanopatterned metal grating can be used as highly transparent electrode, optical transmittance was calculated using Grating solver[39], commercial software based on rigorous coupled wave analysis (RCWA). 700 nm period Cu grating with a line-width of 70 nm (geometric aperture of 90 %) and a height of 40 nm was considered. Transparent Cu electrode is well suited for practical organic electronic

applications as a replacement for ITO as it has a similar work function to ITO (ca. 4.7eV) and is one of the cheapest metals. Simulation (Fig. 2-2) predicts Cu grating is highly transparent and it can be readily used as a transparent electrode. The optical transmittance spectra of the Cu grating with a line-width of 70 nm for the period of 700 nm are quite flat and the average transmittance in visible range is about 91 %.
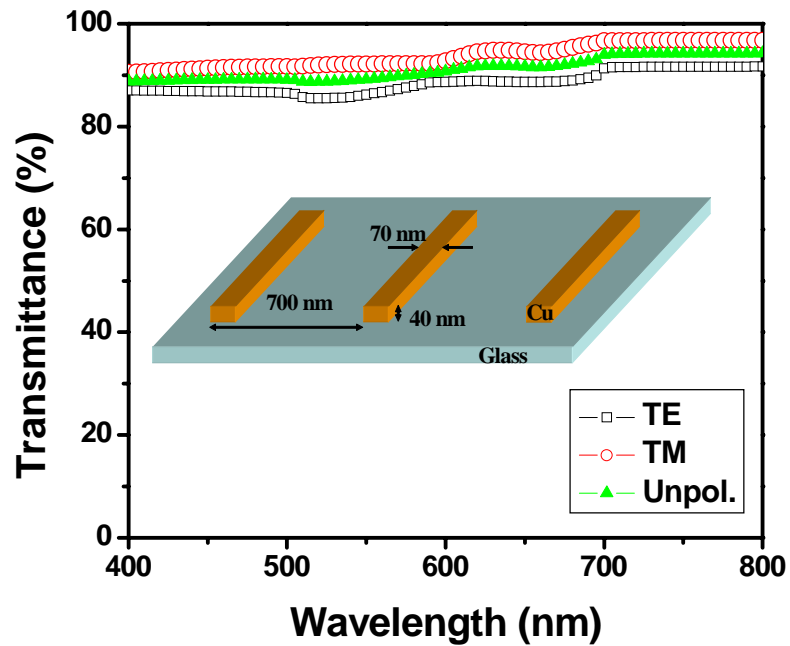
Figure 2-2 Transmittance simulation of the Cu grating on glass substrate. Cu grating has a period of 700 nm, line-width of 70 nm, and thickness of 40 nm.

Other metals such as Au, Ag, and Al were also considered and exhibit similar properties in terms of flatness of transmittance spectra and average transmittance. Therefore, we can expect metal grating electrode is promising not only because it is highly transparent, but also because the work function of transparent electrode side can be easily changed by choosing different metals.

2.3 Experimental details

2.3.1 Fabrication of the mold for transparent metal electrode (TME)

Fabricated nanopatterned TME consists of two grating structures orthogonally positioned to each other. One is 700 nm period grating that defines the main part of the transparent metal electrode because it determines the overall optical transparency. The other is the 10 μm period grating and is used to ensure the electrical connectivity of the 700 nm period grating lines in case some of lines may be disconnected due to defects in the mold and the fabrication processes while minimizing the transmittance loss. The 10 μm period grating also helps to distribute the current flow in the transparent electrode in a quasi-2D fashion, which is important for addressing the organic devices in certain applications. The optical transmittance of the metal electrode is dominantly determined by the line-width of the grating lines, or equivalently, the opening ratio of the grating. Therefore, it is important to fabricate each mold with narrow line-width.

2.3.1.1 Line-width reduction by shadow evaporation

A simple technique based on imprinting and shadow evaporation was developed to allow grating structures with varied line-width to be fabricated while keeping the same period. Figure 2-3 shows the schematic diagram of the shadow evaporation technique.
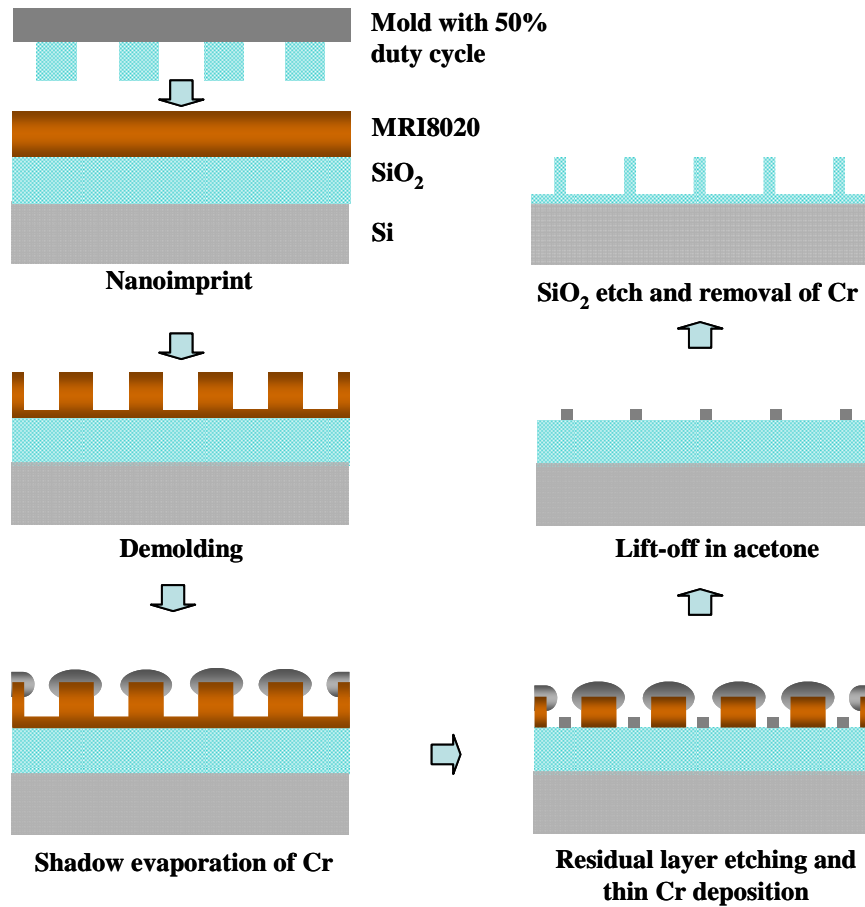
Figure 2-3 Schematic diagram of the shadow evaporation technique.

This is critical step because the degree of the transmittance mainly depends on the opening ratio of the fabricated electrode. Nanonex NX2000 naonoimprinter (Princeton, NJ) is used for NIL process. For the fabrication of the 700 nm period mold with narrow line-width, an original 700nm period SiO_2 grating mold with 50 % duty cycle fabricated by the conventional photolithography (stepper) is used to imprint a MRI-8020 resist (Microresist Technology GmbH) spin-coated on a SiO_2 substrate, at a pressure of 600 psi and a temperature of 180 °C for 5 min. After cooling and demolding, Cr is deposited using e-beam evaporation on each side of the imprinted resist by shadow

evaporation technique as shown in Figure 2-3. Metal line-width can be easily varied at this step by changing the thickness of the evaporated Cr. An anisotropic oxygen plasma etching is used next to remove the residual resist in the imprinted areas. After this, an additional thin Cr layer is deposited and used as SiO_2 etching mask after a lift-off in acetone. SiO_2 is then etched using CHF_3 of 20 sccm for 10 min with power of 150 W and a pressure of 20 mT resulting in 200 nm depth of grating. Treatment of anti-sticking layer (1H, 1H, 2H, 2H-perfluorodecyl trichlorosilane) of the mold after Cr removal completes fabrication of mold with increased trench width. Figure 2-4(a) shows the SEM image of original 700nm period mold with 50 % duty cycle. After imprinting using this mold thin Cr layer is deposited on each side wall of the imprinted resist pattern by shadow evaporation as shown in Figure 2-4(b). To fabricate the mold with line width of 200 nm (Fig. 2-4(c)) and 120 nm (Fig. 2-4(d)), Cr of 65 nm and 100 nm were deposited on each sidewall.
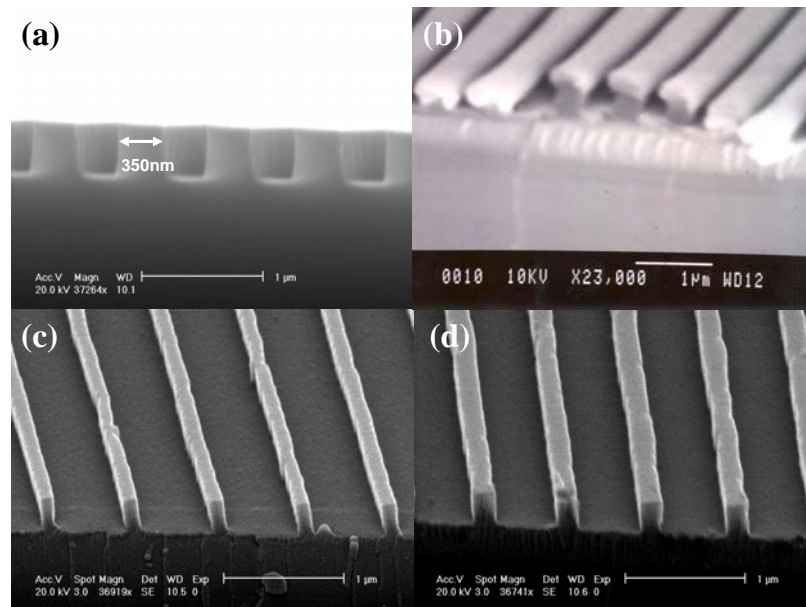
Figure 2-4 SEM images of (a) original 700 nm period mold, (b) after shadow evaporation, and fabricated mold with a line-width of (c)120 nm and (d) 200 nm.

2.3.1.2 Line width reduction by wet etching and shadow evaporation

To obtain higher optical transparency, the line-width of the original 700 nm period grating with a 50 % duty cycle was alternatively reduced by a simple wet chemical etching process rather than the shadow evaporation method used in the previous work. In case of shadow evaporation, fabricated line of the mold is too rough to be used for transparent metal electrode when thick metal (>100 nm) has to be deposited for higher transmittance. Rough line would also increase the resistance of each line by surface scattering. On the other hand, the wet etching approach produced gratings with smoother sidewalls, which could help to reduce the surface scattering of electrons and therefore increase the conductivity of the wire electrode. For this, an original 700 nm period SiO_2 grating mold with a depth of 500 nm and a duty cycle of 50 % was etched by Buffered HF improved purchased from Transene company for 80 s resulting in line-width of ~ 70 nm as shown in Figure 2-5(a). The SiO_2 etch rate was about 100 nm / min in BHF. The second grating mold with a period of 10 μm and a line-width of 850 nm first created by conventional photolithography as shown in Fig. 2-5(b) was also etched by Buffered HF improved to reduce line-width to 400 nm.
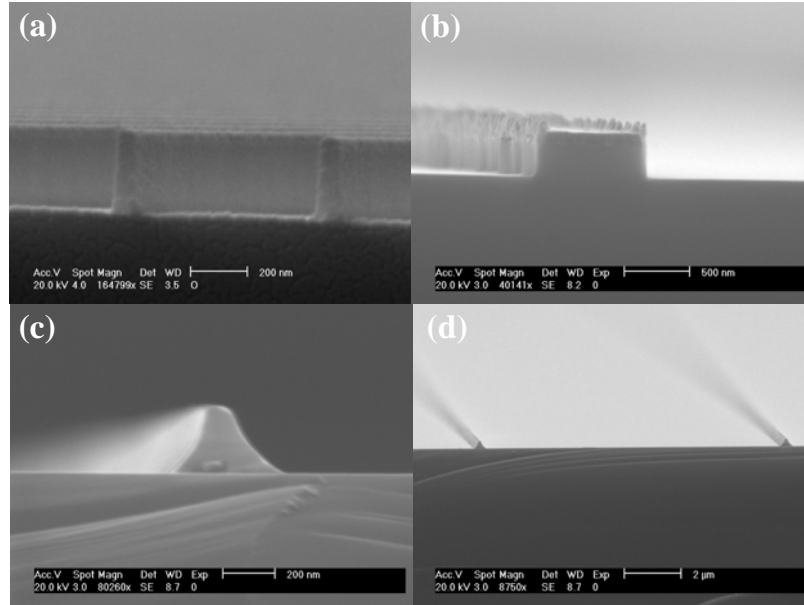
Figure 2-5 (a) SEM image of the 700 nm mold with line-width of 70 nm fabricated by BHF etching, (b) 10 μm period mold with a line-width of about 800 nm fabricated by conventional photolithography, (c), and (d) 10 μm period mold with reduced line width by BHF etching for 2 min.

In wet etching approach, one important thing is the thickness of the SiO_2 layer on Si substrate. To fabricate the mold shown in Fig. 2-5(a), a starting 700 nm period oxide grating was etched down to Si substrate before wet etching resulting in little variation of the grating line between top and bottom of the structure. In case of 10 μm period grating, however, very thick (2μm) oxide was used as a substrate and only 500 nm of oxide was etched using dry etching to fabricate the starting mold. Therefore, the shape of the resulting grating line has a triangular shape (Fig. 2-5(c-d)) because of the nature of the wet chemical etching. However, this tapered shape was easily turned to vertical shape through additional imprinting using this mold and shadow evaporation technique discussed in previous section.

2.3.2 Fabrication of rectangular grid mold

After the fabrication of two grating molds with narrow line-width, a new mold with rectangular mesh grid was fabricated by applying NIL twice. Nanonex NX2000 naonoimprinter (Princeton, NJ) was used for the NIL process. Figure 2-6 shows the schematic process diagram of the fabrication of the rectangular shape grid mold.

1st NIL

Residual Layer etching and Cr deposition

Lift-off

Resist coating

2nd NIL

Residual layer etching, Cr deposition, and lift-off

SiO$_2$ etching and Cr removal
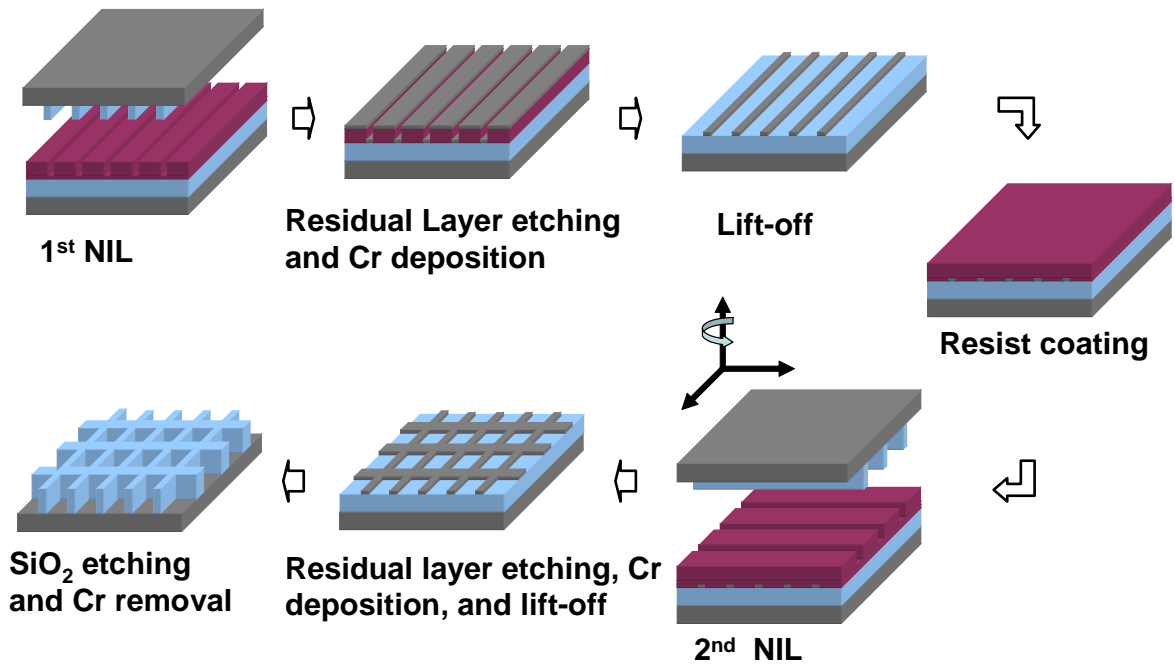
Figure 2-6 Schematic diagram of the fabrication of the mesh type mold.

10μm period mold was first used to imprint a 300 nm thick MRI-8030 resist (Microresist Technology GmbH) spin-coated on a SiO$_2$ substrate, at a pressure of 600 psi and a temperature of 180 °C for 5 min. After cooling and demolding, an anisotropic oxygen plasma etching was used to remove the residual resist in the imprinted areas. After this an additional 20 nm thick Cr layer is deposited and used as SiO$_2$ etching mask after a lift-off in acetone. The 700 nm period grating molds with a different line-width

(e.g. 200 nm, 120 nm, and 70 nm) were used for the second NIL and followed the same procedure as above except that the substrate was turned to 90 ° in NIL. SiO_2 was then plasma-etched using CHF_3 and CF_4 of 15 sccm for 8 min with power of 100 W and a pressure of 15 mT, which resulted in a 140 nm deep rectangular grid pattern. Treatment of anti-sticking layer (1H, 1H, 2H, 2H-perfluorodecyl trichlorosilane) of the mold after Cr removal completed fabrication of the mold with rectangular shaped grid patterns. Figure 2-7 shows the schematic of fabricated mold and SEM images of rectangular mesh grid mold with different line-width in grating a.
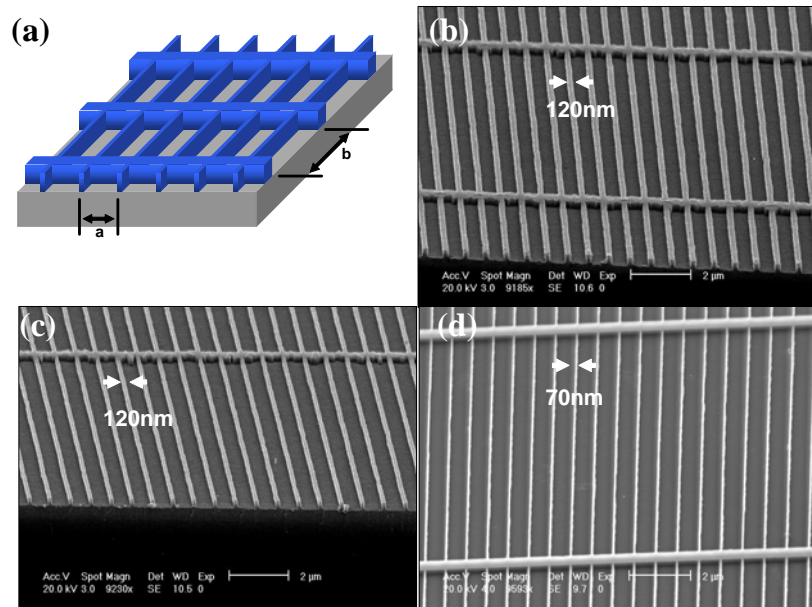
Figure 2-7 (a) Schematic of the fabricated mold. a: 700 nm, b: 10μm. SEM images of the fabricated mold with line width of (b)200 nm, (c)120 nm, and (d)70 nm.

Three molds with different line width of 200 nm, 120 nm, and 70 nm were fabricated. All molds have a common 10 μm period grating to ensure the electrical connectivity of the metal grid on glass. As shown in this work, NIL offers a variety of opportunity for the fabrication of the various shape nanostructure. Apart from mesh structure, various shapes

of nanometer scale particle structures such as square, diamond, and bar shape can also be fabricated using NIL.

2.3.2 Fabrication of TME on glass substrate

To transfer the rectangular mesh grid patterns of the mold into a resist layer on a glass substrate NIL was used again with same condition as above. Standard oxygen residual etching, metallization, and lift-off completed the fabrication of the transparent metal electrode on glass. Different metals of Au, Cu, Al, and (or) Ag electrodes with a thickness of 40 nm were prepared using the method described above to show that the fabrication process can be readily applied to various metals. Figrue 2-8 shows one of the transparent metal electrodes with line width of 70 nm on glass substrate. As shown, a uniform dense metal mesh structure was successfully created.
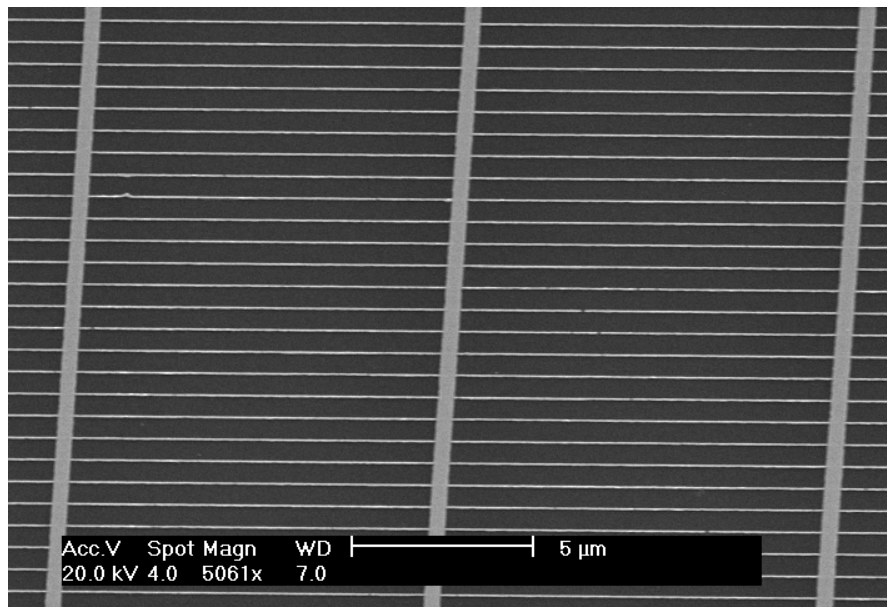
Figure 2-8 SEM image of the transparent metal electrode on glass substrate with a line width of 70 nm.

2.4 Experimental results and discussion

Optical transparency and electrical conductivity are the two most important factors for transparent electrodes. They can be quantified experimentally by measuring the transmittance and the sheet resistance respectively. The parameters for tuning the transmittance and the sheet resistance in our structure are mesh line-width, metal thickness, and periodicity of both grating lines. On the other hand, the metal thickness and the overall mesh fill factor determine the sheet resistance of the structure. It is shown that the two parameters can be controlled separately, providing sufficient design latitude for optimal performance. To characterize the optical transmittance and the sheet resistance ($R_\square$) of the semi-transparent electrodes, three sets of the samples (line-width: 200, 120, 70nm) having large area rectangular grids are prepared. All samples use 40 nm thick metals with 2nm Ti adhesion layer. Several metals such as Au, Cu, Al, and (or) Ag are tested in the experiment. Figure 2-9 shows the transmission spectra for each electrode structure. The transmittance of the unpatterned metals (e.g. Au, Cu) was also shown as a comparison. All the transmittance measurement was referenced to air.
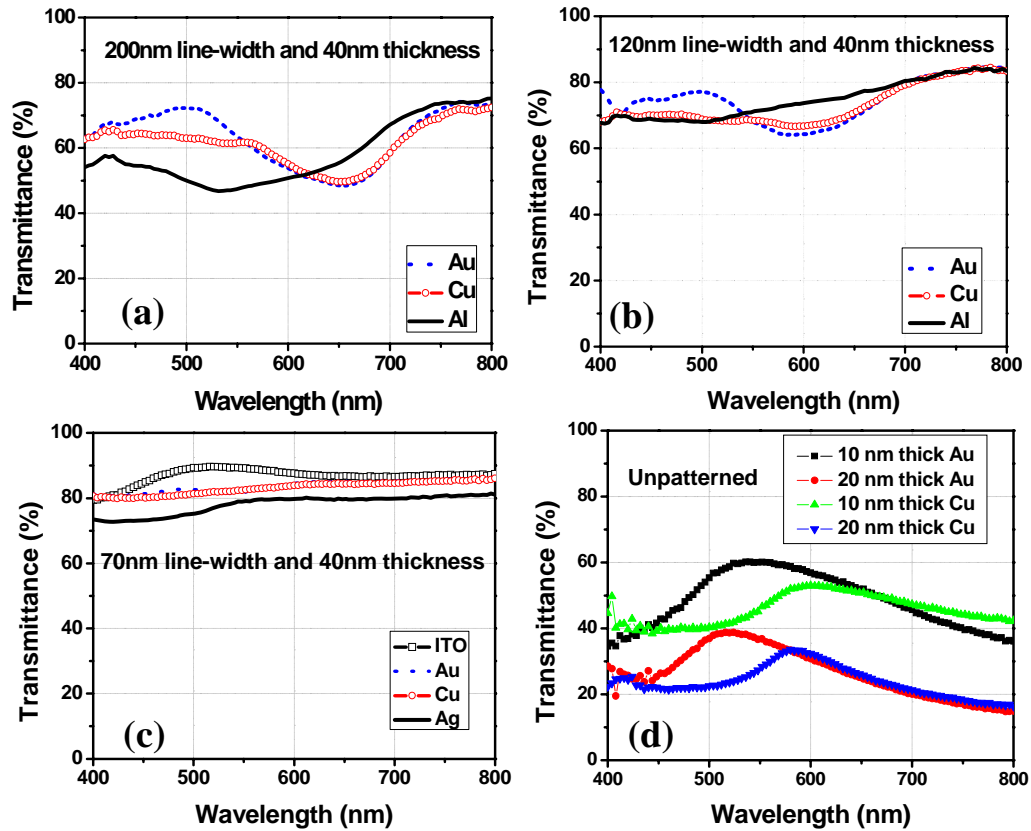
Figure 2-9 The optical transmittance of 40 nm thick transparent metal electrode with line-widths of 200 nm (a), 120 nm (b), 70 nm (c), and unpatterned (d) on glass substrate.

For metal electrodes with 200 nm line-width, average transmittance in the visible range is 63 %, 58 %, and 61 % for Au, Al, and Cu electrode, respectively. As shown in Figure 2-9(a), the transmittance is much dependent on wavelength in these cases and the trend of wavelength dependency is different for different metals. We can increase the transmittance by reducing metal line-width from 200 nm to 120 nm as shown in Figure 2-9(b). The average transmittance is increased by more than 10 % as compared with the one with 200 nm line-width but the same thickness. Moreover, the wavelength dependency is much mitigated by using reduced line-width. The average transmittance for the metal

electrode with 120 nm line-width and same thickness (40 nm) is 74 %, 75 %, 73 % for Au, Al, and Cu electrode, respectively. The transmittance in longer wavelength region (above 700 nm) is over 80 % for all three metals. On the other hand, Au electrode shows high transmittance in short wavelength region (below 500 nm) and low transmittance in mid wavelength region (between 500 nm and 700 nm). Al electrode shows flatter transmittance than Au electrode and transmittance is increased gradually as wavelength is increased. Cu electrode shows intermediate behavior between Au and Al electrode. The wavelength dependence of transmittance is correlated to the plasmon absorption band in different metals. Much higher transmittance was achieved by reducing the line with further (e.g. 70 nm) as shown in Fig. 2-9(c). The average transmittance in the visible range is 84 %, 83 %, and 78 % for Au, Cu, and Ag electrode, respectively. Interestingly, Ag electrode has lower transmittance than Au and Cu electrode even though it has same line-width and thickness, which is believed to be related with dispersion property of the Ag material. The transmittance of these metal electrodes is relatively flat over the visible region. The wavelength dependency observed previously in the nanoimprinted metal electrode having a wider line-width (e.g. 200 nm and 120 nm) was significantly reduced by using narrower metal line-width, 70 nm. As a comparison, the optical transmittance of the conventional high performance ITO electrode was also measured and shown in Fig. 2-9(d). ITO has a peak transmittance of 90% at 500 nm and an average transmittance of 87 % in the whole visible range. Figure 2-9(d) shows the transmittance spectra of unpatterned metal film (e.g. Au, Cu). As shown, the transmittance of unpatterned metal film is quite low (maximum transmittance at a specific wavelength is less than 60 % for 10 nm thick film) and not adequate as a general transparent and conductive electrode even though their superior sheet resistance (a few ohm/square for 20 nm thick film).

24

The increase in the transmittance by reducing the metal line-width is also accompanied by the increase in sheet resistance. But such increase of the sheet resistance can be compensated by using thicker metals. For instance, the average transmittance and sheet resistance for metal electrode with 120 nm line-width and several thicknesses are summarized in Figure 2-10.
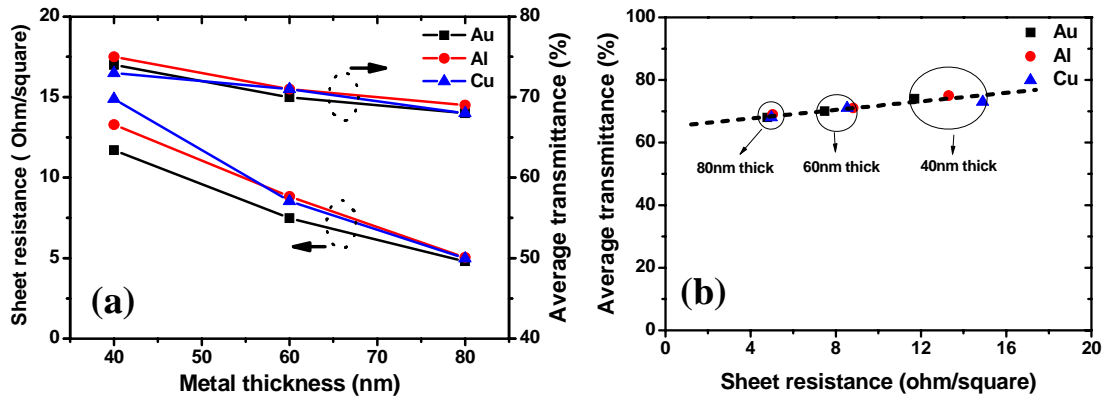
Figure 2-10 (a) Sheet resistance and average transmittance as a function of metal thickness and (b) average transmittance vs. sheet resistance of transparent metal electrodes with a line width of 120 nm.

The sheet resistance for the metal electrode with a line-width of 200 nm and thickness of 40 nm is 7.68 $\Omega/\square$, 8.45 $\Omega/\square$, 10.8 $\Omega/\square$ for Au, Al, and Cu electrode, respectively. Sheet resistance is increased from 7.68 $\Omega/\square$ to 11.7 $\Omega/\square$ for Au electrode by reducing line-width from 200 nm to 120 nm for higher transmittance. The amount of increase of the sheet resistance for Al and Cu electrode is similar to that of Au electrode. As shown in Figure 2-10(a), the sheet resistance can be significantly reduced by making metal electrode thicker. For example, sheet resistance of 11.7 $\Omega/\square$ for 40 nm thick Au electrode is decreased to 4.79 $\Omega/\square$ for 80 nm thick Au electrode with only small reduction in transmittance. For all considered case, the sheet resistance is decreased by more than

59 % but the transmittance is decreased only by less than 8 % by using thicker metal from 40 nm to 80 nm. These results are plotted in Figure 2-10(b). It can be seen from the fitted line that the sheet resistance could be further decreased to less than a few Ω/□ with only small decrease of average transmittance if metals thicker than 80 nm are used. These results confirm that transmittance and sheet resistance of the semi-transparent metal electrode can be easily tuned by varying metal line-width and thickness. All the measurement results such as average transmittance and sheet resistance is summarized in Table 2- 1.

Table 2-1 Average transmittance and sheet resistance of various transparent metal electrode.

Metal	Line width (nm)	$R_{\square}$ (Ω/□)	T_{avg} (%)
Au	200	7.68	63
	120	11.7	74
	70	24	84
Cu	200	10.8	61
	120	14.89	73
	70	28	83
Al	200	8.45	58
	120	13.3	75
Ag	70	23	78
ITO		12	87

An important observation can be made from these results that the transparency of such electrode structure can be increased without sacrificing the overall conductivity by using narrower and thicker metal lines. This characteristic is another advantage over ITO electrode in which the sheet resistance has to be compromised in order to achieve high

transmittance. Therefore, nanoimprinted transparent metal electrode is very promising not only because it can prevent the disadvantage of ITO electrode but also because it can meet the requirement of both sheet resistance and optical transmittance by optimizing the duty cycle of the periodic patterns on the mold and the metal thickness.

2.5 Summary

In summary, a new type of transparent and conductive electrode based on metallic structures was proposed as an attempt to replace the conventional transparent and conductive electrode, ITO. A scheme was developed to fabricate transparent metal electrode in the form of nanoscale periodically perforated metal mesh film which shows high optical transmittance in the visible range as well as excellent electrical conductivity. Transparent metal electrode can be used in many other applications instead of ITO for which specific transmittance and conductivity are required because they are easily tuned by varying the line-width and the thickness of the metals. Moreover, the work function of an anode can be easily changed by choosing different metal materials which provide more flexibility in studying the effect of anode work function on device behaviors. Furthermore, similar structure can be made on flexible plastic substrate. Obtained results indicate that transparent metal electrode is an attractive and potentially practical solution as a transparent, conductive electrode.

Chapter 3

Transparent Metal Electrodes on Flexible Plastic Substrates by Metal Transfer Printing

3.1 Introduction

Organic optoelectronic devices such as organic solar cells (OSCs)[4, 40-43] and organic light emitting diodes (OLEDs)[1, 2] offer promising alternatives to inorganic counterparts particularly for specific applications such as packaging, clothing, flexible screen that inorganic devices can not reach. These potentials are due to their low cost, easy fabrication and compatibility with flexible substrate over large areas. So far, most of those devices have been built on conventional transparent electrode, indium tin oxide (ITO). However, it is not the best choice for low-cost and high-performance flexible applications. The high quality ITO, especially high conductivity, is hard to be achieved because of the limitation in high temperature processing of flexible substrates. Thus, the poor conductivity of the ITO film on flexible substrates[5, 44, 45] can cause a voltage drop along the addressing line, thus limiting the operation of a large area passive matrix OLED array[15] and reduce the fill-factor (FF) of the solar cell device resulting in low power conversion efficiency (PCE) of large area OSCs[46]. The mechanical strength is also not enough for flexible applications. The poor mechanical stability of the ITO can cause device failure when the ITO-coated flexible substrate is bent[17, 30, 46]. Moreover,

the price of ITO drastically increases due to the limited supply of the indium and the increasing demand from the rapidly expanding display market. These aspects of the ITO potentially prevent the realization of low cost and high performance large scale and flexible OLED and OSC fabrication.

As demonstrated in Chap. 2, proposed nanopatterned transparent metal electrodes[35] showed promising potential as replacement of the ITO electrode. However, the lithographic technique used, nanoimprint lithography (NIL), for the fabrication of transparent metal electrode is not compatible with the flexible substrate. The conventional NIL requires high pressure and high temperature when imprinting thermoplastic material, which can cause deformation of the flexible substrate. Therefore, another nanoscale patterning technique which can easily produce the nanostructure metal mesh pattern is needed. In this work, we demonstrate the nanoscale metal transfer printing and its application to fabrication of nanostructured transparent metal electrode on flexible substrate[47]. It is an additive technique that produce metal patterns directly on a plastic substrate, which eliminates the additional processes such as oxygen reactive ion etching (RIE) for residual layer etching and lift-off process used in conventional NIL process as described in Chap. 2. The transparent metal (Cu) electrode on polyethylene terephthalate (PET) substrate fabricated by transfer printing of nanoscale dense metal mesh shows high transparency in the visible range as well as good electrical conductivity. The mechanical strength of the Cu electrode on PET substrate under simple bending test is shown to be superior to that of the conventional ITO. Therefore, the fabricated transparent Cu electrode on flexible substrates is much more promising for organic optoelectronic device application than ITO.

3.2 Principle of metal transfer printing

The technique developed was inspired by the work on nanoscale patterning of metal films with a flexible stamp as an advanced technique for nanofabrication[48]. In this work, the transfer of metal films on the substrate relies on the chemical bonding between those two surfaces leading to successful transfer. Recently, it has been reported that the transfer of metal films on polymer substrates can be achieved by use of noncovalent surface forces[49]. The adhesion difference in each surface played a role of successful transfer.

Fig. 3-1 shows the schematic of the metal transfer printing onto a flexible substrate. Flexible polydimethylsiloxane (PDMS) structure is used as a stamp because it has very low surface energy[50]. Metals such as Au and Cu deposited on PDMS stamp are transferred onto a flexible substrate from PDMS stamp with slight pressure (e.g. 10 - 30 psi) and heat of about 10 °C greater than glass transition temperature (Tg) of the substrate. The temperature over the Tg of the plastic substrate will increase the adhesion ability of the plastic substrate by forming a sticky surface. Alternatively, an interfacial thin polymer layer can be used between metal and plastic substrate.
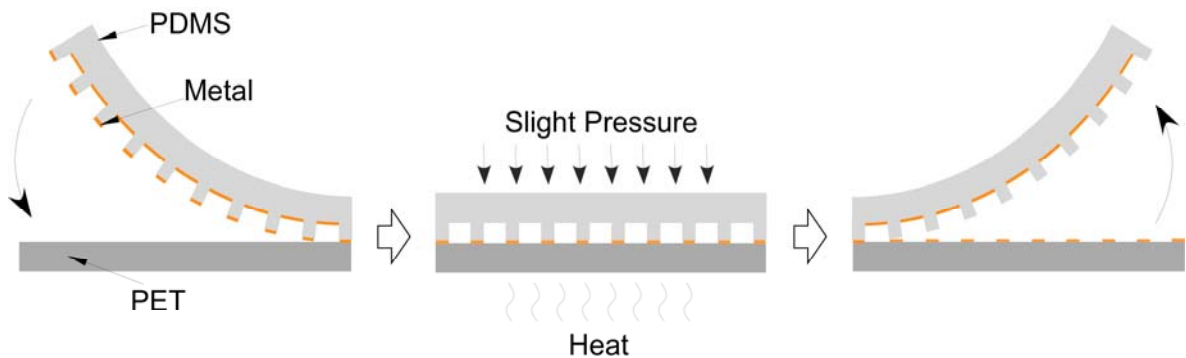
Figure 3-1 Schematic of metal transfer printing on a flexible substrate.

3.3 Experimental details

3.3.1 Fabrication of PDMS stamp

Flexible PDMS stamp is needed to transfer thin metal films from its protrusion region onto PET substrate. Fig. 3-2 shows the schematic diagram of the fabrication procedure of the PDMS stamp.

SiO$_2$ mold

Casting and curing

NIL resist

(a) NIL   **(b) PDMS fabrication**   **(c) PDMS demolding**
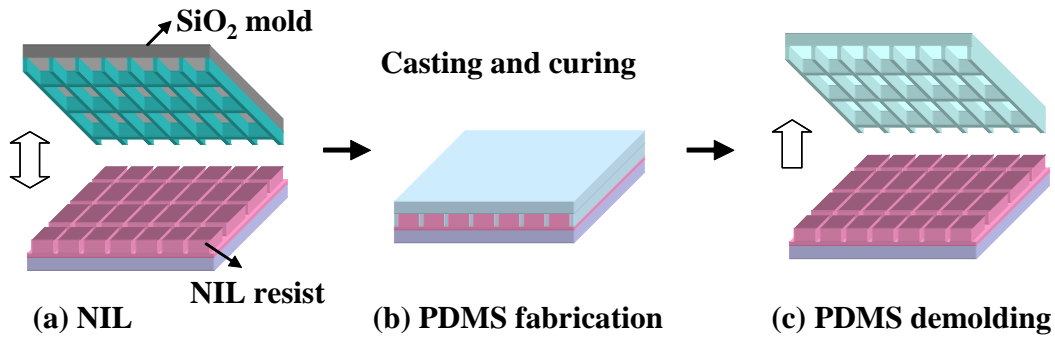
Figure 3-2 Schematic diagram of the fabrication procedure for the PDMS stamp.

Resist template with nanoscale mesh patterns is first fabricated by conventional NIL. The detailed fabrication procedure for the SiO$_2$ mold with mesh patterns for NIL can be found in Chap. 2. The molds used in this work consist of two sets of grating structure which are orthogonally positioned. One has a period of 700 nm, which defines the main part of the semitransparent Cu electrode. The other has a period of 10 μm, which is used to ensure the electrical connectivity of the 700 nm period grating lines. A Nanonex NX 2000 nanoimprinter (Princeton, NJ) was used for the NIL process. NIL is done on MRI-8020 resist (Microresist Technology GmbH) spin-coated onto a SiO$_2$ substrate at a pressure of 600 psi and a temperature of 180 °C for 5 min. After the

sample has been cooled and demolded, PDMS is drop-casted on nanoimprinted resist template. For easy generation of the nanoscale mesh patterns, recently developed high modulus PDMS[51] was first drop-casted and cured at 70 °C for 10 min which gives 100 μm thick PDMS on resist. The high modulus PDMS is a polymeric precursor formulated with short chain oligomeric polysiloxanes to increase its crosslinking density after cured by heat exposure. A high crosslinking density increases the stiffness of the cured PDMS allowing the replication of structures in the nanoscale regime. Commercially available PDMS, sylgard 184, is then drop-casted and cured at 70 °C for 2 hrs to support thin high modulus PDMS for better durability. Three types of PDMS stamp with different line-width were prepared.

3.3.2 Metal transfer printing on PET substrate

A 40 nm thick Cu and a 3 nm thick Ti are then deposited sequentially on the PDMS stamp by e-beam evaporation at a rate of 2 Å/sec. After brief O_2 plasma treatment on PDMS surface on which Cu and Ti were deposited, a Cu layer coated on PDMS stamp is transferred to PET substrate as shown in Figure 3-3.

:40 nm Cu / 3 nm Ti   PET
                       :30psi, 100°C, 3min

(d) Metal deposition   (e) Printing   (f) Removing PDMS
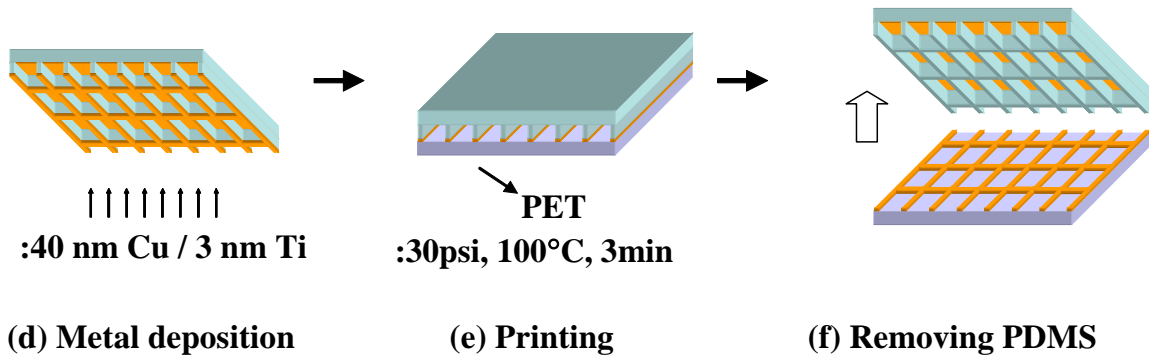
Figure 3-3 Schematic of the metal transfer printing onto PET substrate

O$_2$ plasma treatment oxidize whole Ti layer on Cu which make adhesion between the metal and the PET substrate stronger resulting in higher fabrication yield. To form intimate contact between the metal layer on protruded regions of the PDMS stamp and PET substrate, uniform pressure of 30 psi and temperature of 100 °C for 3 min were applied using nanoimprinter, NX 2000. It was found that 30 psi was the most effective pressure for metal transfer. Pressure lower than 30 psi generates mesh pattern with non-uniformity and pressure higher than 30 psi caused the metal layer in the recessed region of the PDMS stamp also transferred to PET because of the shallow depth of the PDMS stamp, 200 nm. The difference in adhesion strength between PDMS/Cu and Cu/PET interfaces determines the success of the metal transfer. Since the PDMS has low surface energy, the adhesion of Cu to it is poor. The elevated temperature (100 °C) will increase the adhesion ability of the PET substrate by forming a sticky surface. It is also known that the heating can reduce the surface energy of the PDMS stamp[49] which was possibly increased by the surface modification of the PDMS during the electron beam evaporation of the Cu film[52]. Fig. 3-4(a) and 3-4(b) show the perspective view of the fabricated PDMS stamp with a line-width of 200 nm and 120 nm, respectively. Figures 3-4(c) and 3-4(d) show the top view of corresponding transparent Cu electrode with a line-width of 200 nm and 120 nm on PET substrate. As shown, the dense metal mesh pattern was successfully fabricated.
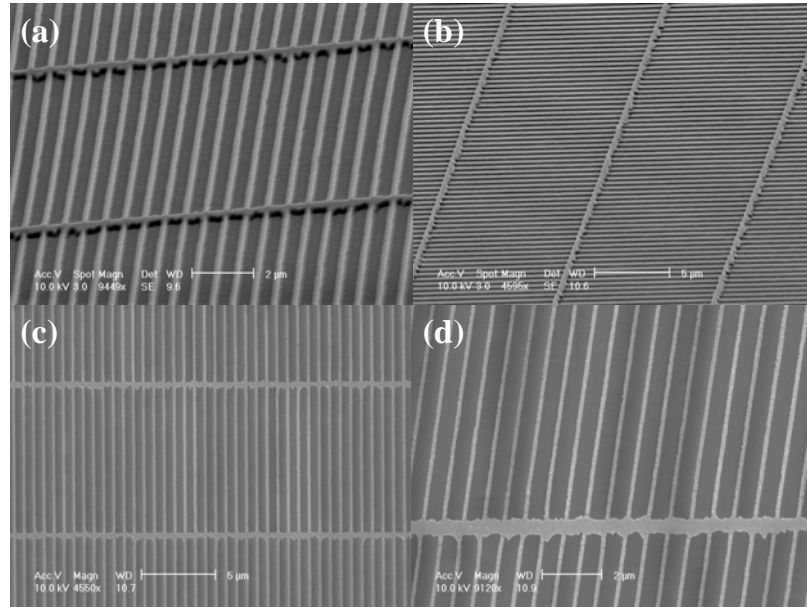
Figure 3-4 The perspective view of the fabricated PDMS stamp with line width of (a) 200 nm and (b) 120 nm, and the top view of corresponding semitransparent Cu electrode with line width of (c) 200 nm and (d)120 nm on PET substrate.

Since the metal transfer relies on the intimate contact between PDMS stamp and PET substrate, the surface roughness of the PET substrate is an important parameter. Initial PET substrate has RMS roughness of about 6 nm with peak to peak value of 20 nm. Rough surface creates several defects causing disconnection of the metal mesh pattern, which could limit the proper device operation. The surface roughness was significantly reduced by annealing at temperature lower than Tg of the PET as shown in Fig. 3-5. RMS roughness of 0.8 nm with peak to peak value of 2 nm was achieved by annealing PET at 70 °C for 30 min.
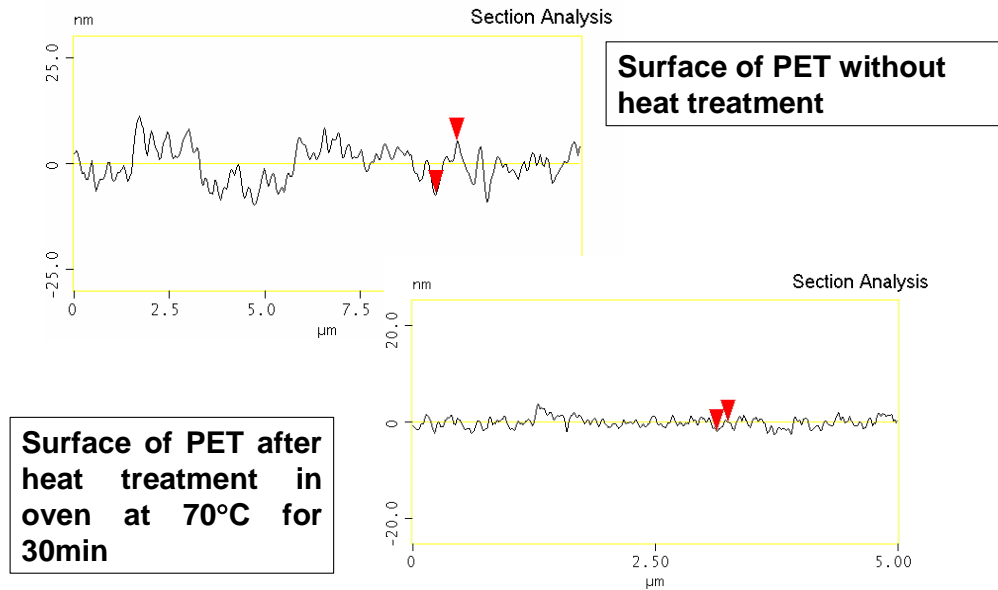
Figure 3-5 Surface roughness profile measured by Atomic Force Microscopy (AFM) before and after annealing of the PET substrate.

3.3.3 Metal transfer onto PEDOT layer on flexible substrate

The direct metal transfer printing discussed above has a limitation in choosing substrate material. Only the substrate with low Tg such as PET can be used for direct metal transfer printing because it relies on the physical bonding process between substrate and metals. As an expansion of the metal transfer printing, metal can be transferred onto a polymer layer coated on the substrate instead of directly transferring metal onto the plastic substrate. By using the interfacial polymer layer such as PEDOT:SS, metal grid on PDMS stamp can be efficiently transferred on the substrate. In this case, there is no limitation in choosing the substrate material and thus either soft or hard substrate can be readily used. Fig. 3-6 shows the schematic of the metal transfer printing onto PEDOT coated PET substrate.

(a) Metal deposition   **(b) Printing**   **(c) Removing PDMS**
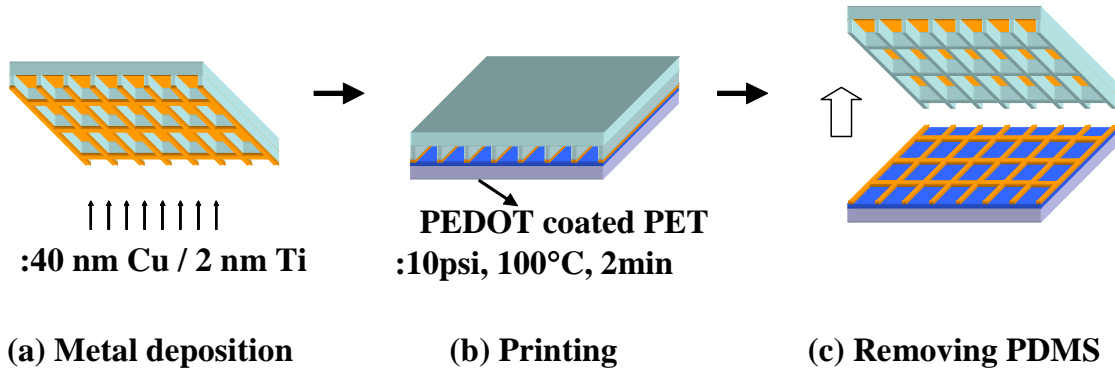
Figure 3-6 Schematic of the metal transfer printing onto PEDOT coated PET substrate.

To demonstrate this, a 40 nm thick Cu was then transferred onto 30 nm thick PEDOT:PSS layer spin coated on PET or SiO_2 substrate under a pressure of 10 psi and a temperature of 100 °C for 2 min. It was found that lower pressure than that needed for direct metal transfer printing on the PET substrate was needed. 0.1 wt. % glycerol was added to PEDOT:PSS to prevent the solvent from evaporating, which made the PEDOT:PSS layer sticky. The success of the metal transfer is determined by the difference in adhesion strength between PDMS/Cu and Ti/PEDOT:PSS interfaces. Since the PDMS has low surface energy, the adhesion of Cu to it is poor. Moreover, the sticky surface of the unbaked PEDOT:PSS makes the adhesion of metal to it stronger during printing process resulting in successful transfer of Cu mesh on to PEDOT:PSS layer. To increase the yield of the printing process, the surface of the PDMS stamp can be treated with anti-sticking layer (1H, 1H, 2H, 2H-perfluorodecyl trichlorosilane) before metal evaporation. Fig. 3-7 shows the SEM images of the SiO_2 mold, resist template, PDMS stamp, and transferred Cu mesh electrode on PEDOT:PSS coated PET substrate, respectively. The Cu mesh electrode has a line-width of about 70 nm in this experiment. As shown in Fig. 3-7(d), the large area Cu mesh pattern was uniformly transferred with

high yield.
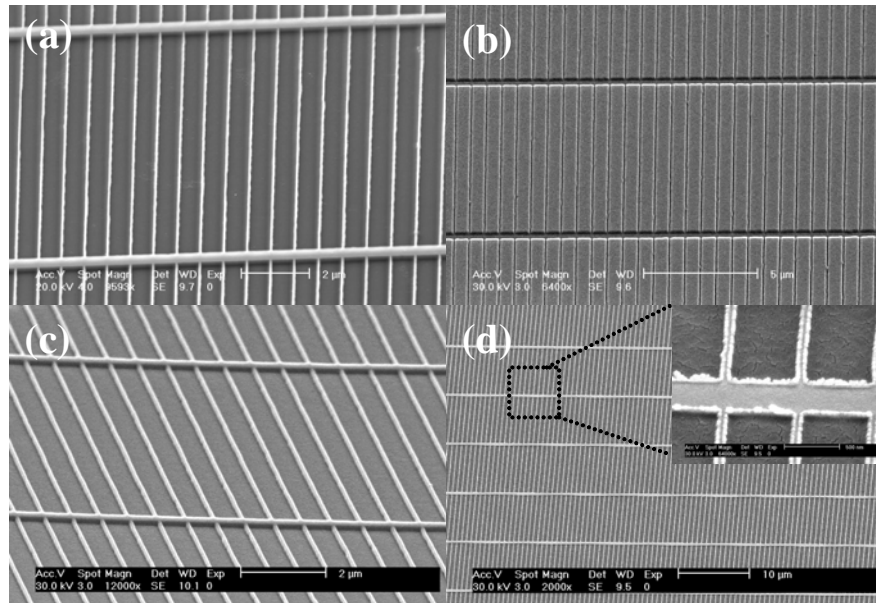
Figure 3-7 SEM images of (a) the SiO$_2$ mold for NIL, (b) the resist template, (c) the fabricated PDMS stamp, and (d) the transferred Cu mesh electrode onto PEDOT:PSS coated PET substrate.

3.3.4 Demonstration of nanopatterned metal electrode on flexible substrates using roll-to-roll nanoimprint process

The fabrication of the nanopatterned metal electrode using developed metal transfer printing can be easily extended to cost effective and large area fabrication such as roll-to-roll nanoimprint lithography (R2RNIL)[53, 54] due to the use of flexible molds. To demonstrate the possibility, an attempt was made to fabricate Au metal gratings on large area PET substrates using roll-to-roll process. Fig 3-8 shows schematics of a continuous R2RNIL process, which consists of two processing steps: (1) the coating process and (2) the imprinting-curing process.
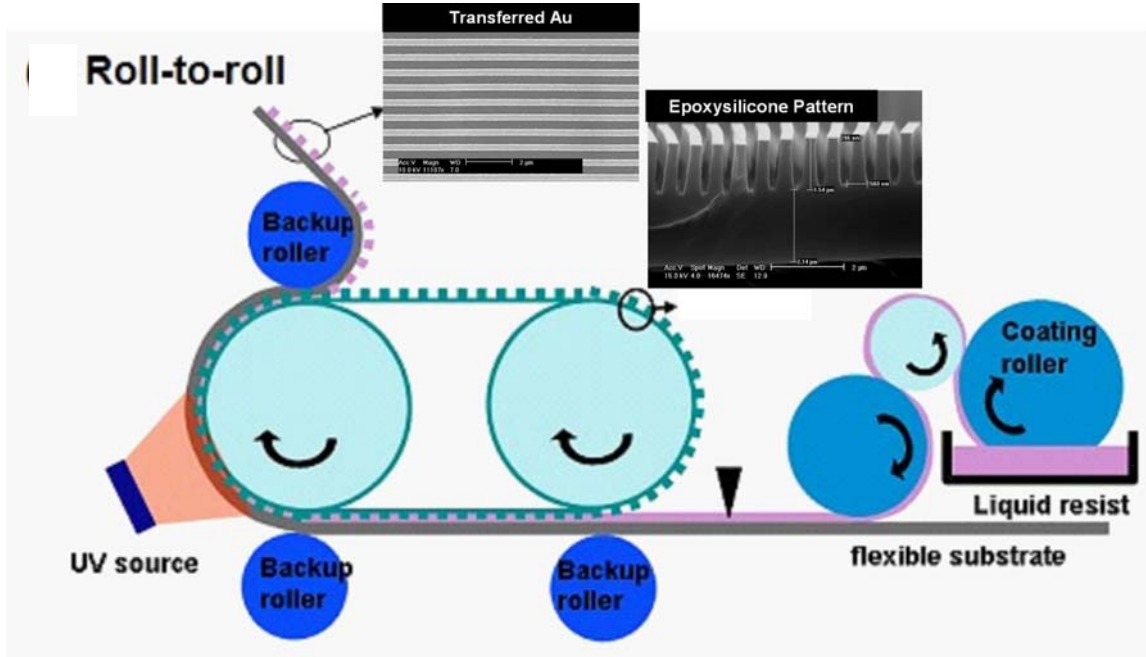
Figure 3-8 Schematics of R2RNIL process.(Courtesy of Se Hyun Ann[54])

For this work, surfactant treated epoxysilicone patterns (inset in Fig. 3-8) with a period of 700 nm and duty cycle of about 50 % on PET substrate were used as a mold and then 40 nm thick Au films are deposited on them. Au films on protrusions of the mold are transferred onto UV epoxy on PET substrates as shown in Fig. 3-8.

3.4 Results and discussion

3.4.1 Transparent Cu electrode on PET substrate

Optical transparency and electrical conductivity, the two most important factors for transparent electrode, were quantified experimentally by measuring the transmittance and the sheet resistance, respectively. Fig. 3-9 shows that the optical transmittance results and photograph of the semitransparent Cu electrode on PET in bent condition, showing the flexibility of the electrode coated substrate.
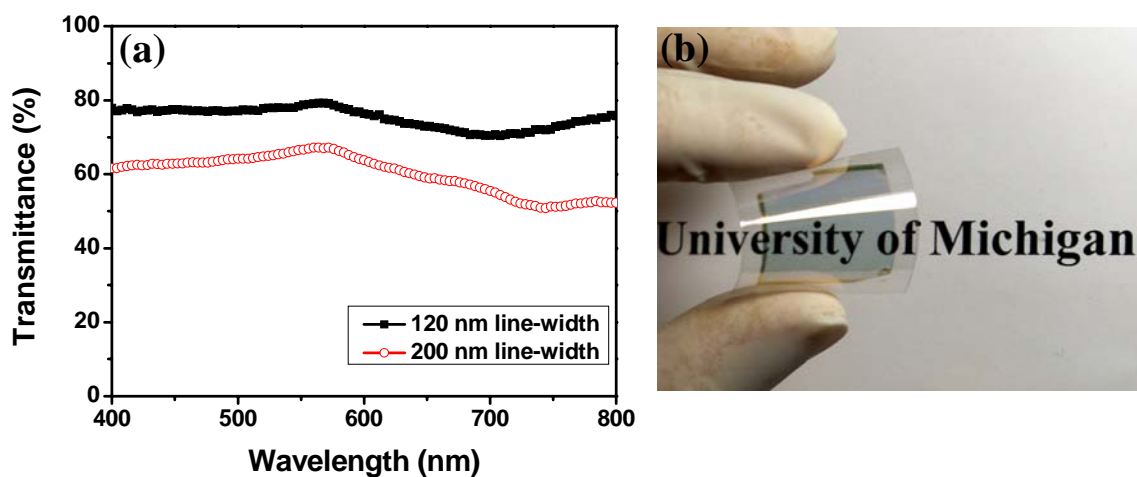
Figure 3-9 (a) The optical transmittance and (b) the photograph of the transparent Cu electrode on PET fabricated by direct transfer from PDMS stamp.

The measured optical transmittance was referenced to PET substrate in this case. As shown in Fig. 3-9, the transparent Cu electrodes are highly transparent in the visible range. The average transmittances are 61 % and 75 % for Cu electrode with a line-width of 200 nm and 120 nm, respectively. The results confirm that the transmittance was increased much by decreasing line-width of the mesh structure. The associated sheet resistance are 10 Ω/□ and 14.8 Ω/□ for line width of 200 nm and 120 nm, respectively. The increased sheet resistance by reducing line-width can be compensated by transferring thicker metal. For transparent metal electrode, the line-width should be narrower for high transmittance which means that the portion of light through narrow metal line is small. Therefore, there is small dependence of transmittance on metal thickness. Simulation on transmittance vs. metal thickness for Cu grating with a line-width of 120 nm shows that the average transmittances in the visible range are 82.4, 80.4, 79.4, 78.7,and 78.1 % for 20, 40, 60, 80, and 100 nm thick transparent Cu electrode, respectively. For Cu thicker

than 40 nm, the average transmittance did not change much because 40 nm thick metals can block the light efficiently. Therefore, it is expected that increasing thickness by a factor of 5 can decrease the sheet resistance by the same order but the transmittance by only slight decrease. It should be noted that wavelength dependency of the transmittance of the semitransparent Cu electrode on PET substrate is different from that on glass substrate shown in Chap. 2. The dip in the transmittance in case of PET substrate was red-shifted compared with that on the glass substrate but the overall trend of the transmittance is similar. 2 nm thick Ti layer was used as adhesion layer for glass substrate. On the other hand, 3 nm thick oxidized Ti layer was used between Cu layer and PET substrate. The wavelength dependence of transmittance is correlated to the plasmon absorption band in the metal which is known to be very sensitive to refractive index change of the adjacent material[55]. From this result, it could be expected that the transmittance dip can be intentionally changed by adjusting the Ti layer thickness for higher transmittance at desired wavelength region. Moreover, it would be possible to make the transmittance in the visible range flatter by tuning refractive index of adjacent material.

3.4.2 Transparent Cu electrode on PEDOT coated PET substrate

The optical transmittance of the fabricated Cu mesh electrode on PEDOT coated PET substrate in the visible wavelength range was measured and shown in Figure 3-10. As a comparison, the optical transmittance of the commercial ITO electrode (Sigma Aldrich, 60 $\Omega/\square$) was also measured and included in the figure. All the transmittance measurement was referenced to air in this experiment.
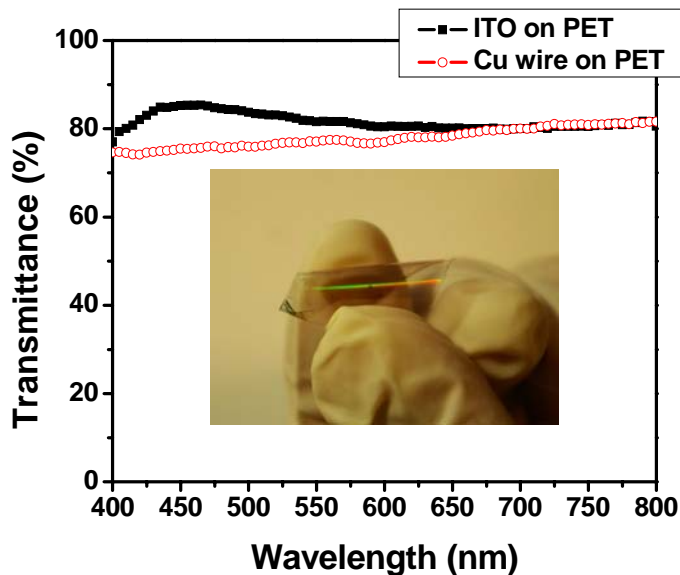
Figure 3-10 Optical transmittance of 40 nm thick Cu nanowire mesh electrode with the sheet resistance of 22 Ω/□ on PET substrate and the commercial ITO electrode on PET substrate (60 Ω/□). Inset: the photograph of the flexible Cu mesh electrode on PET substrate.

ITO has a peak transmittance of 85 % at 465 nm and an average transmittance of 82 % in the whole visible range. The transmittance of the Cu mesh electrode is very flat over the visible region and the average transmittance is about 78 %. The wavelength dependency of the transmittance of Cu electrode was much relieved by reducing the line-width to 70 nm. The measured sheet resistance of the transparent Cu electrode is 22 Ω/□, about three times lower than that of the ITO. One should note that in contrast to the ITO, the sheet resistance of the transparent metal electrode can be reduced further by using thicker metal with little reduction of the transmittance.

The fabricated Cu electrode on PEDOT coated PET substrate was found to be much more flexible than the ITO through the simple bending test and the results are shown in Figure 3-11. In case of the transparent Cu electrode, it can be bent down to a

radius of about 3 mm with no degradation of the conductance. On the other hand, the ITO exhibited that the conductance started to decrease at a radius of ~20 mm. One should note that the conductance of the ITO was measured right after the specific bending radius was reached. At even a radius of ~20 mm the conductance gradually decreased and reached close to zero. Reduced conductance is not recoverable due to the permanent cracks formed in ITO. Micro-cracking in ITO film on the order of 20 μm was observed after bending test.
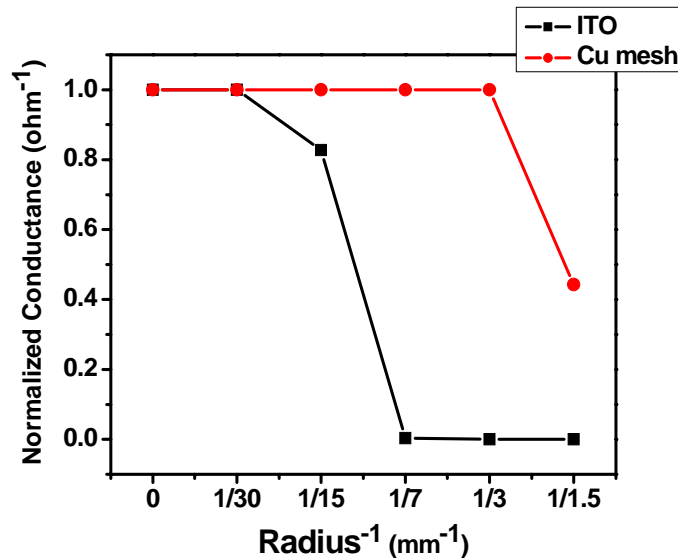
Figure 3-11 Normalized conductance vs. inverse of the radius curve of the Cu mesh and ITO electrode. The Cu mesh electrode showed a superior flexibility and can be bent down to ~3 mm with no degradation of conductance.

3.4.3 Nanopatterned metal electrode on flexible substrates using roll-to-roll nanoimprint process

Fig. 3-12 shows Au nanogratings on PET substrate fabricated by R2RNIL process.
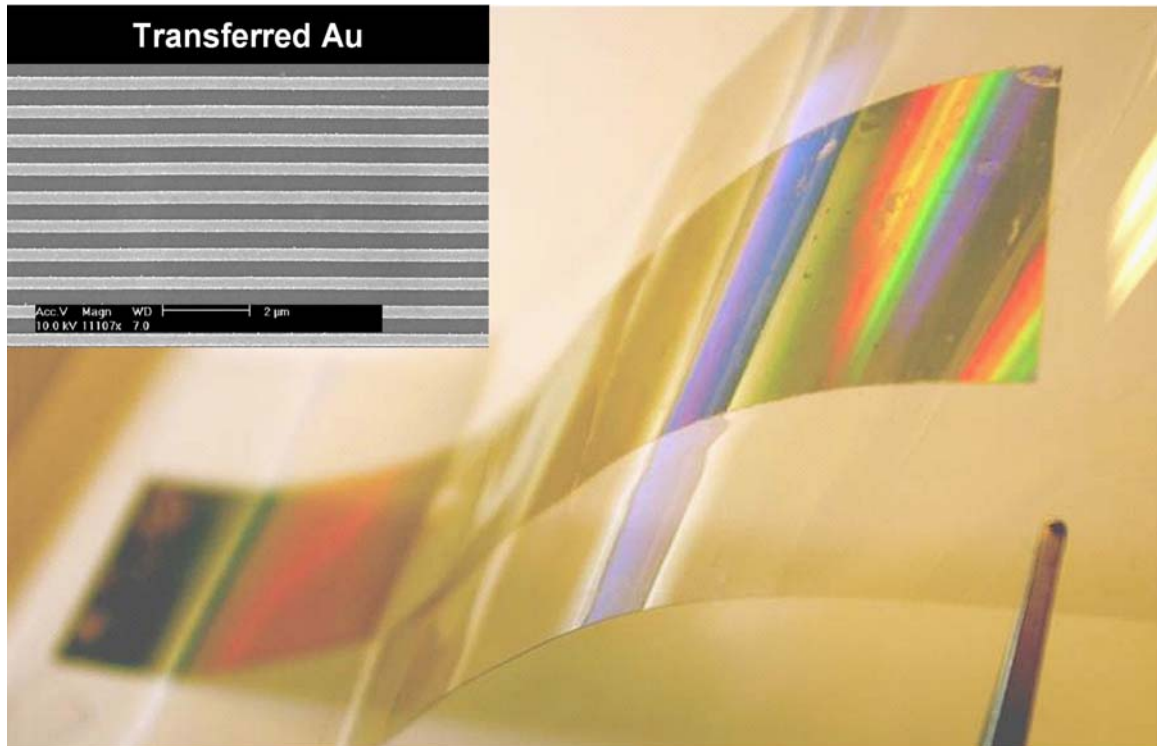
Figure 3-12 Photograph of large area (32 mm x 184 mm) Ag nanogratings on PET substrate. Inset shows the SEM image of fabricated Au gratings.[*]

As shown, large area (32 mm x 184 mm) nanopatterned Au electrodes were successfully fabricated. This result implies that the fabrication of the nanopatterned metal electrode can be easily extended to R2RNIL process, which could help to realize low cost, large area transparent electrode.

3.5 Summary

In this study, transparent Cu electrode on the PET substrate created by nanoscale metal transfer printing was demonstrated. Nanoscale dense metal mesh pattern was successfully replicated by using high modulus PDMS stamp. The fabricated transparent

---

[*] Fabrication of Au nanogratings using R2RNIL process was done by Se Hyun Ahn.

Cu electrode showed high transmittance in the visible range and good electrical conductivity. The transparency of such an electrode structure can be increased without sacrificing the overall conductivity by using narrower and thicker metal film. This characteristic is another advantage over an ITO electrode, in which the sheet resistance has to be compromised to achieve high transmittance. As demonstrated, metal transfer printing is the simple method and can be easily expanded to low cost, large area fabrication such as R2RNIL process[53,54]. Fabricated Cu mesh electrode showed a greater flexibility than conventional ITO electrode with high optical transmittance and electrical conductance. Therefore, the use of cheap material such as Cu and simple fabrication method could help to realize low cost, large area flexible organic optoelectronic devices such as OSCs and OLEDs.

Chapter 4

Metal Transfer Assisted Nanolithography on Rigid and Flexible Substrates

4.1 Introduction

A low cost and efficient lithography technique that can produce nanometer scale feature is essential for future plastic optoelectronics, biotechnology, and other technical fields. Nanoimprint lithography (NIL)[36], metal transfer printing[47-49], and soft lithography[56] (e.g. microcontact printing) are potential candidates because they require only simple tools such as molds, stamps, presses, and/or self-assembled monolayers (SAMs) but can create nanometer scale pattern efficiently. Microcontact printing uses elastomeric stamps such as PDMS to form patterns of SAMs on the surfaces of substrates such as Au and Ag. Metal patterns are then created by selective wet etching[57, 58]. In metal transfer printing, the nanometer scale metal pattern is transferred from stamps to substrates directly by means of covalent interactions or difference in surface adhesion properties between the metal and the substrates. Organic devices such as organic light emitting diode and organic thin film transistors were recently demonstrated using metal transfer technique. However, several issues need to be addressed before it can be used as a lithography technique for future flexible electronics. First, the previously demonstrated

method requires either a specific covalent interaction or very flat plastic surface for faithful transfer printing. Second, the technique works efficiently only for metals with weak adhesion to stamp (e.g. Au). Also the adhesion to substrates is relatively poor without relying on covalent interaction. In future flexible optoelectronics, a variety of metals and high adhesion characteristic[59] may be required as electrode materials on flexible substrate. In this work, we demonstrate an alternative nanolithography technique based on metal transfer printing, in which the transferred metal acts as a etch mask for pattern transfer to the substrate. There are several advantages of this nanolithography technique. First, it can be applied to plastic substrate as well as rigid substrate due to the use of an intermediate polymer layer, and the low pressure and temperature in the metal transfer process. Second, it can create both large (micron size and larger) and small (nm size) pattern at the same time which are challenging for conventional NIL[60]. Third, the naturally formed undercut in polymer layer after oxygen RIE makes lift-off process of nanometer scale size very easy. Fourth, a variety of metals can be used by using a thin layer of adhesion metal (e.g. Ti) for high adhesion characteristic of metal electrode on substrates. Lastly, this lithography can be potentially extended to roll-to-roll processing due to the use of flexible stamp.

4.2 Principle of metal transfer assisted nanolithography

The technique developed was motivated by the work on the fabrication of metal mesh pattern using the metal transfer printing process[47]. The metal transfer printing was shown to be very effective for the production of dense nanoscale metal mesh pattern on a flexible substrate. However, there are a few drawbacks which prevent that from

using as a general lithography technique. There is a limitation in choosing substrate when direct metal transfer on substrate is used. Even though the use of an interfacial polymer layer can solve that problem, it causes another issue. It is very hard to apply another lithography step (e.g. Photolithography and NIL) to build additional structure because the interfacial polymer is attacked by the pattern transfer process such as wet chemical and dry etching. In developed metal transfer assisted nanolithography as shown in Fig. 4-1, metal is transferred onto the polymer layer and the transferred metal act as a etch mask of the polymer layer underneath instead of using as an electrode. After removing the exposed polymer layer using oxygen reactive ion etching (RIE), another metal acting as an electrode is deposited and lifted-off. Any kinds of metal electrode can be fabricated using this technique by depositing different metal. Moreover, there is no limitation in choosing substrate, metal, and additional lithography on top of the fabricated electrode.
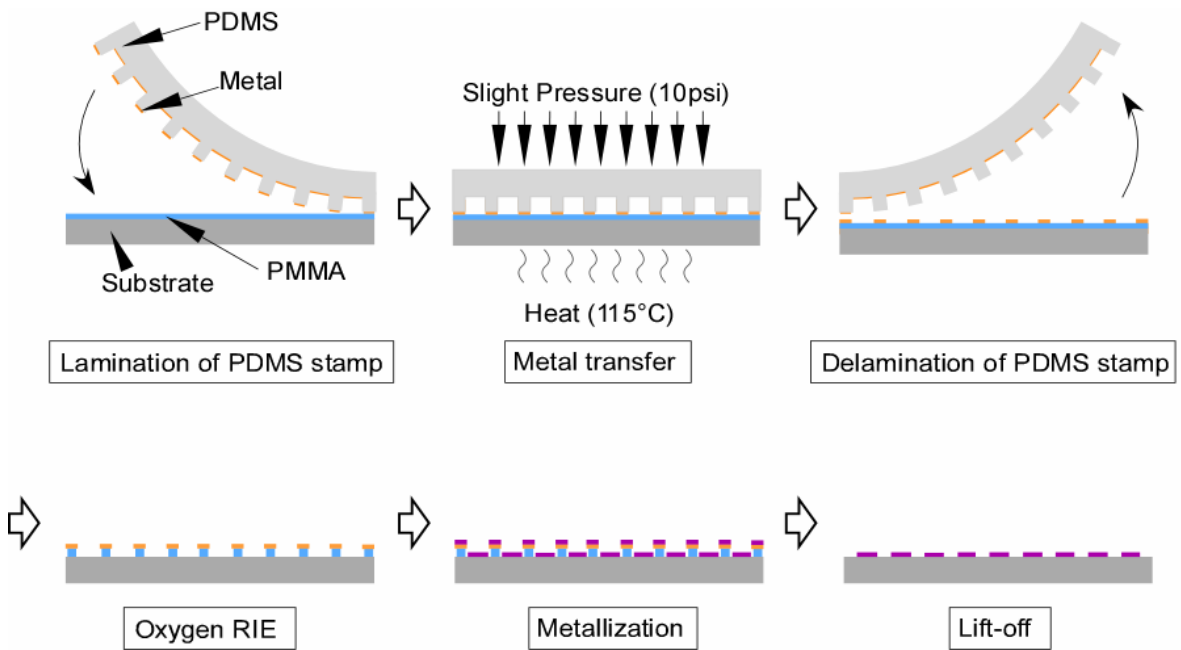
Figure 4-1 Schematic diagram of metal transfer assisted nanolithography

4.3 Experimental details

4.3.1 Fabrication of PDMS stamp

The details of the fabrication of the PDMS stamp in nanoscale can be found in Chap.3. The fabricated PDMS stamp has a period of 220 nm and line-width of 100 nm. Fig. 4-2 shows SEM images of the fabricated PDMS stamp.
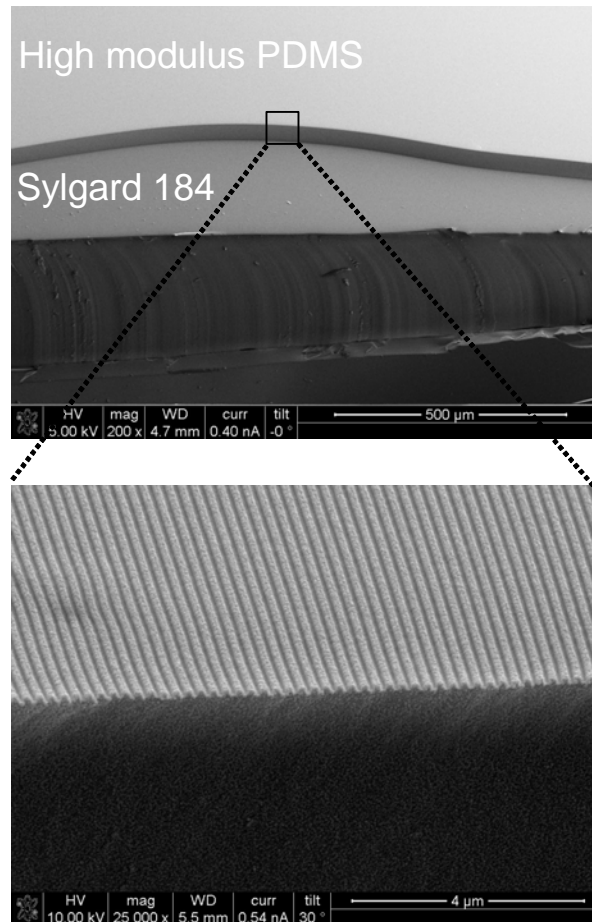
Figure 4-2 SEM images of the fabricated PDMS stamp in this work. The period is 220 nm, the line-width is 100 nm, and the depth is 100 nm.

4.3.2 Metal transfer assisted nanolithography

Resist template for the fabrication of PDMS stamp was first prepared by conventional NIL and PDMS stamp was fabricated as described in Chap. 3. The replicated pattern on the PDMS stamp has a period of 220 nm and a line-width of 100 nm. After the fabrication of the PDMS stamp, a 10 nm thick Au and 5 nm thick Ti were deposited sequentially on the PDMS stamp by e-beam evaporation at a rate of 2 Å/sec. As shown in Fig. 4-1, an intermediate polymer layer is required for metal bonding and the pattern transfer by O_2 RIE. Spin-coated Poly(methyl methacrylate) (PMMA) was used for this purpose. The metal coated PDMS stamp was then laminated onto a 180 nm thick PMMA layer on the substrate. For this work, SiO_2, glass, PET substrate were used as substrates. A slight pressure of 10 psi was applied to the stamp to ensure an intimate contact between the metal layer on the PDMS stamp and the PMMA layer. At the same time, a temperature of 115 °C was applied for 2 min to make PMMA sticky for better adhesion to the metal layer. After cooling down to room temperature, removing the PDMS stamp from the PMMA layer left the metal grating on the PMMA layer from the protrusions on the PDMS stamp. This is an additive process that relies on the difference in the surface adhesion characteristics between the PDMS-metal and the metal-PMMA interfaces. It has been known that PDMS has much lower surface energy than PMMA[50]. Moreover, a temperature above Tg of the PMMA will increase the adhesion ability of the PMMA to the transferred metal patterns with high yield. After the metal transfer, the PMMA layer was etched by oxygen RIE with transferred metal as the etch mask. "LAM 9400", commercially available plasma etcher was used for removing the exposed PMMA layer. The etching condition for pattern transfer is the power of 100 W for TCP and 30 W for bias; the pressure of 20 mT; the O_2 flow of 20 sccm. The etch rate

for PMMA is 6 nm / sec. 180 nm thick PMMA was etched for 40 sec (30% over etching). Usually, the oxygen RIE with low power can not etch the metal at al so we assume that the etch selectivity between the gold/titanium and the PMMA is almost infinity. This should be true for short period of time of oxygen RIE used in this work. Therefore, due to the large difference in the etch rate between the metal and the PMMA, an undercut feature was formed naturally below the metal mask, which made lift-off process of nanoscale pattern very easy.

4.2.3 Fabrication of nanoscale metal particle arrays

As an expansion of metal transfer assisted nanolithography, dense nanoscale metal particle arrays can be easily fabricated from a nano-mesh template produced by transferring metal grating twice sequentially. For this process, the first metal grating was transferred as described in above. The second metal grating was then transferred with an angle (e.g. 90° or 30°) with respect to the first grating. A different period of grating can also be used for the second metal transfer, which can create metal particle arrays with different shapes and sizes. One difference in the metal transfer process between the first and the second metal grating transfer is the pressure. To make an intimate contact between the second metal grating and the exposed PMMA region between the first transferred metal gratings, higher pressure (e.g. 20 psi) was needed.

4.2.4 Measurement of Localized Surface Plasmon Resonance (LSPR) of patterned metallic nanoparticles

Localized surface plasmon resonance (LSPR) are collective charge-density oscillations excited by an incident light of certain frequency, and exhibit a high-degree of

tunability based on the shape, size, composition and the spacing of the nanoparticle system. The ability of noble metal nanoparticles to transduce dielectric changes through the shift of their LSPR has attracted tremendous interest for sensor applications. Absorbance measurement was performed to obtain the LSPR spectra of the metal nanoparticles. We used a Nikon TE300 Eclipse inverted microscope with transmitted light coupled into an Ocean Optics fiber-coupled spectrometer using an achromatic lens. For polarization dependent extinction measurements, a linear polarizer mounted in a rotating module was aligned to the optic-axis of the microscope directly above the sample stage. All measurements were taken using normal incident light referenced to air.

4.2.5 Reduction of the pattern line-width

Another extension of the technique is the reduction of the feature size of the pattern (Fig. 4-3). We used dense line and spacing pattern as an example to illustrate such a process. As shown in Figure 4-3, by angled-evaporation (~20°) metal was deposited only on top and the two sides of the grating on the PDMS stamp. This process was also referred to as the shadow evaporation technique. Evaporated metal was then transferred onto PMMA layer as described in section 4.3.2.
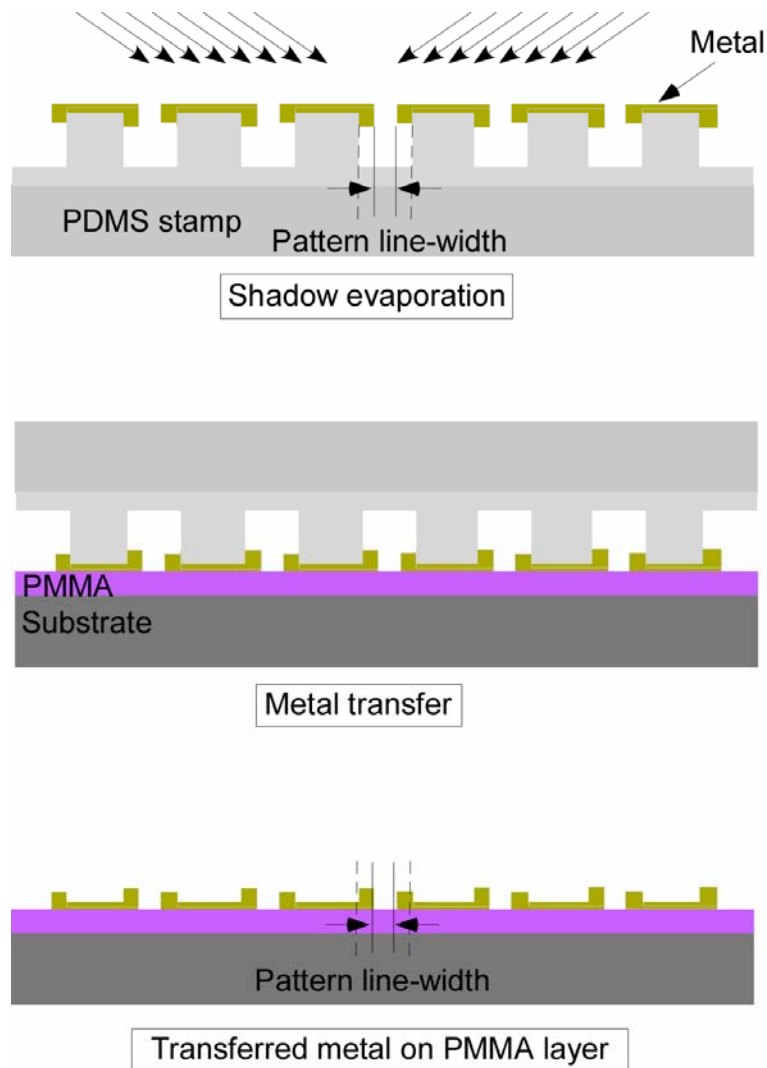
Figure 4-3 Schematic of shadow evaporation of metals to reduce pattern line-width.

After the metal transfer to the PMMA layer, the pattern can be further transferred to the substrate as shown in Fig. 4-1 with same condition. The resulting pattern line-width is reduced by the thickness of the metal on the PDMS grating sidewall during shadow evaporation. In our experiment, 25 nm thick Au and 10 nm thick Ti were deposited at one direction and 25 nm thick Ni and 10 nm thick Ti were deposited at the other direction. Nickel was needed to bond between first metal (Au/Ti) and second metal (Ni/Ti) so all the metals were transferred. When gold was used as second layer, only second layer was

transferred due to the poor adhesion property of Au. The reduction of pattern line-width is a simple yet effective approach for producing smaller feature sizes.

4.4 Results and discussion

Figure 4-4(a) and 4-4(b) show the SEM images of the transferred metal grating pattern on the PMMA layer with a period of 700 nm and 220 nm, respectively. Figure4-4(c) shows the cross section view after O_2 RIE of figure 4-4(b). The undercut feature, formed naturally during O_2 RIE due to the different etch rate between the metal and the PMMA, was clearly visible and made a subsequent lift-off process very easy. After metallization and lift-off, 220 nm pitch dense metal grating with a line-width of 100 nm was achieved on the PET substrate and shown in Figure 4-4(d). The line-width of the final metal grating follows the dimension of the trench patterns on the PDMS stamp, which shows that the resolution of metal transfer assisted nanolithography is mainly dependent on the minimum feature size achievable on the PDMS stamp. It is expected that the resolution of this lithography can be further enhanced by fabricating high resolution PDMS stamp. In microcontact printing, one of the useful techniques for patterning metal, metal pattern is formed by selective wet etching with SAM layer as a mask. However, the control of the line-width and resolution is not easy when relying on wet etching. Moreover, it is hard to fabricate thick and dense nano-meter size metal pattern because of the isotropic characteristic of the wet etching.
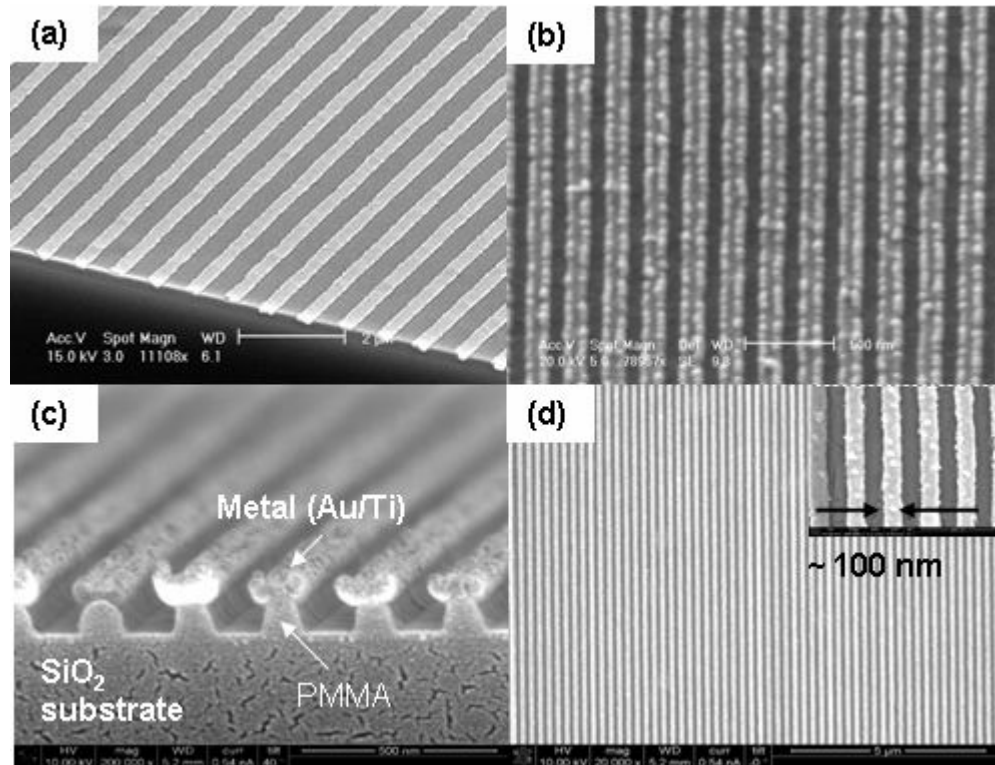
Figure 4-4 SEM images of the transferred metal grating pattern onto PMMA layer with a period of (a) 700 nm on the SiO₂ substrate and (b) 220 nm on PET substrate, (c) after O₂ RIE of (b) in case of SiO₂ substrate, and (d) after metallization and lift-off process of (c)

Nanosize metal particle arrays were created by transferring two metal gratings sequentially. After the first metal transfer, the second metal grating can be transferred with different angles to the first grating to generate various shapes of metal particle arrays. As shown in Figure 4-5(a) and 4-5(b), the second metal grating was transferred orthogonal and about 30° to the first grating, respectively. To obtain different shape or dimension of the metal nanoparticle array, different period of grating (e.g. 700 nm) can be used for the second metal transfer as shown in Figure 4-5(c). Figure 4-5(d)-4-5(e) show the corresponding SEM images after metallization and lift-off process of Figure 4-5(a)-4-5(e), respectively.
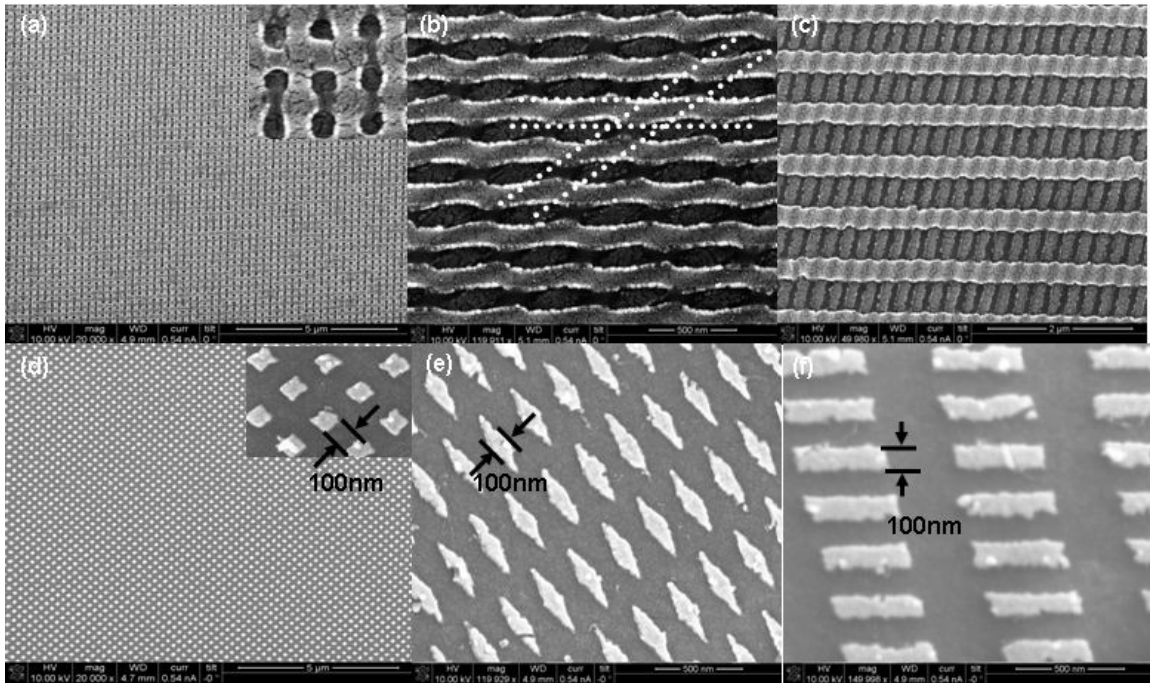
Figure 4-5 SEM images of the sequentially transferred two metal gratings (a-c) and the corresponding nanosize metal particle arrays on PET substrate after metallization and lift-off process (d-f). Two 220 nm period gratings were transferred orthogonally (a) and with an angle of ~30° (b). (c) A 700 nm pitch grating was transferred orthogonally to a 220 nm period grating. (d-f) Nanosize metal particle arrays with different shapes such as square (d), diamond (e), and nanobar (e) after metallization and lift-off process of (a-c)

The large area and dense metal particle arrays in the form of nanosquare, nanodiamond, and nanobar were created on PET substrate with high yield. The typical sample size is approximately 1 inch^2 and only limited by size of the original PDMS stamp. Therefore, metal transfer assisted nanolithography offers another effective route to fabricate large area and uniform plasmonic arrays for sensor application.[55] The localized surface plasmon resonance spectra of the nanosquare are shown in Fig. 4-6.
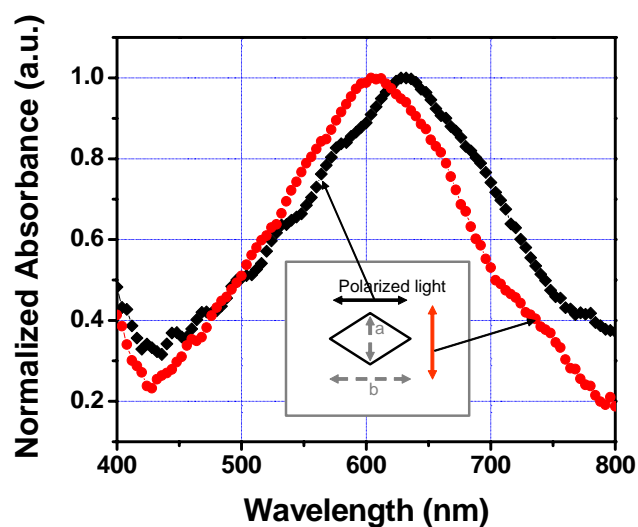
Figure 4-6 Localized surface plasmon resonance spectra of nanosquare arrays obtained for linearly polarized incident light aligned with shorter axis a (●), and longer axis b (♦).

The two curves correspond to extinction spectra measured by using polarized light of two orthogonal polarizations, one along the longer axis (b) and the other shorter axis (a). The lower energy peak associated with the LSPR along the longer axis was consistent with previous reports. The distinct polarization dependence is due to the aligned orientation of the particle array.

As described earlier, the pattern line-width can be further reduced by depositing metals on the side of the PDMS grating. Figure 4-7 shows the SEM and photograph images of the metal grating fabricated using this technique, where the line-width of the pattern was reduced to 50 nm from the original 100 nm.
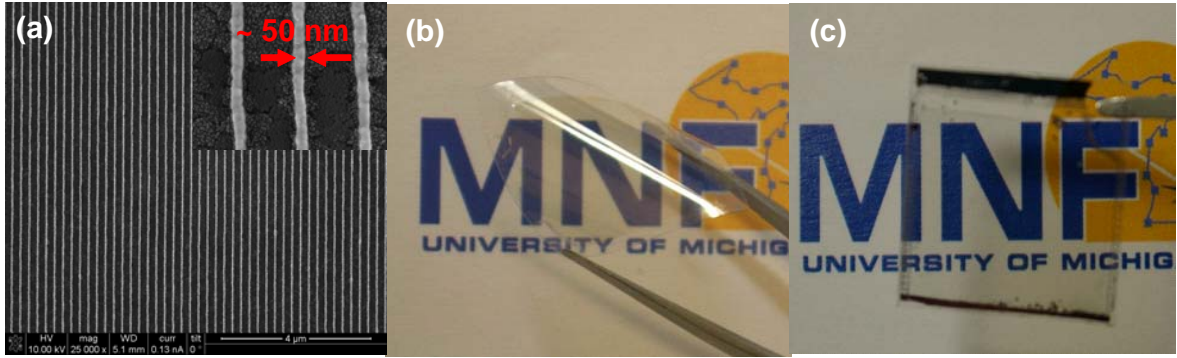
Figure 4-7 (a) SEM image of the metal grating on PET substrate after line-width reduction. The inset shows is a zoom-in view showing that the line-width was reduced to 50 nm. (b) and (c) photographs of the transparent metal electrode on PET and glass substrates using metal transfer assisted nanolithography, respectively.

The maximum line edge roughness of the fabricated 50 nm wide metal grating is less than 10 nm based on Fig. 4-7 which means that the sidewall roughness after angled-evaporation on PDMS stamp is in the same order. As shown in Fig. 4-7(b) and 4-7(c), the reduction of line-width of the metal grating may find useful application in transparent metal electrode[35] in which the line-width needs to be reduced for high optical transmittance.

4.5 Summary

In this study, metal transfer assisted nanolithography was demonstrated. Due to the use of an intermediate polymer layer, and the low pressure and temperature in the process, this lithography technique can be used on flexible substrate as well as hard substrate. Transferred metal layer was used as etch mask for pattern transfer to substrate. Naturally formed under-cut feature after O_2 RIE greatly facilitated the lift-off process and ensured high yield patterning over large area. Large area and dense nanosize metal

particle arrays with different sizes and shapes were created on flexible substrate with high yield by transferring two metal gratings. Pattern line-width was reduced to 50 nm in metal grating by depositing metals on the PDMS grating sidewall during shadow evaporation. As demonstrated, the metal transfer assisted nanolithography can be readily used as a low-cost and high resolution lithography technique on any substrate including flexible and hard substrate.

Chapter 5

Organic Light Emitting Diodes (OLEDs) with Transparent Cu electrodes

5.1 Introduction

Organic light emitting diodes (OLEDs) are promising for full color, full-motion flat panel display applications[1-3] since they have several advantageous features such as ease of fabrication, low cost, light-weight, bright self-emission, wide-viewing angle, and possibility for flexible display. The basic OLED structure consists of a number of organic semiconductor layers sandwiched between a cathode and an anode. For efficient electron injection into the organic layers, low work function materials are required for the cathode. A very thin LiF layer with thick Al capping[61] is widely used for this purpose. For the anode, the indium tin oxide (ITO) is the predominant choice because it offers transparency in visible range as well as electrical conductivity[7-9]. However, several aspects of ITO are far from optimum for high performance OLED. It is known that the migration of indium and oxygen from ITO into organic semiconductors during operation of OLED causes device degradation[10, 11]. The electrical properties of ITO depend much on the film preparation[12, 13]. Rough surface of the deposited ITO film and the work function of ITO, ~4.7 eV, limit the efficiency of the hole injection[14]. The typical sheet resistance for a 100 nm thick ITO, 20~80 $\Omega/\square$, is still high so it causes voltage drop

along the addressing line resulting in limiting the operation of a large area passive matrix OLED array[15]. Moreover, the cost of ITO escalates in recent years because of the price jump of the indium element. Several alternative materials such as TiN[62], Al-doped ZnO[22], and fluorine tin oxide[18] have been investigated as anode instead of ITO, however none are optimal as anode in OLED because they suffer from either lower work function than ITO or lower conductivity. Other transparent conducting oxides such as Ga-In-Sn-O (GITO), Zn-In-Sn-O (ZITO), Ga-In-O (GIO), and Zn-In-O (ZIO) which have higher work function than ITO and similar electrical conductivity to ITO have also been examined as an OLED anode[63]. However, they are potentially problematic because of the indium element which possibly diffuses into the organic layer in the OLED and makes those electrodes expensive. Besides these materials, several metals with high work function such as Au[14], Ni[31], and Pt[32] were investigated as anodes for OLEDs. In these cases, metal was used to modify the surface of ITO electrode or as anode for top emitting devices. Surface modified thin Ag film[33, 34] was used as semi-transparent electrode instead of ITO but its transparency was low. Recently, carbon nanotube films were investigated as transparent, conductive electrode[27, 29, 30, 64] but they have high sheet resistance which may limit the device performance. In this work, we evaluate the potential of the transparent Cu electrode as an OLED anode. The fabricated transparent metal electrode offers several advantages over ITO for OLED applications. First, several problems associated with ITO can be eliminated, such as device degradation by indium diffusion and high cost. Second, efficient hole injection to the organic semiconductor can be obtained by choosing metals with high work function, such as Au or Pt. Third, transparent metal electrode is potentially suitable for top emitting device and tandem structure. Last but not the least, output efficiency of OLED can be enhanced by

preventing waveguiding in ITO layer due to its high refractive index, which is the one of the limitations to the external efficiency of OLEDs[65], and by forming two-dimensional hole array with proper periodicity[66, 67].

5.2 Experimental details

5.2.1 Fabrication of OLEDs on glass substrates

To demonstrate the potential use of the transparent Cu electrode as transparent conducting electrode for optoelectronic devices, organic light emitting diode (OLED) is fabricated using such electrode as anode. Though Au is preferred due to its high work function for efficient hole injection, results of using Cu as anode material is presented because of its much lower cost and has a similar work function to ITO (~4.7 eV). Cu material, being one of the cheapest metals, is well suited for practical organic electronic applications. 40 nm thick semi-transparent Cu electrodes with 200 nm and 120 nm line-width are chosen as anodes in OLED. Fig. 5-1 shows the SEM image of the transparent Cu electrode on glass substrate.
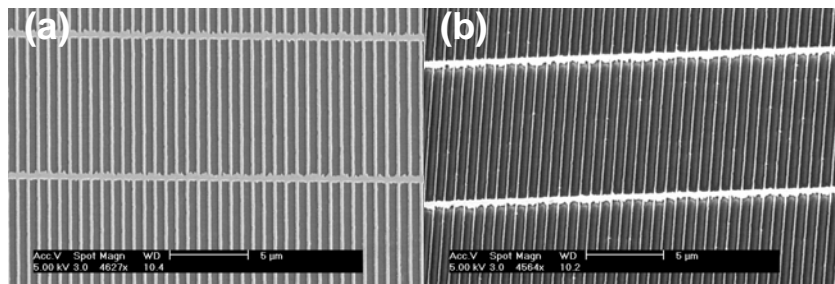
Figure 5-1 SEM images of the transparent Cu electrodes with line-widths of (a) 200 nm and 120 nm, respectively.

Transparent Cu anodes on glass are cleaned in acetone and IPA under sonication for 20 min each and then exposed to brief (30 s) oxygen plasma (80 W, 250 mT, 17 % O_2) to thoroughly remove organic residue. The plasma treatment also makes the metal anode more hydrophilic for easy spin coating of the hole transport layer, PEDOT:PSS. Commercially available high resistivity PEDOT:PSS, Baytron CH8000, was used. Filtered PEDOT:PSS is then spin-coated on Cu anode at 1.5k rpm for 30 s which produces an 80 nm thick layer and then baked at 120 °C for 1 hr. Next the emissive organic layer poly[2-(2-etylhexyloxy)-5-methoxy-1,4-phenylenevinylene](MEH-PPV) (0.5 % by weight dissolved in toluene) is spin coated after filtration on PEDOT layer at 1 krpm for 30 s which gives 50 nm thick layer and then baked in vacuum oven for 24 hrs at ambient temperature. Thermal evaporation of 1 nm thick LiF followed with 100 nm thick Al through shadow mask completes the OLED device fabrication. Fig. 5-2 shows the fabricated OLED schematic.
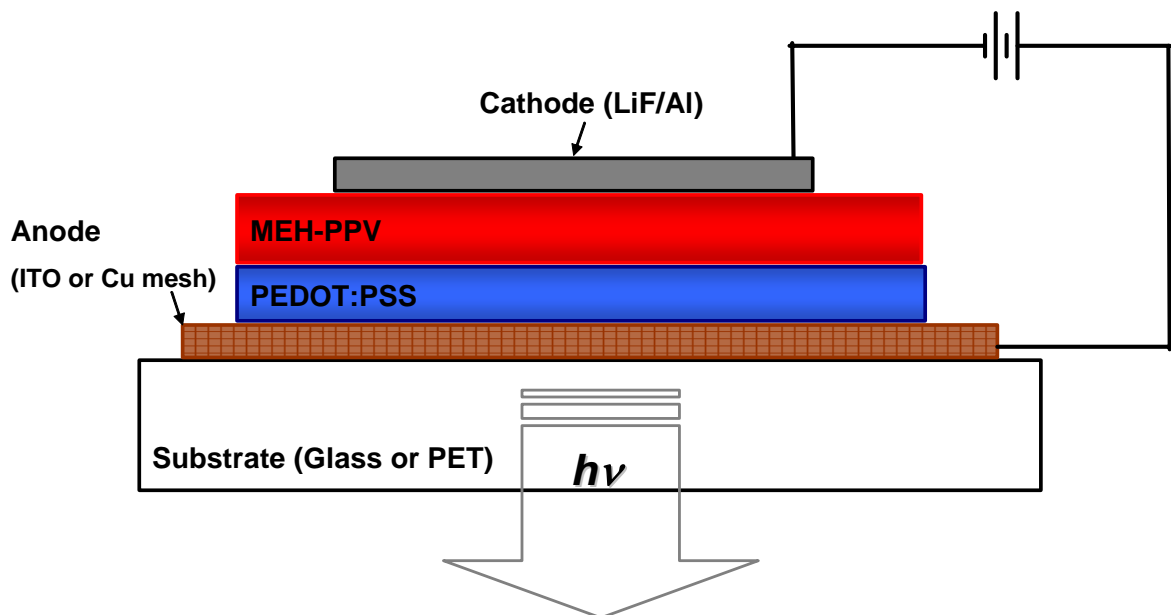
Figure 5-2 Fabricated OLED device schematic. The OLED device consists of a transparent Cu mesh electrode as the anode, PEDOT:PSS as the hole transport layer, MEH-PPV as the emissive layer, and LiF/Al as the cathode.

5.2.1 Fabrication of OLEDs on PET substrates

A flexible OLED was also fabricated using such an electrode as the anode. Cu is well suited for practical flexible display for which light-weight and low cost fabrication are essential because of its work-function (ca. 4.7 eV) and cost. Transparent Cu electrode with a thickness of 40 nm and line-width of 200 nm was chosen as anode in the OLED in this experiment. Fig. 5-3 shows the SEM image of the transparent Cu electrode used in this experiment, fabricated by Cu transfer printing on PET substrate.
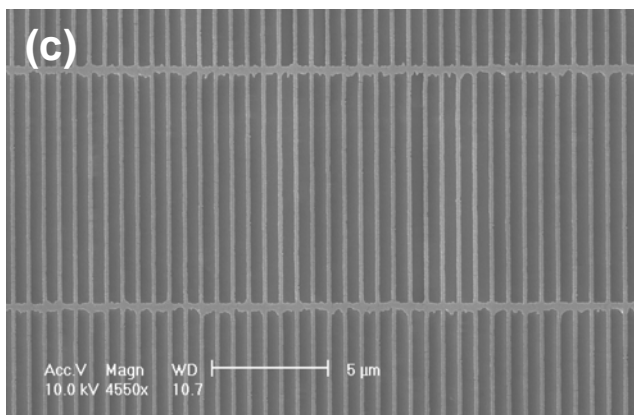
Figure 5-3 SEM image of the transparent Cu electrode with a line-width of 200 nm.

The flexible OLED device structure is same as that built on glass substrate. Device fabrication details are similar to the fabrication of OLED on glass substrate. The only difference was that the PEDOT layer was baked at 60 °C for 4 hrs in nitrogen purged oven instead of 120 °C because PET has low Tg, 79 °C.

5.3 Results and discussion

Fig. 5-4 shows the current density vs. voltage and electroluminescence

characteristics of the OLEDs using transparent Cu anodes on glass substrate.
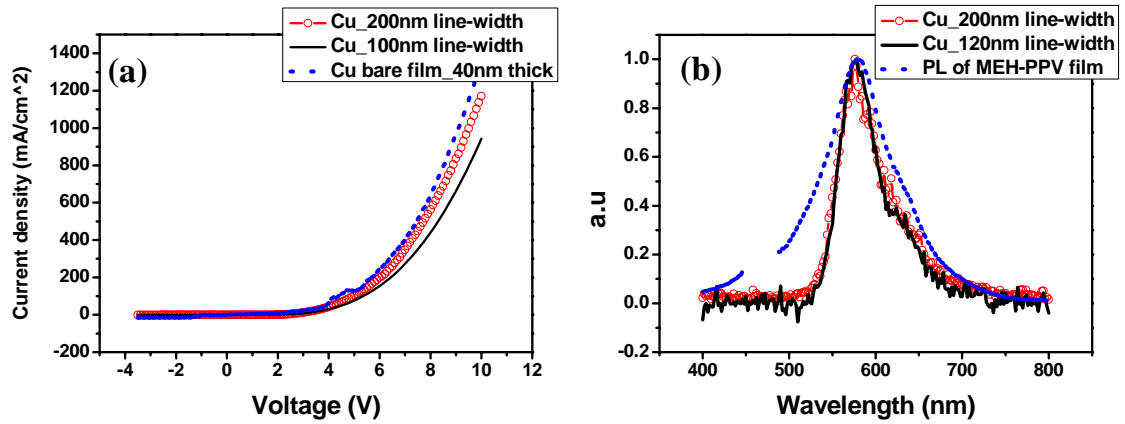
Figure 5-4 (a) Current density vs. applied voltage and (b) electroluminescence characteristics of OLEDs with semi-transparent Cu anode.

The junction exhibits good rectifying characteristics. The turn-on voltages of these OLEDs are similar to the control samples made with ITO electrodes. The OLED made with 120 nm line-width Cu anode shows a slightly higher turn-on voltage than that made with 200 nm line-width Cu anode and as a result lower current density at given bias after the device is turned on. As a comparison, the current density vs. voltage characteristic of an OLED made with 40nm thick continuous Cu film as anode is also shown in Fig. 5-4(a). It shows similar characteristic to OLED made with the nanoimprinted Cu anode, only with a slightly higher current density at given bias. From these results, we can deduce that the overall mesh fill factor does not significantly affect the device's electrical performance. Both devices show strong electroluminescence peaked at 577 nm, which is the same as the photoluminescence peak of MEH-PPV as shown in Fig. 5-4(b). Though we do not have a set up to quantify the total output power of these OLEDs, to naked eyes the device made with transparent Cu electrode is as bright

as the control sample made using ITO electrode. Upon optimization, such semi-transparent metal electrode could be used to replace the ITO anode.

Fig. 5-5 shows the current density versus voltage and the photograph showing light emission from the flexible OLED made with transparent Cu electrode on the PET substrate fabricated by metal transfer printing.
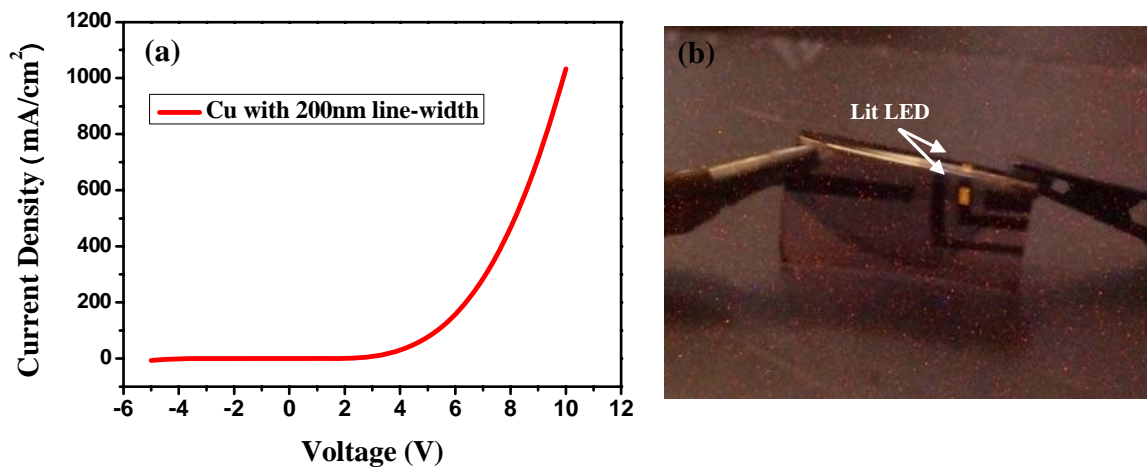
Figure 5-5 (a) Current density versus voltage and (b) the photograph showing light emission from the OLED made with semitransparent Cu as transparent anode in bent condition.

The junction also exhibits good rectifying characteristics. The electrical characteristics of OLED made with transparent Cu electrode are similar to those in literature[68] with same organic material and ITO electrode. The turn on voltage is around 5V and devices have similar current density at given bias after devices are turned on. Upon optimization, such transparent metal electrode could be used to replace the ITO anode, and with an enhanced flexibility on plastic substrate[59, 69].

5.4 Summary

As an application of the transparent metal electrode, OLEDs were demonstrated using transparent Cu electrode as anode to replace the conventional ITO electrode on both flexible and hard substrate. They showed good rectifying characteristic and comparable electroluminescence to ITO device. The work function of an anode can be easily changed by choosing different metal materials in case of transparent metal electrode which provide more flexibility in studying the effect of anode work function on device behaviors. Transparent metal electrode is also potentially suitable for top emitting device and tandem structure. Moreover, output efficiency of OLED can be enhanced by preventing waveguiding in ITO layer and by forming two-dimensional hole array with proper periodicity. Therefore, transparent metal electrode is an attractive and potentially practical solution for organic light emitting devices. As a future work, the quantitative analysis the OLED made with transparent metal electrode and conventional ITO electrode is needed.

Chapter 6

Organic Solar Cells (OSCs) with Transparent Metal Electrodes

6.1 Introduction

Cost effective and highly efficient renewable energy is becoming ever more important in our age of rising energy prices and global climate change. Solar energy is a non-exhaustible and green energy. Organic solar cells (OSC) have the merits of low cost and simplistic fabrication in addition to compatibility with flexible plastic substrates over large areas.   They have therefore been considered a promising energy conversion platform for clean and carbon-neutral energy production[4, 42].   In recent years, the power conversion efficiency (PCE) of OSCs based on conjugated polymers has steadily increased through improved energy harvesting, enhanced exciton separation through improved device structures[70], and optimization of processing parameters such as solvent evaporation time[71] and annealing conditions[72, 73].   Most of OSCs have been built on indium tin oxide (ITO) substrates because ITO offers transparency in the visible range of the electromagnetic spectrum as well as good electrical conductivity. However, ITO is not an optimum electrode for solar cell applications because it has been reported that the band structure of ITO hinders efficient photocurrent generation[16]. Moreover, the poor mechanical stability of ITO can cause device failure when an ITO-

coated flexible substrate is bent[17]. In addition, the limited supply of indium and the increasing demand from the rapidly expanding display market have increased the cost of ITO drastically, which potentially prevents the realization of low cost and large scale OSC fabrication. Therefore, there is a strong need to find an alternative material to replace ITO as a high transparency electrode. Some recent examples that have been investigated are nanotube networks[29, 30, 74, 75] and Ag wire grids[76, 77].

In this work, organic solar cells with high transparency metal wire grid electrodes are demonstrated. The high transparency metal electrodes have several advantages over other highly transparent electrodes including ITO for organic solar cell applications. First, the work function of nanopatterned transparent metal electrode can be easily tuned by choosing different metal materials, which allows systematic studies of the effect of the electrode work function on the device performance. Second, a high electrical conductivity can be achieved without seriously compromising the transparency[35]. Third, the light absorption and the resulting power conversion efficiency of OSC can possibly be increased by means of a light trapping phenomenon induced by the grating structure[78-81]. Lastly, large area organic solar cell having a transparent metal electrode could be realized at a low cost by using a newly developed roll-to-roll nanoimprint technique[53]. It is demonstrated that the power conversion efficiency of OSCs having nanopatterned metal electrodes (e.g. inexpensive Cu material) is comparable to that of the analogous cells using high performance ITO electrode for both glass and PET substrate. It is also shown the effect of the anode work function on the OSC's fill factor (FF) and the photocurrent. A simple design principle to make suitable transparent metal electrodes is discussed.

68

6.2 Experimental details

6.2.1 Fabrication of OSCs on glass substrates

40 nm thick transparent metal (Au, Cu and Ag) electrodes and ITO on glass substrate were cleaned in acetone and isopropyl alcohol (IPA) under sonication for 30 min each. ITO coated glass was purchased from Delta Technologies, LTD. The transparent metal electrode used in this work (Fig. 6-1) has a line-width of 70 nm on glass substrate.

Acc.V	Spot	Magn	WD	5 µm
20.0 kV	4.0	5061x	7.0	
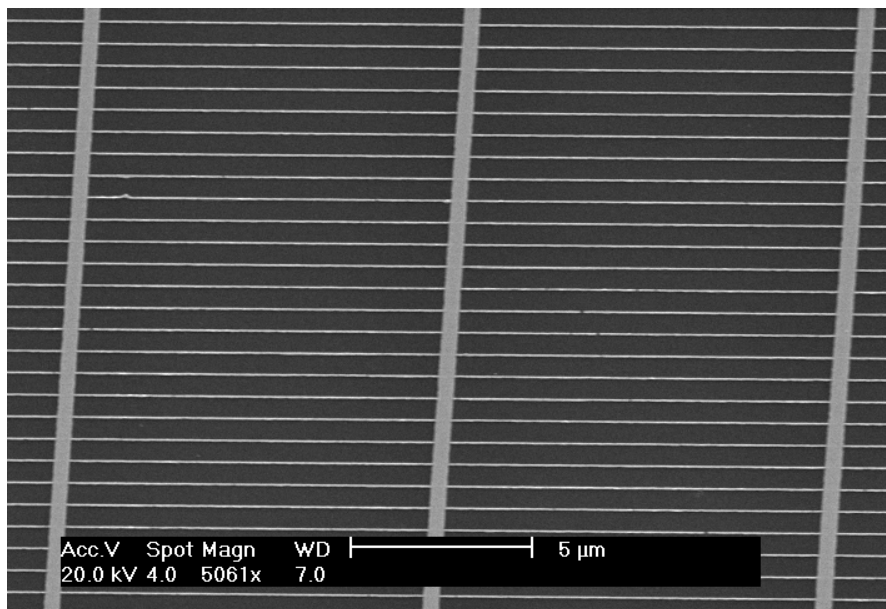
Figure 6-1 SEM image of the transparent metal electrode used as anode for the fabrication of the organic solar cell. The line-width is 70nm for 700nm period of grating.

Cleaned substrates are then transferred to N_2 purged glove box, and filtered PEDOT:PSS (Baytrom PH 500) purchased from H.C. Starck was spin-coated onto the metal electrode at 3000 rpm for 30 s, producing a 95 nm thick layer and then baked at 120 °C for 15 min. To increase the wetting to the substrate and to control the PEDOT:PSS thickness, 0.2 wt.% Silquest 187 and 30 wt. % IPA are added to PEDOT.

The light absorbing material, a blend of poly(3-hexylthiophene)(P3HT) and 1-(3-methoxycarbonyl)-propyl-1-phenyl[6,6]C61 (PCBM) (1:1 ratio by weight) in chlorobenzene, was spin-coated after filtration onto the PEDOT:PSS layer at 1000 rpm for 30 s, which gave a 105 nm thick layer, and then annealed at 130 °C for 20 min. P3HT and PCBM were purchased from Rieke Metals Ltd and American Dye source, respectively and used as received. After cooling to room temperature, samples were brought to an evaporation chamber from the N_2 glove box. Thermal evaporation of a 1 nm thick LiF layer followed by a 70 nm thick Al layer through a shadow mask (circular shape with 3.5mm diameter) completed the organic solar cell fabrication. Fig. 6-2 shows the schematic diagram of the fabricated organic solar cell structure.
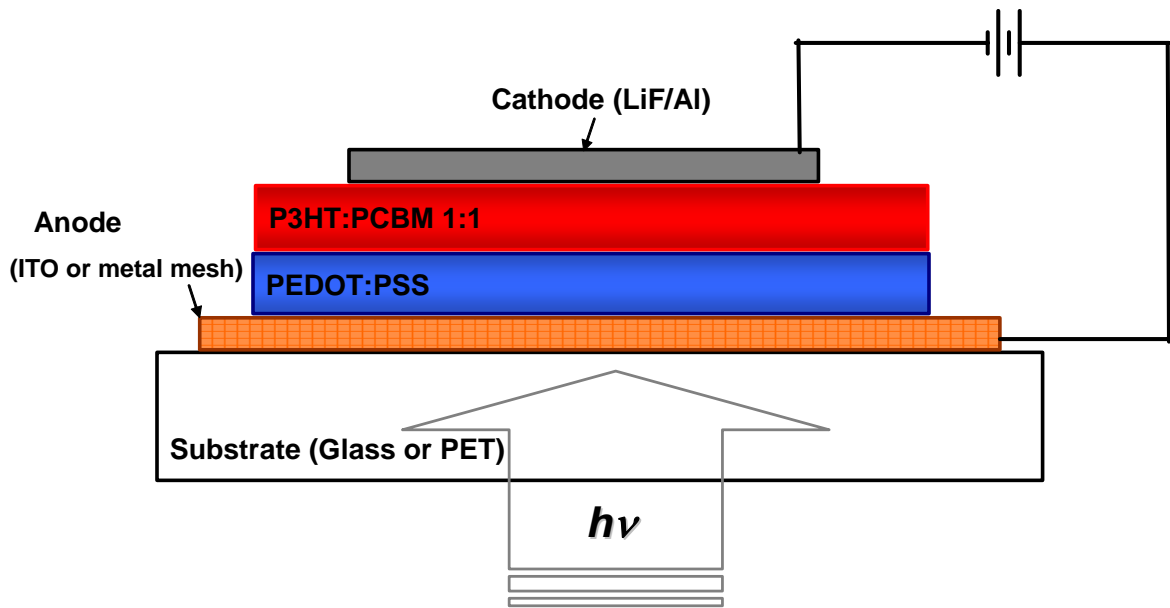
Figure 6-2 Schematic diagram of the fabricated organic solar cell structure.

6.2.2 Fabrication of OSCs on PET substrates

A flexible OSC was also fabricated using transparent Cu mesh electrode

fabricated by metal transfer technique onto PEDOT coated PET substrate (Fig. 6-3) and evaluated compared to the device with conventional ITO electrode. The fabrication process are same as above except that the pure PEDOT:PSS was spin-casted on top of the Cu electrode sitting on PEDOT:PSS coated PET substrate. The shadow mask used in this experiment is circular shape with a diameter of 1 mm.
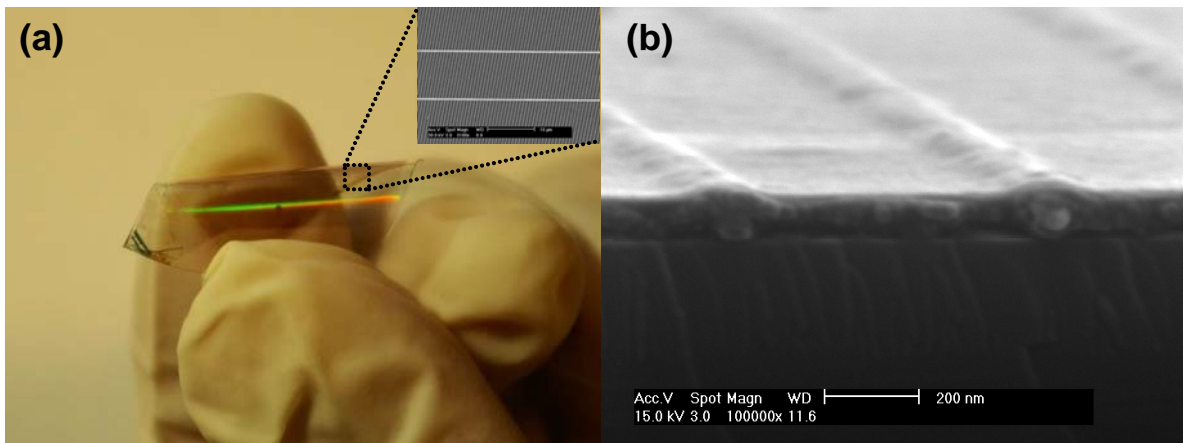
Figure 6-3 (a) Photograph of the transparent Cu electrode on PET substrate used for the fabrication of the flexible organic solar cell. Inset shows the SEM image. (b) SEM image after spin-casting of the PEDOT. For the cross section view, Cu electrode was fabricated on Si substrate.

6.2.2 Measurement of OSCs

The patterned Al cathode has an isolated island type geometry to exclude the overestimation of the photocurrent when a cross-bar type geometry is used.[82, 83] Current versus voltage characteristics were measured in air by illuminating the OSC devices with AM 1.5G simulated sun light (Oriel Solar Simulation, 100 mW/cm^2).

6.3 Results and discussion

The fabricated multi-layer solar cells consist of ITO or nanopatterned metal anode, conducting PEDOT:PSS, P3HT/PCBM blend (1:1 by wt ratio), and LiF and Al cathode from bottom to top. I would like to point out that because the nanopatterned metal electrode has a uniform thickness, we were able to spin coat a very thin PEDOT:PSS layer (~30 nm) on top of it without causing current shunt path which will lower the fill factor and reduce the power efficiency. In case of random nano-wire structures such as the Ag nano-wire mesh[76, 77] used in a previous work, a thin coating of PEDOT layer could increase the current shunt path due to the roughness or unevenness of the random Ag wires. As shown in Figure 6-4, the current versus voltage characteristics of the solar cells having the nanopatterned transparent metal electrodes and ITO electrode on glass substrate are very similar to each other, indicating that such electrodes are interchangeable. All devices showed a power conversion efficiency of ~2 %.
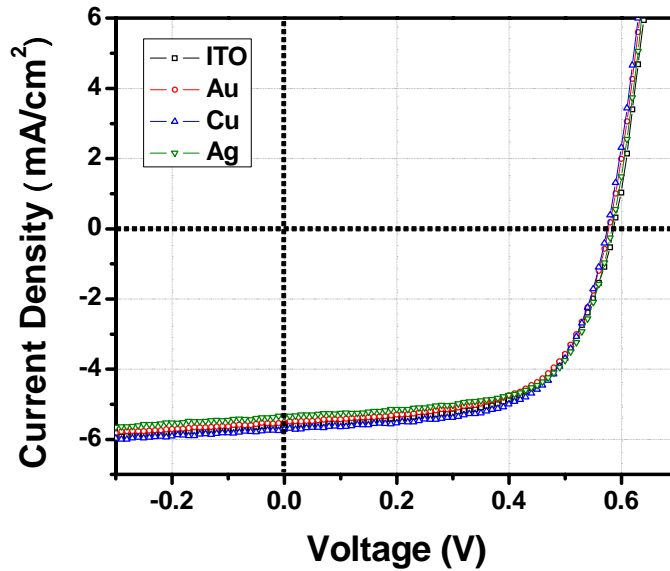
Figure 6-4 Current density versus voltage characteristics of similarly fabricated organic solar cells with varied electrodes, including nanopatterned Au, Cu, and Ag and conventional ITO electrode on glass substrate. (Intensity: AM1.5G 100mW/cm^2)

Detailed device characteristics are summarized in Table 2. Note that such power conversion efficiency is lower than the ones reported in literature because all of our devices were fabricated and tested in ambient environment with no special control of oxygen and moisture. PEDOT and the blend material were spincoated and baked in a N$_2$ glove box, and then the samples were exposed to air before loading to thermal evaporation chamber to deposit the cathode.

Table 6-1 Device characteristics of the solar cells having the nanopatterned Au, Cu, Ag, and ITO electrode on glass substrate.(Intensity: AM1.5G 100mW/cm^2)

Transparent Electrode	Jsc (mA/cm^2)	Voc (V)	FF	Efficiency (%)
ITO	5.59	0.59	0.61	2.00
Au	5.50	0.57	0.62	1.96
Cu	5.71	0.57	0.63	2.06
Ag	5.34	0.58	0.65	2.00

Although the nanopatterned metal electrodes are 8-18% less transparent than that of ITO in the absorption band of P3HT:PCBM around 500 nm, very similar photocurrents were generated under the same intensity light illumination. We believe that light trapping effects induced by the grating structure[78-81] in the high transparency metal electrodes compensates for the effect of lowered transmittance, resulting in similar absorption by the P3HT/PCBM blend layer. Interestingly, the device using Cu electrode showed slightly increased photocurrent and power conversion efficiency of 2.06 % as compared to those of Au and ITO electrodes. From Fig. 2-9(c), the transmittance of the Cu electrode is similar to that of the Au electrode, which in principle should produce same photocurrent. The one difference between the Au and the Cu electrode device is the interface to PEDOT:PSS. We believe that the interface between Cu and PEDOT:PSS is more efficient for hole collection than that between Au and PEDOT:PSS due to the following reason. To collect the photo-generated holes, an anode with lower work function than that of PEDOT:PSS is preferred. The fact that Au has a work function of about 5.22 eV, which is similar to but slightly higher than that of PEDOT:PSS likely impede the hole transfer

from PEDOT:PSS to the Au electrode. On the other hand, Cu has a lower work function (~4.65 eV) than Au, which can facilitate the hole collection. The effect of the reduced internal electric field on photocurrent [84] when low work function is used is negligible in the device with transparent metal electrode because metal electrode occupies only 13 % of whole area on the anode side. Therefore we expect improved performance through efficient hole collection by using metals with lower work function than that of PEDOT:PSS. This may also explain why the performance of the device made with Ag electrode that has a lower transmittance than the other transparent electrodes is comparable to that of the other devices. The difference in transmittance between different metal electrodes could be another contributing factor.

Fig. 6-5 shows the current versus voltage characteristics of the solar cells having the nanopatterned transparent Cu electrode and ITO electrode on PET substrate.
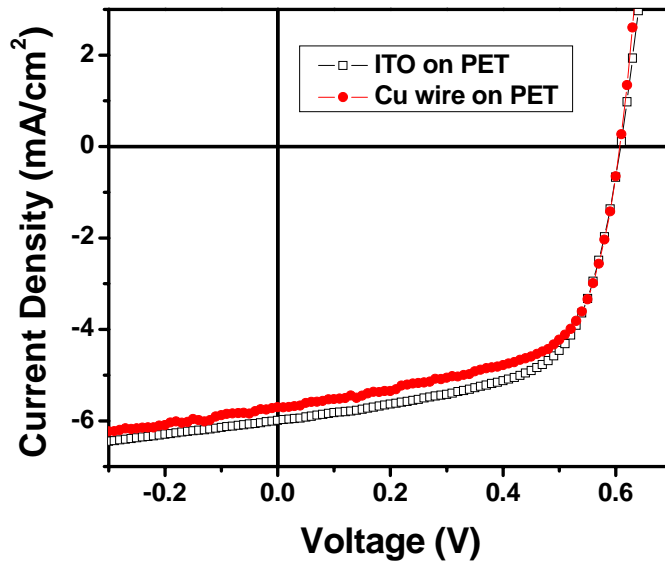
Figure 6-5 Current density versus voltage characteristics of fabricated organic solar cells with nanopatterned Cu and conventional ITO electrode on PET substrate. (Intensity: AM1.5G 100mW/cm^2)

As shown in Fig. 6-5, J-V characteristics of the flexible solar cells having the transparent Cu and ITO electrode are very similar to each other, indicating that such electrodes are also interchangeable for flexible applications. However, the Cu electrode is much more promising due to its superior mechanical stability in bent condition as seen from Chap. 3. The PCE of the device with Cu electrode, about 2.1 %, is comparable to that of the device with ITO electrode, 2.24 %. Both devices have similar open circuit voltage (Voc) and FF which are 0.6 V and 62 %, respectively. The short circuit current (Jsc) is 5.7 mA/cm^2 and 5.9mA/cm^2 for the device with Cu and ITO electrode, respectively. The slight lower Jsc of the Cu device is believed from lower transmittance (Fig. 3-9) at the light absorption range than ITO electrode. However, the difference of the Jsc is smaller than that of transmittance of each electrode, which means that there are also the effects of the light trapping effect in grating structure and the enhanced hole collection efficiency discussed above. The efficiency of the device on PET substrate is a little greater than that of the device on glass substrate. This variation in device performance is believed from the fabrication environment change. Different from the device on glass substrate, the flexible devices were fabricated inside the N$_2$ purged glove box until they were measured in air.

Even though the hole collection efficiency can be increased by using metals with low work function, but since the metal nanograting only covers a small fraction of the anode region, photo-generated holes have to transport through the continuous PEDOT:PSS layer to the metal-wire electrode to be measured as shown in the schematic of Fig. 6-6. Therefore, it is important to evaluate if the conductive PEDOT:PSS can deliver the holes efficiently to the metal electrode. This can be quantified by estimating the voltage drop occurred when holes in the halfway of the two grating lines are collected to metal

electrode. This maximum voltage drop can be expressed as

$$\Delta V_m = J_{ph} \cdot R_{sh} \cdot L^2 = J_{ph} \cdot L^2 \cdot \frac{\rho}{t}(V)$$

where Jph is the photogenerated current density, L is the maximum distance that holes travel (350 nm), ρ is the resistivity of the PEDOT:PSS, and t is the thickness of the PEDOT:PSS. By using the sheet resistance of 150K Ω/□ for a 100-nm thick PEDOT:PSS and the maximum distance that holes have to travel, 350 nm, we estimated that the voltage drop is only the order of μV for each period even if we consider a high efficiency device delivering a photocurrent of 10 mA/cm^2. Therefore, we can conclude that transparent metal-wire electrodes can be treated effectively as a uniform film for the purpose of photocurrent collection.
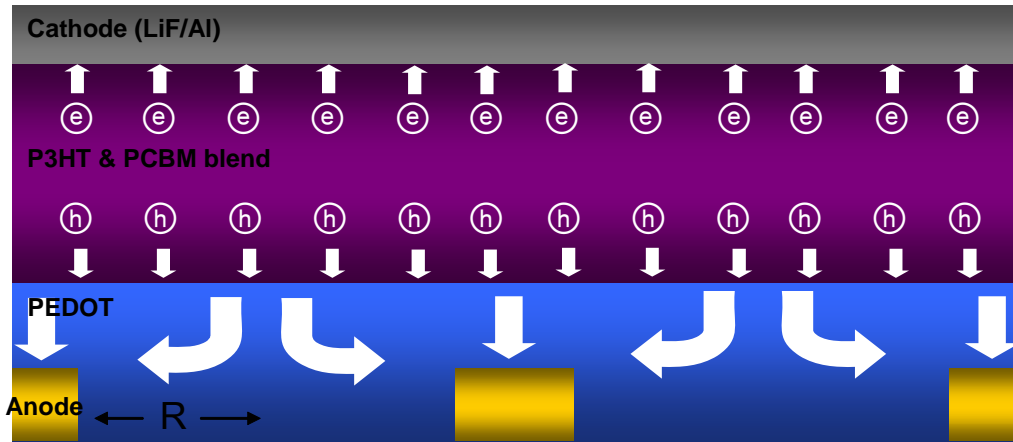
$$\Delta V = \int J_{ph} \cdot R_{sq} \cdot L \ dL$$

Figure 6-6 Schematic of the collection of carriers in the device using nanopatterned transparent electrode.

From the above consideration, we can conclude that transparent metal-wire electrodes can be treated effectively as a uniform film for the purpose of photocurrent

collection. Based on this analysis, a simple design rule that correlates the optimum period of the nanopatterned metal electrodes with the sheet resistance of the PEDOT:PSS was derived, and is shown in Figure 6-7. If we assume a device area of appoximately 0.1 cm^2 and allow a voltage drop of 10 mV in the overall PEDOT:PSS area, the appropriate grating period of the nanopatterned metal electrode at a certain sheet resistance of PEDOT:PSS can be found in the shaded area. The darker the region in the shaded area, the better the OSC performance will be. Here the only assumption made is that the optical transmittance of the metal electrode needs to be comparable to that of the ITO electrode. This means that the line-width of the grating is about 10 % of the period. The star in the shaded region indicates the parameters used in this work. Outside the shaded area the transparent metal electrode will still be able to collect generated photocurrent but with reduced efficiency due to the increased voltage drop in the PEDOT:PSS layer. As a proof, we also fabricated devices with imprinted transparent Au electrode having a period of 10μm. The short circuit current of the device was 80% of the ITO control device leading to 20% lower power conversion efficiency. This result corroborated well with Fig. 6-7, as 10μm periods is outside the shaded region.
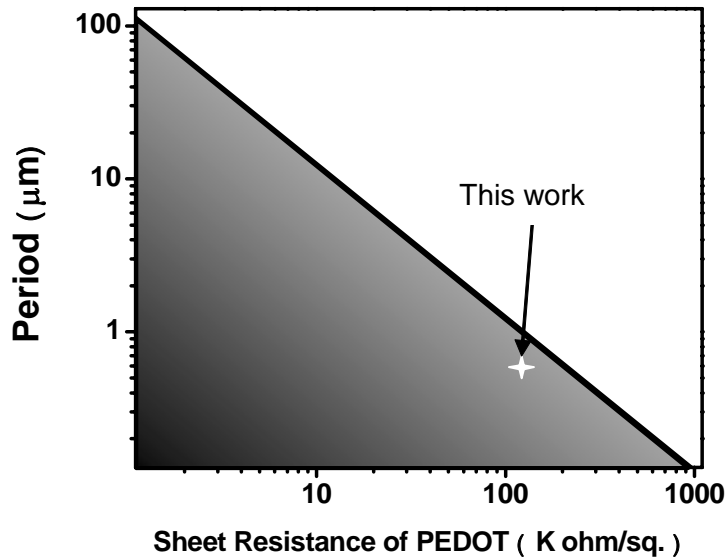
Figure 6-7 Calculated appropriate period of the nanopatterned metal grating in transparent metal electrode as a function of the sheet resistance of PEDOT:PSS. Choosing the metal grating period and the PEDOT sheet resistance within the shaded region will lead to negligible loss of photocurrent. The star in the shaded region indicates the parameters corresponding to this work.

6.4 Summary

Organic solar cells made with the nanopatterned metal electrodes having optimum geometry showed essentially the same performance as the device made with high quality ITO electrodes. The effect of the work function of the nanopatterned electrode on the device performance was also analyzed. It was found that metal electrode with a lower work function than that of the PEDOT:PSS could facilitate the charge transfer from the PEDOT:PSS to the metal electrode, leading to increased FF and higher power efficiency. Large opening area in the transparent metal electrode has little effect on the carrier collection efficiency by using conductive PEDOT layer, which indicates that

nanopatterned transparent metal electrode can be treated as a uniform film. We also demonstrated the flexible devices with transparent Cu electrode, which exhibits same performance as the device with ITO electrode. Cu electrode on a flexible substrate was fabricated by the simple metal transfer printing that can be readily extended to the roll-to-roll processing for low-cost and high throughput fabrication. Therefore the use of very inexpensive Cu material as a transparent electrode and the possible roll-to-roll fabrication could help to realize low cost, large area organic solar cells.

Chapter 7

Surface Plasmon Enhanced Absorption and Efficiency of Organic Solar Cells (OSCs)

7.1 Introduction

Organic solar cells (OSCs) offer a promising alternative to inorganic solar cells due to their low cost, easy fabrication, and compatibility with flexible substrates over a large area. Since the report of a thin film organic solar cell by Tang[40], the power conversion efficiency (PCE) of OSCs has steadily increased and has now reached up to 4-5 %[70, 71, 73, 85]. However, further improvement of the PCE is required for practical applications. To increase the PCE of the device, the light absorption in the organic layer and the electrical carrier transport of the photo-generated carriers must be enhanced[86]. The high absorption of the incident light can be achieved by using a thick organic active layer. However, a thick active layer increases the series resistance and recombination loss mainly due to the low carrier mobility of the organic material resulting in a reduced fill factor(FF) and thus reduced efficiency[87]. On the other hand, thinner organic layers exhibit better electrical carrier transport of the photo-generated carriers. Therefore, the best way to increase the efficiency of a thin film organic solar cell is to increase the absorption of the organic film without increasing the photoactive layer thickness. For this need, several light trapping approaches such as a V-folded configuration[88], diffraction

grating[78, 79], photonic crystal (PC)[89], and surface plasmon resonance (SPR)[69, 90-96] have been investigated and showed promising results. Among these, the utilization of the SPR in metallic nanostructures (eg. Au, Ag) is one of the most promising approaches as surface plasmons exhibit strongly enhanced electromagnetic fields in the vicinity of the metal by the incident light, which can lead to high absorption in the organic film and higher efficiency. Ag nanoparticles have been widely used to enhance the light absorption in thin film organic solar cells in which they were inserted in normal device structure[90, 93, 94]. Thus, the ITO film is still used as a transparent electrode of the device. However, it would be even more attractive in terms of cost and performance if the transparent electrode itself can create the SPR. Recently, such attempts have been reported using randomly perforated Ag films and periodic Ag gratings[95, 96]. Even though these approaches showed relative enhancement of the absorption by the SPR effect in organic solar cells, none of them were compared with conventional ITO devices, due to overall much lower efficiency obtained by those devices.

In this work, a periodic Ag grating structure is employed not only as a transparent electrode but also as the excitation source of the SPR. The incident light resonantly excites surface plasmon modes between the Ag grating electrode and the thick metal cathode, increasing the field intensity and absorption in the organic thin film. It is shown that the overall efficiency of the device using a Ag grating is greater than that of the device using ITO due to higher absorption by SPR.

7.2 Design structure and preliminary simulation.

Figure 7-1 shows the schematic of the proposed device structure utilizing the

SPR to enhance the light field and thus the absorption (efficiency). It consists of a glass substrate, Ag grating, organic layer, and thick Ag cathode from top to bottom. The incident light is illuminated from the glass side. The preliminary simulation based on Rigorous Coupled Wave Analysis(RCWA) was performed for this device structure at a wavelength of 500 nm with the refractive index of each layer as shown in Fig. 7-1.
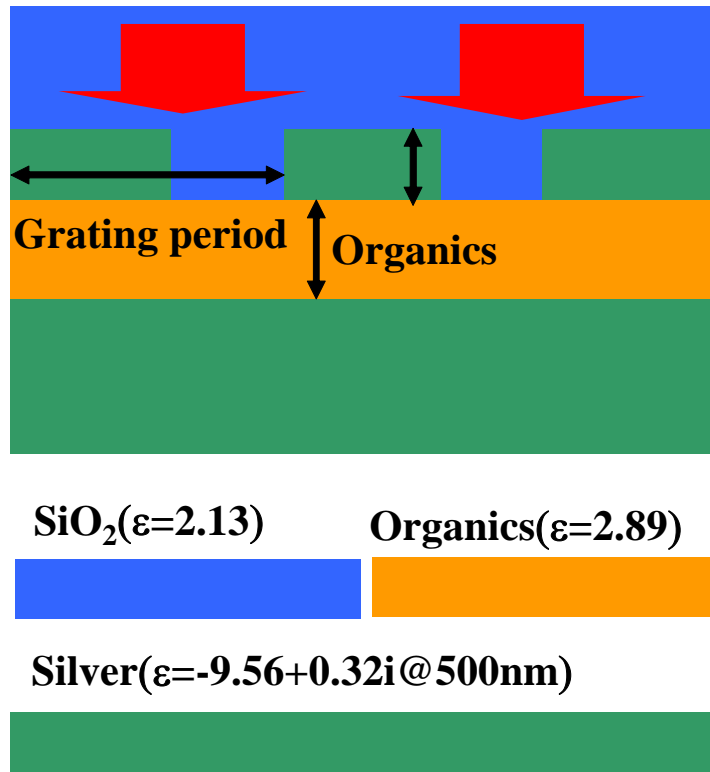
Figure 7-1 Device schematic and refractive index of each layer used in the preliminary simulation.

The period of the Ag grating is fixed at 220 nm and the variable parameters for the simulation are the height and duty cycle of the grating, the thickness of the organic

Simulation was done by one of collaborators, Ting Xu, in Institute of Optoelectronics, the Chinese Academy of Science.

layer, and the incident wavelength.

Figure 7-2 shows the field enhancement factor (a), defined as the light intensity inside the organic layer in the proposed device normalized to the incident one, as a function of the Ag grating height, and the field intensity profiles at different Ag grating heights (b,c). The duty cycle is assumed to be 0.73 (opaque line width: 160 nm). The grating height of 40 nm was shown to give the highest field enhancement factor.
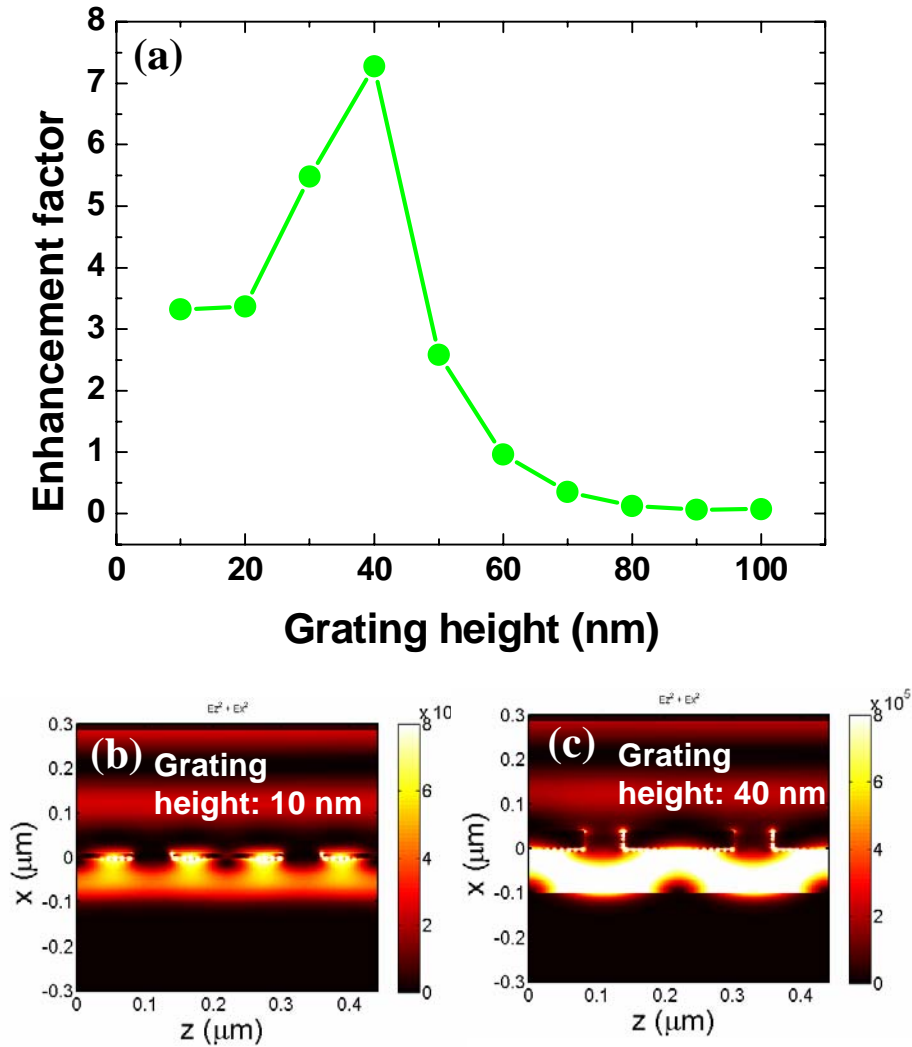
Figure 7-2 (a) Field enhancement factor, normalized to the incident light intensity, as a function of Ag grating height, and (b,c) field intensity profiles at different Ag

grating height (b:10nm, c:40nm). The duty cycle is assumed to be 0.73 (opaque line width: 160 nm).

The effect of the thickness of the organic layer is also examined, as shown in Fig. 7-3, and the thickness of around 90 nm was shown to give the highest field enhancement factor.
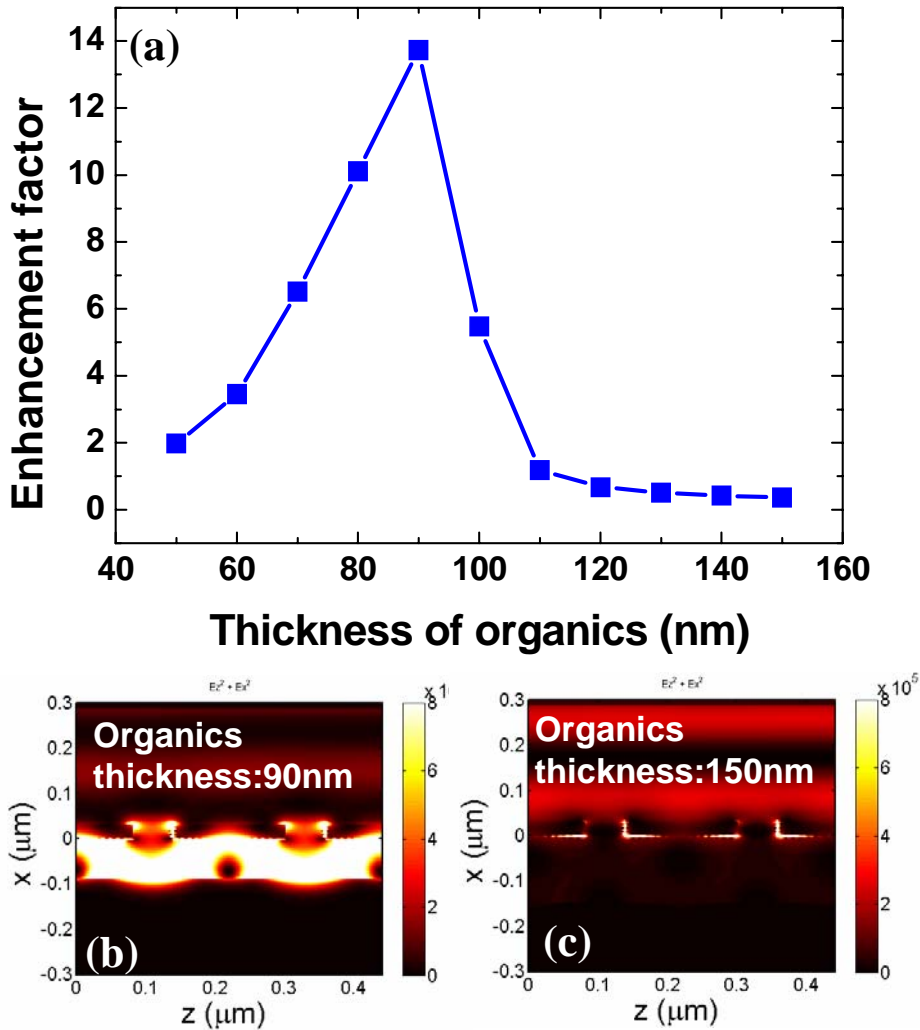
Figure 7-3 (a) Field enhancement factor as a function of Ag grating height, and (b,c) field intensity profile at different organic layer thickness. The duty cycle and the grating height are assumed to be 0.73 (opaque line width: 160 nm), and 30 nm, respectively.

The dependency of the field enhancement factor on the grating duty cycle is shown in Fig. 7-4. The field enhancement factor is highest at a duty cycle of 0.36 (line width of 80 nm), and it drops and saturates as the duty cycle increases.
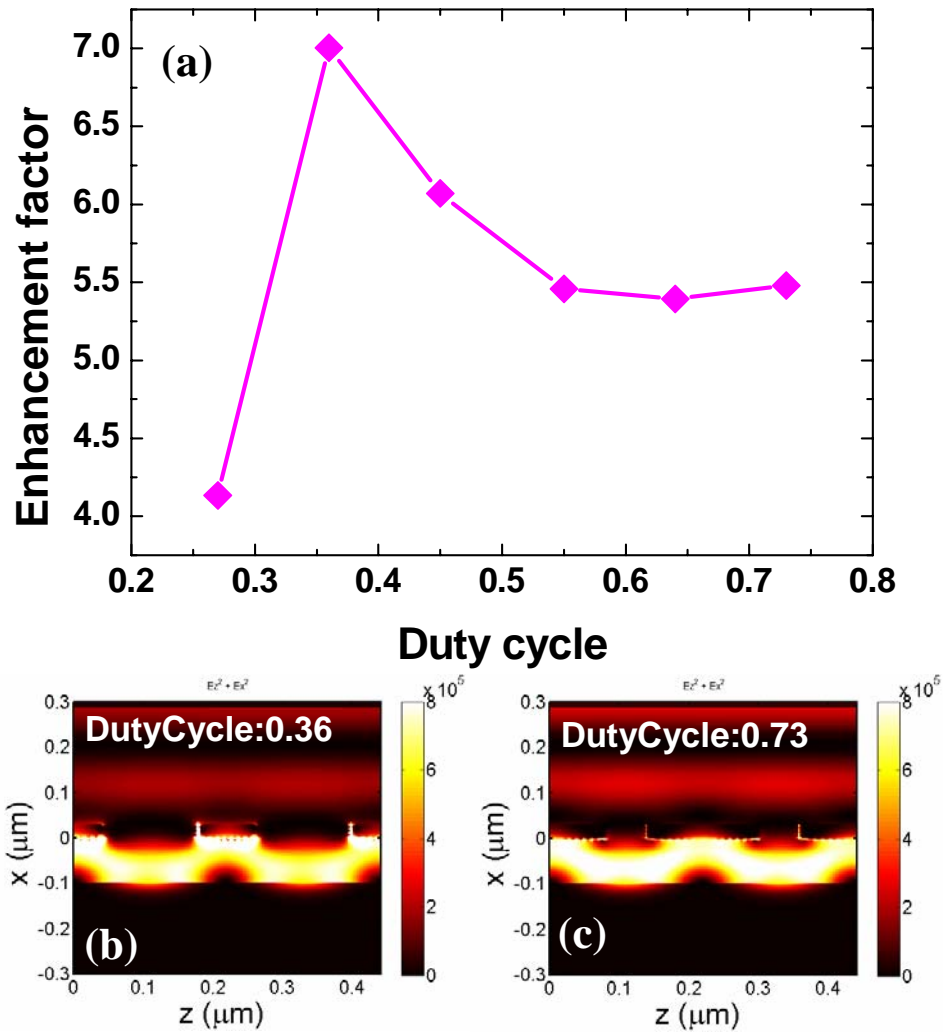
Figure 7-4 (a) Field enhancement factor as a function of Ag grating duty cycle, and (b,c) field intensity profile at different duty cycle. The thickness of organic layer and grating height are assumed to 100 nm, and 30 nm, respectively.

Figure 7-5 shows the wavelength dependency of the field enhancement factor. For this simulation, the refractive index of Ag was varied and that of organic layer was assumed to be unchanging.
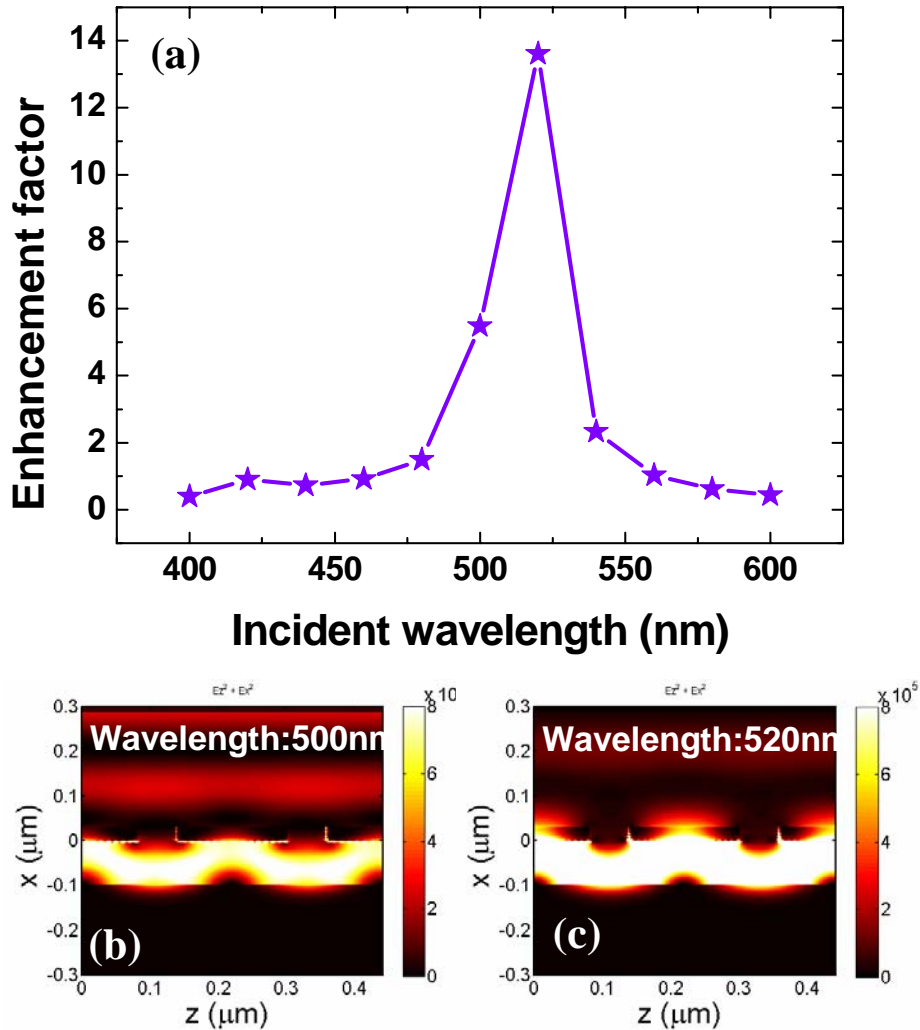
Figure 7-5 (a) Field enhancement factor as a function of the incident light wavelength, and (b,c) field intensity profiles at different wavelengths. The thickness of the organic layer, the grating height, and the duty cycle are assumed to be 100 nm, 30 nm, and 0.73 respectively.

The bandwidth for which the field enhancement factor is greater than 1 is 100 nm

with a peak enhancement factor at a wavelength of 520 nm.

Based on the preliminary simulation results the optimal structure parameters are as follows:

- Grating period: 220 nm

- Duty cycle: 0.36 ~ 0.73

- Grating height: 30 ~ 40 nm

- Thickness of organic layer: 80 ~ 100 nm

Preliminary simulations confirm the presence of the surface plasmon-enhanced light intensity, which will lead to enhanced absorption in the organic active layer and thus greater power conversion efficiency of the organic solar cell.

7.3 Experimental details

7.3.1 Fabrication of the mold and Ag electrode

With the preliminary simulation results as a starting point, an attempt was made to fabricate organic solar cells using the Ag grating as an anode. The mold with proper geometry was the first prepared for this work. Figure 7-6 (b) shows the SEM image of the mold used in this work. This mold was fabricated from the original mold, which has a line-width of about 150nm and a trench of about 70 nm. This mold was fabricated using laser interference lithography[97]. NIL is performed using the original mold on the imprint resist, MRI8030, coated on 10 nm thick Cr layer on a SiO_2 substrate. After NIL, thin metals are shadow-evaporated on each side wall of the MRI pattern. O_2 RIE, Cr dry etching, SiO2 dry etching, and removal of Cr layer complete the fabrication of the mold, which has the period of 220 nm, the line-width of ~110 nm and the duty cycle of about

0.5. Specific fabrication conditions can be found in Chap. 2.
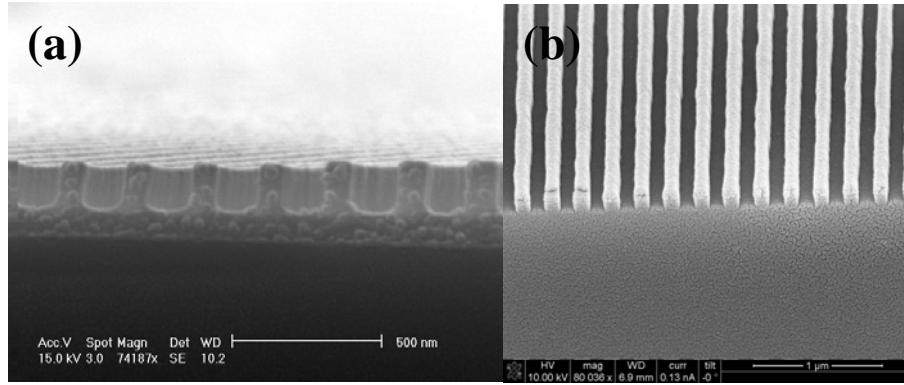
Figure 7-6 SEM images of (a) imprinted MRI pattern using mother mold (opposite shape) and (b) a mold with a duty cycle of 0.5 fabricated from (a).

Ag gratings with different line-widths on glass substrates are fabricated with conventional NIL using the mold shown in Fig. 7-6(b). After NIL, Ti of 5 nm and 25 nm was deposited on each sidewall of the imprinted grating structure to fabricate Ag gratings with a line width of 100 nm and 60 nm, respectively. O_2 RIE, deposition of 40 nm thick Ag with 1 nm NiCr using electron beam evaporation and lift-off complete the fabrication of the Ag grating electrode on a glass substrate. The optical transmittance of these Ag gratings is shown compared to a conventional ITO electrode in Figure 7-7. The measured transmittance was referenced to air. The average transmittance in the visible range of Ag gratings with a line width of 100 nm, 60 nm, and ITO electrode is 58 %, 77 %, and 87 %, respectively. Ag gratings with 100 nm and 60 nm line-widths will be referred to as AgW and AgN, respectively. The Ag grating samples have a dip in the transmittance at around 420 nm due to the absorption increase by the surface plasmon resonance.
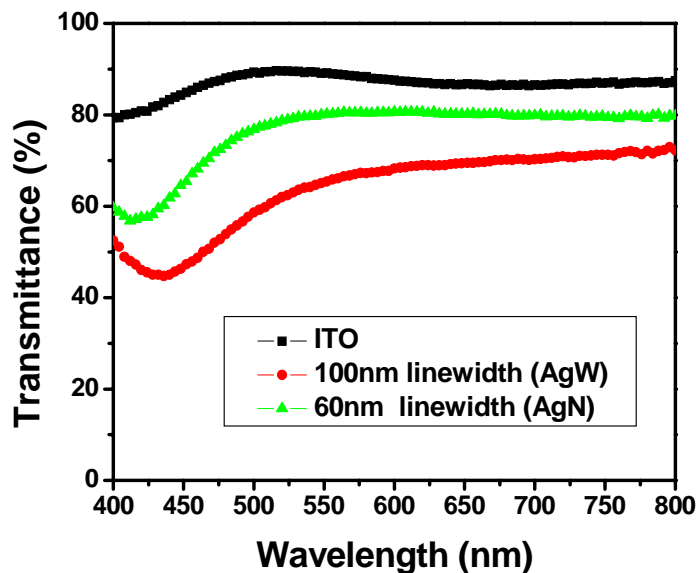
Figure 7-7 Optical transmittance of the Ag gratings and conventional ITO electrode

7.3.2 Fabrication of OSCs

To prove the concept, organic planar heterojunction solar cells using copper phthalocyanine (CuPc) and buckminsterfullerene (C60) were fabricated. First, the Ag grating electrodes and ITO on glass were cleaned in acetone and isopropyl alcohol (IPA) under sonication for 30 min each. ITO coated glass had an additional 5 min UV ozone cleaning. Filtered PEDOT:PSS solution was spin-coated onto the Ag grating electrodes and ITO at 1000 rpm for 30 s, producing a 30 nm thick layer, and then baked at 120 °C for 15 min inside a homemade N_2 purged box. To increase the wetting on the substrate and to control the PEDOT:PSS thickness, 0.2 wt.% Silquest 187 and 100 wt. % deionized water were added to the PEDOT (Baytron PH 500). Samples were then brought to an evaporation chamber from the N_2 box. Thermal evaporation of the CuPc, C60, BCP, and Ag completed the organic solar cell fabrication. A shadow mask (diameter of 1 mm) was

put on the sample before the Ag evaporation. Fig. 7-8 shows the schematic of the fabricated device.
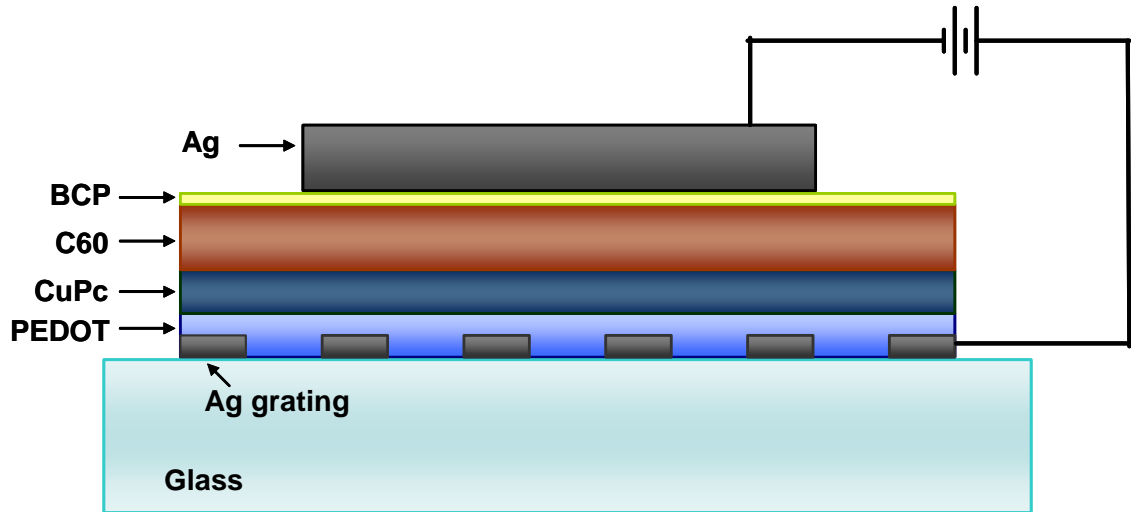
Figure 7-8 Schematic of the fabricated small molecule organic solar cell

Several devices with different organic layer thicknesses, as shown in Table 7-1, were fabricated to investigate the dependence of the field enhancement on the organic layer thickness.

Table 7-1 Thicknesses of the organics layers of the fabricated organic solar cell

Device #	Thickness (nm)				
	PEDOT	CuPc	C60	BCP	Total
1	30	28	44	8	110
2	30	25	35	8	100
3	30	20	32	8	90
4	30	16	26	8	80
5	30	12	20	8	70

A 40 nm thick Ag grating and ITO electrode were used as an anode and a 70 nm thick bare Ag film was used as a cathode for all of the fabricated devices. The thickness of PEDOT and BCP was fixed at 30 nm and 8 nm, respectively. These layers are very important for preventing device shortening and blocking generated excitons, respectively. The total organic layer thickness was controlled by changing the thickness of the CuPc and C60, as shown in table 7-1, while attempting to keep the ration the same.

7.4 Results and discussion

The current density vs. voltage characteristic was measured by illuminating the devices with AM 1.5G simulated sun light (Oriel Solar Simulation, 100 mW/cm^2). The open-circuit voltage (Voc) and the fill-factor (FF) are similar for both the ITO and Ag devices except device #5. The Voc of the ITO device, ~0.53 V, is slightly greater than that of Ag devices, ~0.5 V, and the FF of about 50 % is similar for both devices. These results indicate that the patterned Ag grating did not affect the device fabrication using thermal evaporation of the small molecule materials and photo-generated carrier collection. The Ag device # 5 having the thinnest organic layer (70 nm) showed much reduced Voc, ~0.37 V, which is believed to be caused by the shortening path between the edge of the grating and top cathode due to the very thin organic layer. However, the short-circuit current (Jsc) showed a dramatic difference. Because the SPR enhances the light field, we expect the enhanced absorption efficiency accordingly which will lead to the increased Jsc. For thick organic layers (device #1 and #2), the Jsc of the device made with a 60 nm Ag grating (AgN device) is comparable to that of the ITO device. For organic layers

thinner than 100 nm (device #3, #4, and #5), the Jsc of the AgN device was enhanced as much as 43 % compared to that of ITO device as the thickness of the total organic layer decreases to 70 nm. The device made with a 100 nm line-width Ag grating (AgW device) also showed a similar behavior to AgN device but the overall enhancement was lower due to the low transmittance of the Ag grating in this case. Fig. 7-9(a) shows the dependency of the Jsc of each device (ITO, AgN, AgW device) on the thickness of the organic layer. Fig. 7-9(b) shows the current density vs. voltage curve of the device #4 which exhibits the highest enhancement of the Jsc and the overall PCE. In fact, the device #5 showed the highest enhancement of the Jsc but the PCE is low due to the low Voc.
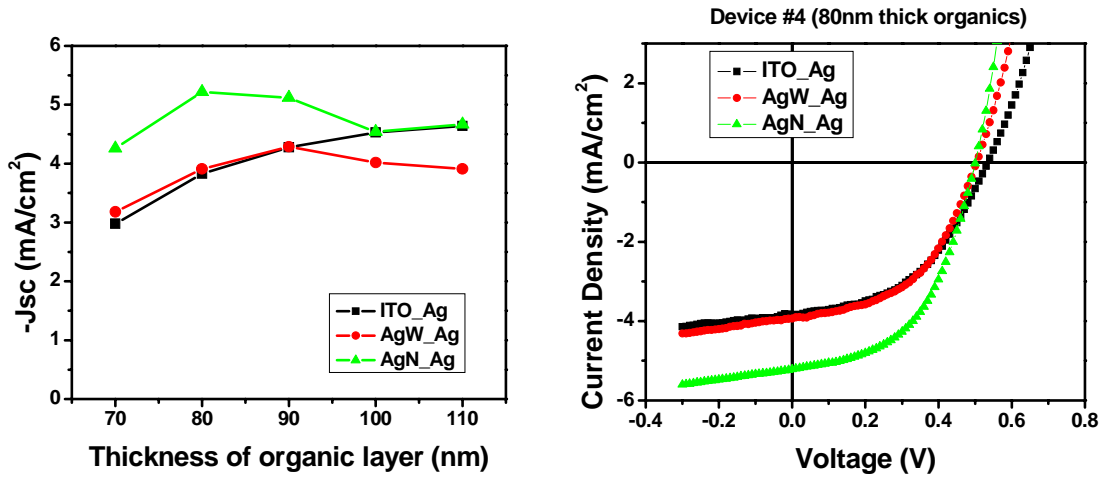
Figure 7-9 (a) Jsc vs. thickness of the organic layer characteristics of the devices fabricated (ITO, AgN, AgW device) (b)current density vs. voltage curve of the device #4 which exhibits highest enhancement of the Jsc and overall PCE.

As shown in Fig. 7-9(a), the Jsc of the ITO device decreases as the organic layer thickness decreases due to the corresponding lower absorption. However, the Ag device showed enhanced Jsc as the organic layer thickness decreases mainly due to enhanced

light intensity by the SPR and thus enhanced absorption in thinner devices. The other possibilities for the enhanced absorption and Jsc are discussed later. Each device has a different thickness of the organic layer resulting in different absorption efficiency. The enhancement factor of the Jsc of the Ag device due to surface plasmons was extracted by normalizing the Jsc of the Ag device with the Jsc of the ITO device. Therefore, this enhancement factor can be used as a measure of the enhanced absorption and internal optical field by the SPR. Fig. 7-10 shows the Jsc enhancement factor vs. the thickness of the organic layer.
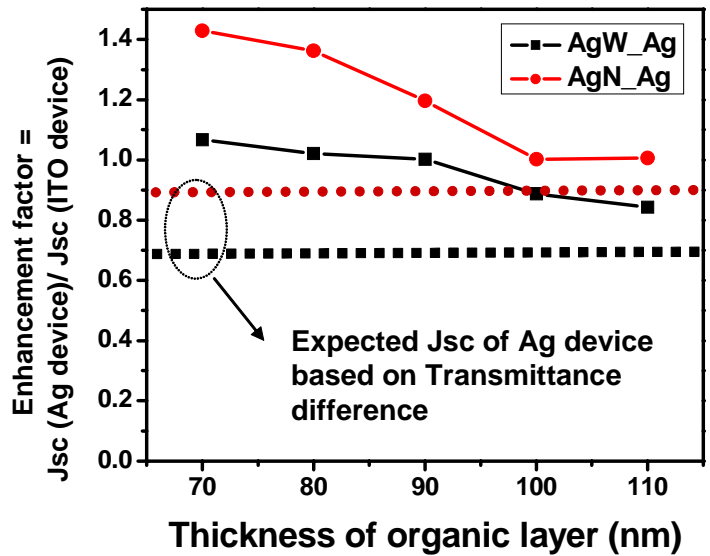
Figure 7-10 Enhancement factor vs. the thickness of the organic layer curve. Dotted lines show the expected Jsc of the Ag device based on the transmittance of each electrode without absorption enhancement by the surface plasmon.

One should note that the enhancement factor shown in Fig. 7-10 did not take into account the transmittance of each Ag grating electrode. In fact, the transmittance of the

Ag grating electrodes is lower than that of the ITO electrode as shown in Fig. 7-7. Therefore, the enhancement factor is even higher than those shown in Fig. 7-10 when the transmittance of each electrode is considered. For simplicity, if we consider the average transmittance of each electrode in the visible range, the net enhancement factor due to surface plasmons can be extracted from the difference between solid and dotted line. The dotted line shows the expected Jsc when there is no surface plasmon enhanced absorption. This net enhancement factor due to surface plasmons for the Ag devices is shown in Fig. 7-11. As shown, surface plasmons will enhance the Jsc of the AgN device as much as ~65 % compared to the ITO device when both the AgN and ITO device receive the same amount of the light from the incident one.
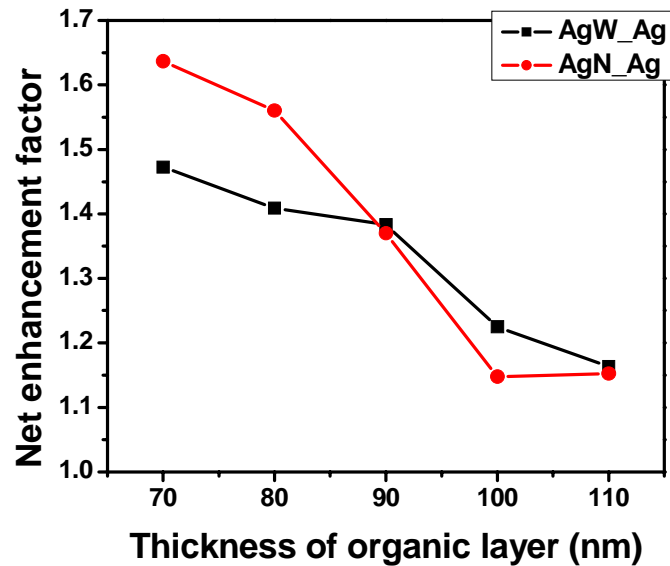
Figure 7-11 Net enhancement factor of the Jsc of the Ag devices compared to ITO device when both devices receives the same amount of the incident light.

Due to the enhanced Jsc, the overall PCE of the AgN device was also enhanced

compared to that of the ITO device. For device #3, the PCE of the AgN was enhanced by about 18 %, with the absolute PCE of the AgN device and ITO device of 1.41 % and 1.2 %, respectively. For device #4, the PCE enhancement was even higher, 35 %, with the absolute PCE of the AgN device and ITO device of 1.32 % and 0.97 %, respectively. As discussed earlier, each device has a different organic layers thickness which will lead to different absorption efficiency and Jsc as seen from the behavior of the ITO device. However, Ag devices do not follow those trends. As the organic layer becomes thinner, the effect of the SPR is getting stronger. However, there should be a limitation about the minimum thickness at which the maximum light field enhancement is achieved. Based on the enhancement factor shown in Fig. 7-10, the degree of the increase of the enhancement factor starts to decrease at organic layer thicknesses below 80 nm. Therefore, we can expect the enhancement of absorption efficiency due to surface plasmon resonance might be saturated at organic layer thicknesses a little below 70 nm. In practice, the maximum efficiency enhancement was achieved at an organic layer thickness of 80 nm. Below 80 nm, it showed shorting behavior between the anode Ag grating and the cathode due to the non-planar nature of the Ag grating used in this work. If we can make the grating planar by imbedding the grating inside a glass substrate or other ways, we can expect the PCE enhancement to be higher than the 35 % achieved in device #4 (80 nm thick organic layer). Based on the Fig. 7-11, the effect of the SPR on the enhancement of the Jsc is similar for both Ag grating devices when the average transmittance of each electrode is considered. However, the absolute Jsc and PCE of the device with the 100 nm line-width Ag grating (AgW device) is much lower than the AgN device. This tells us that the transmittance of the anode is also a very important factor for the device with high PCE.

To find a possible reason for the increased absorption and thus the Jsc, incident

photon to current efficiency (IPCE) was measured for each device. The obtained external

quantum efficiency (EQE) of each device is shown in Fig. 7-12.
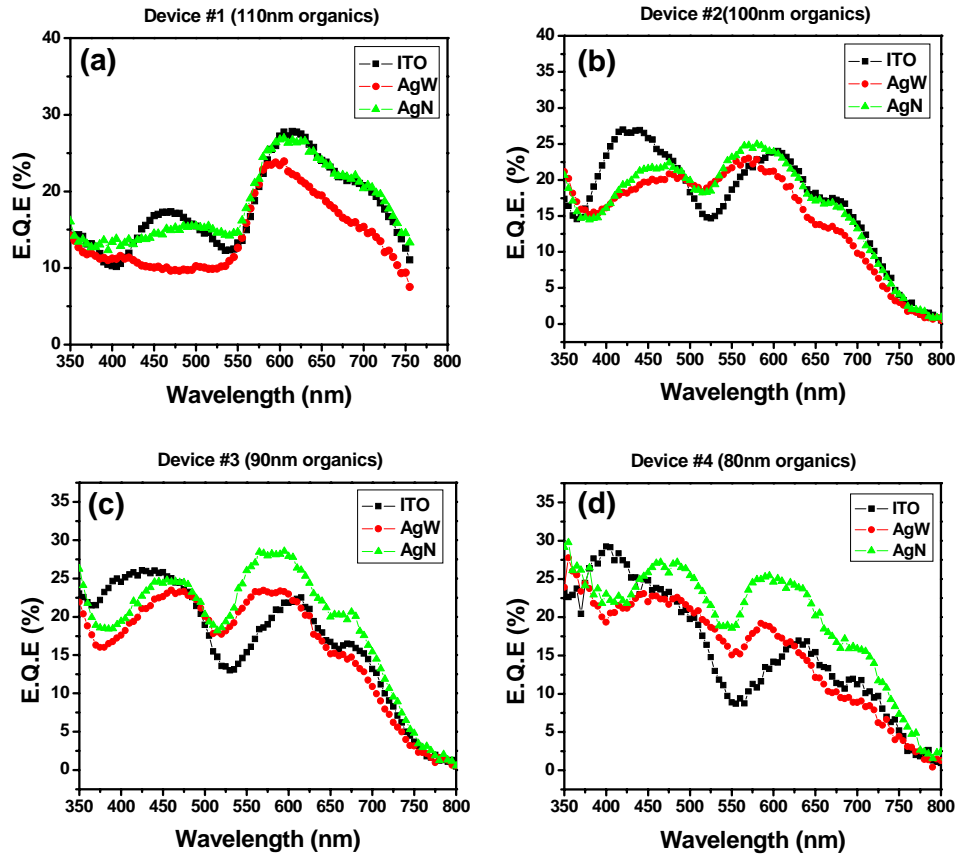
Figure 7-12 EQE spectra of the device. (a) device #1, (b) device #2, (c) device #3, and (d) device #4.

The EQE of device #5 is not shown because of its instability. There are

noticeable differences in the Ag devices as the organic layer gets thinner (Fig. 7-12(a-d)).

The two EQE peaks located at a wavelength of around 470 nm and 570 nm are red and

blue shifted, respectively, compared to those of the ITO, around 420 nm and 620 nm. For

thinner organic layers, both peaks are getting stronger and the bandwidth for which the

EQE of Ag device is bigger than that of ITO device is getting wider, which can explain

the enhancement of the Jsc of each device. Since the EQE depends proportionally on the absorption efficiency, we can attribute the observed enhancement of the Jsc to the enhanced light field caused by the surface plasmon resonance in the Ag grating structure. The enhancement factor of the light intensity and thus absorption efficiency of the Ag device relative to ITO device as a function of wavelength can be deducted from the ratio of the EQE between the Ag devices and the ITO device. Fig. 7-13 shows the EQE enhancement factor of the Ag devices relative to ITO device.
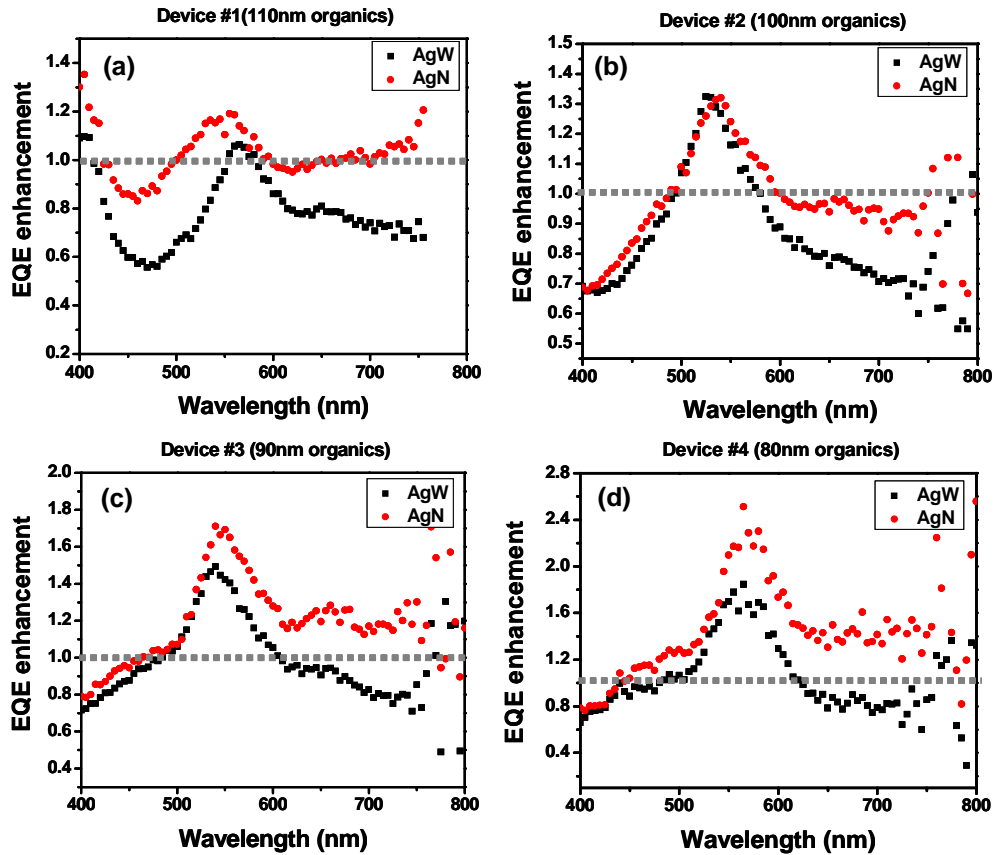
Figure 7-13 EQE enhancement factor of the Ag device as a function of wavelength obtained by normalizing the EQE of the Ag device with the EQE of the ITO device.

As shown in Fig. 7-13, the relative EQE enhancement of the Ag device is increasing and the bandwidth the area with the enhancement greater than 1 is getting

wider as the organic layer gets thinner. Specifically, the maximum enhancement occurs at a wavelength of 555 nm for device #1 (thickest organic layer). For device #2 and #3, the maximum enhancement is at around 540 nm. For device #4 (thinnest organic layer), the maximum enhancement is at around 570 nm. The origin of the variation of the maximum enhancement wavelength is not clear and needs to be further studied. So far, about a 2.5 fold EQE enhancement was achieved at around 570 nm for the organic layer thickness of 80 nm (device #4), which led to the 35 % PCE enhancement. Therefore, we can expect absorption efficiency enhancement by the same amount. Here, we can also extract the net EQE enhancement factor due to the SPR for the Ag devices by taking into account the transmittance of each electrode. This can be obtained by taking the ratio of the EQE of each device which was normalized by the transmittance of each electrode. Fig. 7-14 shows the net enhancement factor due to the SPR for the Ag devices.
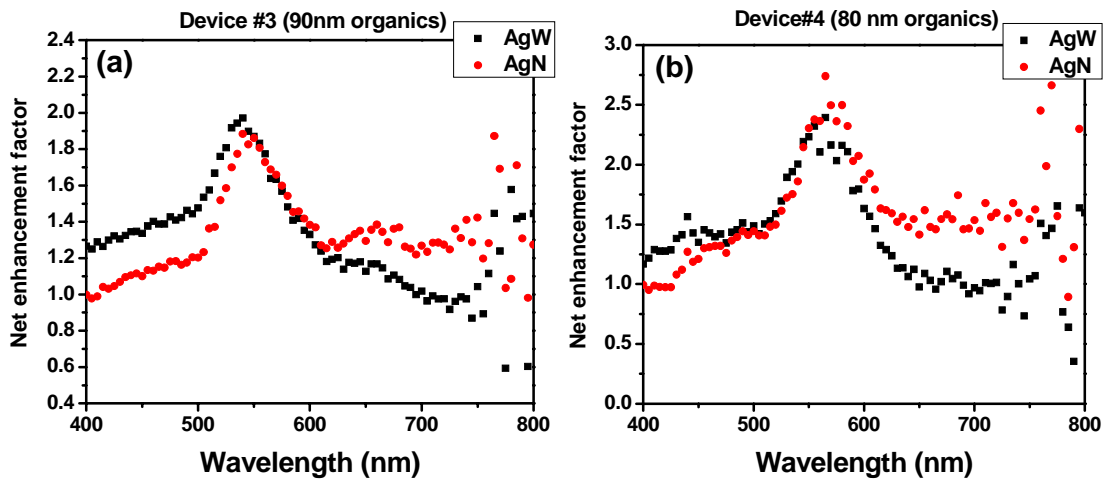
Figure 7-14 Net enhancement factors for the Ag device by the SPR as a function of wavelength when the transmittance of each electrode is considered. (a) Device #3 (90 nm organics layer), and (b) device #4 (80 nm organics layer)

As shown in Fig. 7-14, when the Ag device delivers the same amount of the light to organic layers from the incident one as the ITO device does, the maximum enhancement factor of about 2.8 at a wavelength of 570 nm can be achieved in case of device #4 (80 nm organics layer). Moreover, the SPR enhanced the EQE over the entire visible wavelength. The degree of enhancement is similar for both Ag devices; however, the resulting PCE enhancement of the AgW device is very small because of the low transmittance. Therefore, a Ag grating with high transmittance (narrow line-width) is desirable for the enhancement of the PCE due to the surface plasmon resonance.

So far, we here attributed the enhancement of the Jsc and overall PCE to the enhancement of the absorption efficiency due to the SPR. Are there other effects which can explain the observed enhancement of Jsc? There are two possibilities: light trapping by the light diffraction in grating structure and the device area increase caused by using 40 nm thick Ag grating as an anode. There are some reports that light diffraction from the grating pattern can increase the optical path length of the light resulting in higher absorption efficiency[78, 79]. However, the period of the Ag grating used in this work, 220 nm, does not create diffraction in the visible range where the organic layers absorb. Simulations showed that diffraction occurred at a wavelength below 315 nm when a 220 nm period grating and the refractive index of 2 for the organic layers were used. Therefore, we can exclude the possibility of light trapping by diffraction. Fig. 7-15 shows SEM images of the fabricated Ag grating device. As shown in Fig. 7-15, the device has a sinusoidal shape following the Ag grating dimensions.
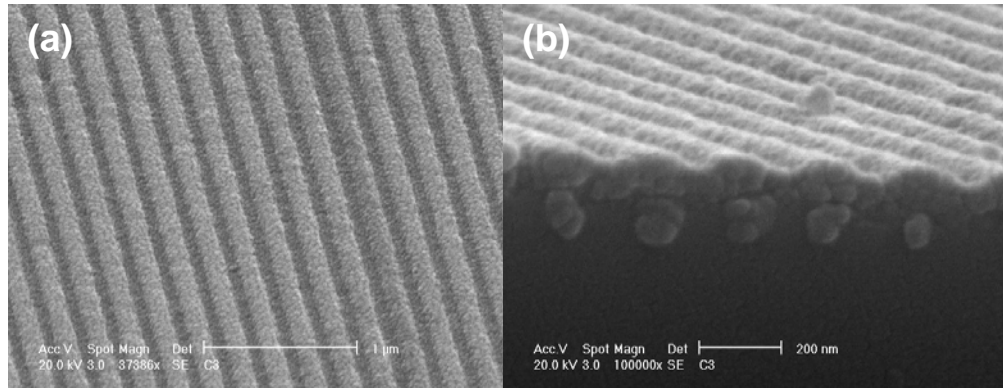
Figure 7-15 SEM images of device with Ag grating. (a) top view, and (b) side view.

Even though the device shows the sinusoidal shape, the increase of the device area is negligible compared to the enhancement of the Jsc. The difference between the peak and the valley is about 35 nm which was estimated to increase the surface area by about 5 %. Therefore, we can also exclude the possibility of device area increase for the observed enhancement of the Jsc. This conclusion is backed by another experiment, which investigated the effect of the grating thickness on the device performance. As shown in Fig. 7-16, there is no change in the Jsc as the thickness of the grating changes. These facts confirm that the observed Jsc of the Ag grating device was enhanced through the concentrated light field due to the surface plasmon resonance in the structure.

Ag grating thickness dependency
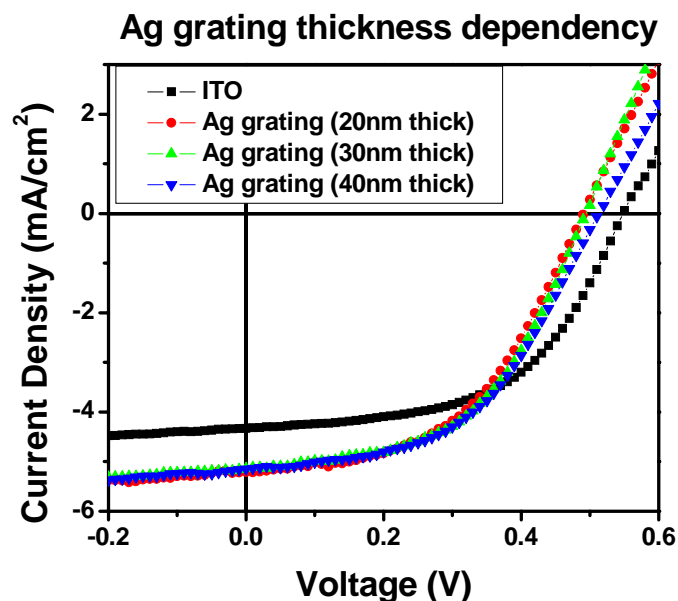
Figure 7-16 Current density vs. voltage curve of the ITO device and Ag device with Ag grating height of 20, 30, and 40 nm. The total organic layer thickness is 90 nm (device #3)

Simulations were performed again to draw the internal field enhanced by surface plasmon resonance. At this moment, the simulations used the measured complex refractive index data for each organic layer. Fig. 7-17 shows the field profile inside the structure at different wavelengths for the device #4 (organic layer thickness of 80 nm). From the Fig. 7-13, at a wavelength of around 420 nm, the AgN device shows an EQE enhancement factor lower than 1 (ITO shows better EQE). The EQE of the AgN device showed the strongest enhancement at a wavelength of around 560 nm and moderate enhancement at a wavelength of around 620 nm.
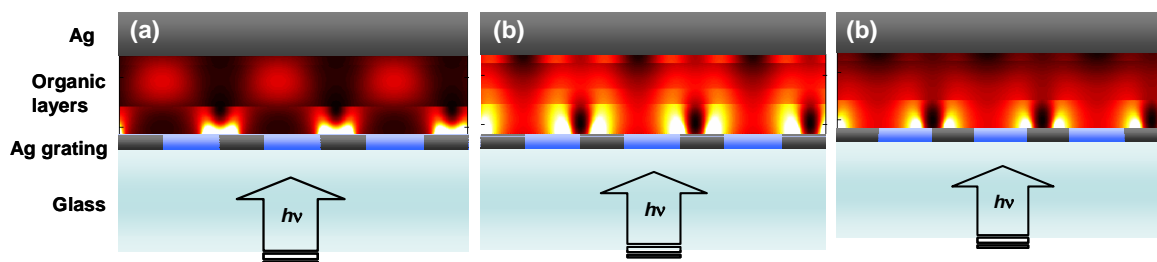
Figure 7-17 Simulated internal field inside the Ag device at a wavelength of (a) 420 nm, (b) 560 nm, and (c) 620 nm.

As shown in Fig. 7-17, strong enhancement of the optical field within the organic layer is seen at a wavelength of around 560 nm, which matches with the experimental results. In fact, the simulation predicts that the strongest enhancement is at about 520 nm. It is believed that this discrepancy is from the difference between the simulated device (Fig.7-8) and the fabricated device (Fig. 7-15). More simulations which can match with the experimental results are needed.

7.5 Summary

In summary, we demonstrated organic solar cells with a periodic Ag grating and evaluated their performance compared to the one with conventional ITO electrode. The periodic Ag grating acts not only as a transparent electrode but also as an excitation source of the SPR. Incident light resonantly excites surface plasmon modes between the Ag grating electrode and the thick metal cathode, increasing the field intensity and absorption in organic thin film. The Surface plasmon effect was sensitive to the organic layer thickness sandwiched between the cathode and Ag grating anode. As the organic layer gets thinner, the surface plasmon effect was shown to be stronger and the Jsc was enhanced as much as 45 % compared to that of the ITO device. The measured EQE was

also enhanced for thinner organic layers. A 2.5 fold enhancement of the EQE of the Ag device relative to the ITO device was achieved at a wavelength of around 570 nm for an 80 nm thick organic layer. Due to this enhancement, the overall power conversion efficiency of the Ag device was enhanced by about 35 % compared to that of the ITO device. Further improvement of the PCE can be achieved by using a thinner organic layer at which the surface plasmon effect is strongest. However, device structure optimization to reduce the chance of shorting between the cathode and anode is needed. Simulations predict the presence of the surface plasmon effect, but more optimization needs to be done to match more exactly with the experimental results.

Chapter 8

Conclusion

8.1 Summary of thesis

We have developed and demonstrated a new type of transparent and conductive electrode (TCE) based on a periodically nanopatterned metal film. A TCE is a very important component in any photosensitive optoelectronic devices such as organic light emitting diodes (OLEDs) and organic solar cells (OSCs). An ideal TCE must be highly transparent to allow the maximum amount of light through, and it must also be conductive to provide uniform electrical current distribution. The most widely used material in industry and academia is tin-dope indium oxide, commonly referred as ITO. Even though ITO has demonstrated good performance as a TCE for optoelectronic applications, it may not be the best choice for future low-cost and high performance optoelectronic applications in terms of the cost, chemical and mechanical properties of the material. The developed nanopatterned transparent metal electrodes have the characteristics of high optical transmittance and electrical conductivity, but unlike ITO, those properties are controlled independently. Moreover, it has been demonstrated that our transparent metal electrode is mechanically more stable than the ITO electrode in flexible applications. The work function of the TCE can be easily controlled by choosing different metals. Other than the high transmittance and conductivity, transparent metal

105

electrodes offer the opportunity to increase the device efficiency (both OLED and OSC) by choosing proper periodicity and material. It has also been demonstrated that the transparent metal electrode could be fabricated with low-cost and high-throughput by choosing cheap material and fabrication processes such as roll-to-roll processing. As an application of the transparent metal electrode, OLEDs and OSCs were fabricated using transparent metal electrode as a TCE. The fabricated OLEDs showed a similar electrical characteristic to ITO device. The optical characteristic need to be studied further but the electroluminescence form metal electrode device was observed similar to that of the ITO device to naked eye. The fabricated OSC also showed similar characteristics to the ITO device when the highly transparent metal electrode was used. By choosing the proper material and periodicity which can excite the surface plasmon resonance, the power conversion efficiency (PCE) was enhanced as much as 35 % compared to the ITO device. Therefore, the use of transparent metal electrodes as a TCE instead of ITO could help to realize low cost, large area, flexible organic optoelectronic devices such as OSCs and OLEDs.

8.2 Summary of specific achievements

The transparent metal electrode is in the form of a periodically nanopatterned dense metal mesh film on substrates such as glass. Such structures are fabricated using conventional nonoimprint lithography (NIL). To realize the transparent metal electrode using NIL, a simple technique involving NIL, shadow evaporation, wet chemical etching was developed, which allows nanoscale grating structures with varied line-width to be fabricated while keeping the same period. Using the technique developed, a highly

transparent metal electrode was demonstrated. The highest average transmittance of approximately 84 %, comparable to that of ITO, was achieved for the Au electrode. The sheet resistance about 5 $\Omega/\square$ was also achieved by doubling the metal thickness (from 40 nm to 80 nm) with minimal decrease of the transmittance.

NIL, the lithographic technique used for the fabrication of the transparent metal electrode on the glass substrate, is not compatible with flexible substrates due to the requirement of high pressure and high temperature. To solve this problem, another lithography technique based on metal transfer printing from a flexible PDMS stamp was developed. A highly transparent Cu electrode on a PET substrate using the developed patterning technique was successfully demonstrated. It is much more flexible than ITO, showing that it can be bent down to a radius of about 3 mm with no indication of conductance degradation. On the other hand, the ITO conductance started to decrease at a radius of ~20 mm. As a demonstration, large area Au nanogratings were fabricated using R2RNIL process, which indicates that developed transparent metal electrode could help to realize low cost, large area flexible organic optoelectronic devices such as OSCs and OLEDs.

Metal transfer printing was further developed to be used as another versatile lithography technique in which the transferred metal acts as an etch mask for pattern transfer to the substrate. High transparency metal electrodes were demonstrated by using this technique. The technique developed offers not only the fabrication of transparent metal grating patterns but also the fabrication of various nanoscale metal particles such as squares, diamonds, and nanobars which are a useful platform for biosensor applications. Moreover, it was demonstrated that the minimum feature can be controlled by employing

shadow evaporation. The pattern line-width was reduced down to 50 nm from the original 100 nm line pattern.

OLEDs were demonstrated using transparent Cu electrodes as a TCE. The electrical characteristic of the fabricated OLED is similar to that of the OLED using the ITO with a turn-on voltage of around 5V. Flexible OLED was also demonstrated.

OSCs were demonstrated using transparent metal (Au, Ag, and Cu) electrodes as a TCE on both hard (glass) and soft (PET) substrates. The characteristics such as Voc, Jsc, FF, and PCE are comparable to those of the ITO device when high transparency metal electrodes on glass substrates were used. The analysis about carrier transport in the transparent metal electrode together with the conductive polymer, PEDOT:PSS, suggested that the periodically nanopatterned metal mesh electrode could be effectively treated as a uniform film. Therefore, the opening area in the transparent metal mesh electrode has no effect on the device performance.

OSCs were demonstrated with a periodic (220 nm) Ag grating electrode, acting as not only a transparent electrode but also the excitation source of the surface plamon resonance (SPR). The absolute PCE enhancement of about 35% for the device with a Ag electrode relative to the ITO device was achieved. The PCEs of the Ag device and the ITO device are 1.32 % and 0.97 %, respectively, for the same thickness of the organic layer (80 nm). It was demonstrated that the SPR enhanced the external quantum efficiency (EQE) by about 2.5 times for the Ag device compared to the ITO device at a wavelength of around 570 nm for a 80 nm thick organic layer. The experimental results suggested that higher enhancement would be possible for a thinner organic layer.

8.3 Future works

8.3.1 Organic light emitting diodes (OLEDs) using transparent metal electrodes

We have demonstrated OLEDs using transparent Cu electrodes and done the preliminary evaluation for electrical and optical characteristics. To determine whether transparent metal electrodes can replace conventional ITO electrode for OLED applications, more quantitative analyses such as luminescence-current-voltage (L-I-V) characteristic and EQE are needed. The developed transparent metal electrode is very promising for increasing EQE. Nanostructured metal electrodes can effectively prevent the wave-guiding effect encountered in devices using ITO electrode that results from its high refractive index, and thus increase the light out-coupling efficiency. Moreover, the output efficiency of OLEDs can be further enhanced by forming two-dimensional hole-arrays with proper periodicity. For this work, a thorough analysis which can predict the proper dimensions of the electrode is needed. There is one potential issue that needs to be solved in using metal mesh electrodes for OLED applications. Other than OSCs, OLEDs operate at relatively a high voltage regime with high current. Because current is injected from the metal mesh electrode which occupies less than 20 % of the device area, current crowding can cause device failure. Current crowding is related to the conductivity of the conductive polymer layer, normally PEDOT:PSS and the period of the metal grating. Therefore, an analysis which can determine proper period of the metal grating at a certain conductivity of the PEDOT layer is also needed.

8.3.2 Surface plasmon resonance (SPR) enhanced absorption and

efficiency of organic solar cells (OSCs)

We have demonstrated organic solar cells with periodic (220 nm) Ag gratings and achieved 35 % PCE enhancement compared to the device with the ITO electrode. The increase of the PCE is attributed to the SPR in the Ag grating structure. The SPR enhanced the light field inside the structure and thus the absorption efficiency. The short circuit current (Jsc) was then enhanced accordingly which led to the increase of the PCE. The achieved 2.5 fold enhancement of the EQE is at the wavelength of around 570 nm. The experimental results have shown that there is still some chance that the PCE can be increased by using a thinner organic layer. The EQE enhancement factor in Fig. 7-13 shows the enhanced EQE for most of the visible range as the thickness of the organic layer decreases. However, the EQE did not increase for the wavelength region shorter than 470 nm, but for higher efficiency than that achieved, we also have to utilize those wavelengths region. As shown in Fig.7-17, the surface plasmon still excites the concentrated field in the device structure in the shorter wavelength region, but it is much weaker than that in other regions. Thus, simulations were performed to check whether the field intensity at shorter wavelengths changes as the thickness of the organic layer decreases. Fig. 8-1 shows the simulated field profile inside the Ag device at a wavelength of 400 nm.
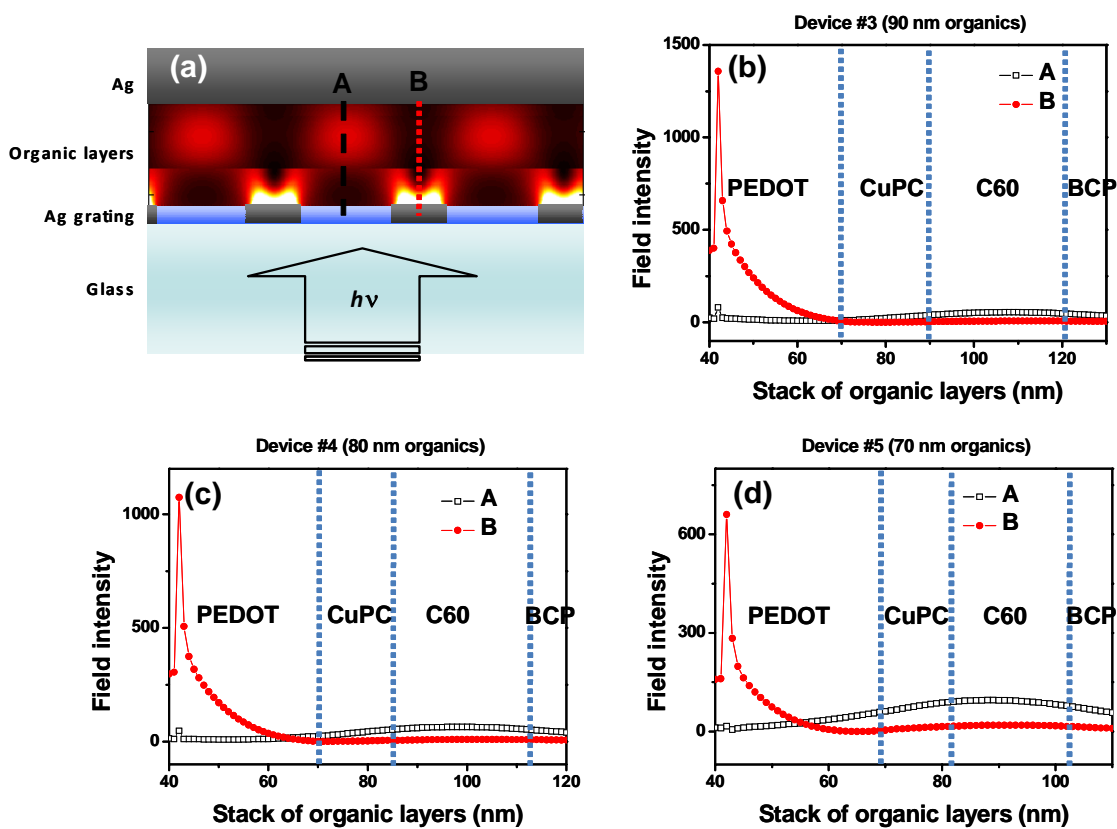
Figure 8-1 (a) Simulated field profile inside the Ag device at a wavelength of 400 nm and the vertical field profile on top of the Ag grating (B) and PEDOT layer (A) for the Ag device with organics layer thickness of (b) 90 nm, (c) 80 nm, and (d) 70 nm.

As shown in Fig. 8-1, there is high field intensity on top of the Ag grating and it decays rapidly (field profile along B). Most of the field is concentrated inside the PEDOT layer. The field profile along A (on top of PEDOT layer) is different from that along B (on top of Ag grating) and its intensity inside the light absorbing organic layer (CuPc and C60) is getting stronger as the total organic layer thickness decreases. Therefore, based on this simulation, we need thinner PEDOT than the 30 nm used in this work as well as thinner total organic layer for further enhancement of the PCE.

Other than this, there is another possibility for PCE enhancement based on the

EQE curve shown in Fig. 7-13. The maximum enhancement occurs at a wavelength of around 570 nm. Below 570 nm the enhancement drops to 1 at a wavelength of about 470 nm. Above 570 nm the enhancement drops and saturates to about 1.3 fold until the wavelength of 800 nm. If we consider the absorption spectra of the material used (C60 and CuPc) as shown in Fig. 8-2, there are two strong absorption peaks at wavelengths of around 470 nm and 620 nm, which correspond to the absorption of C60 and CuPc, respectively.
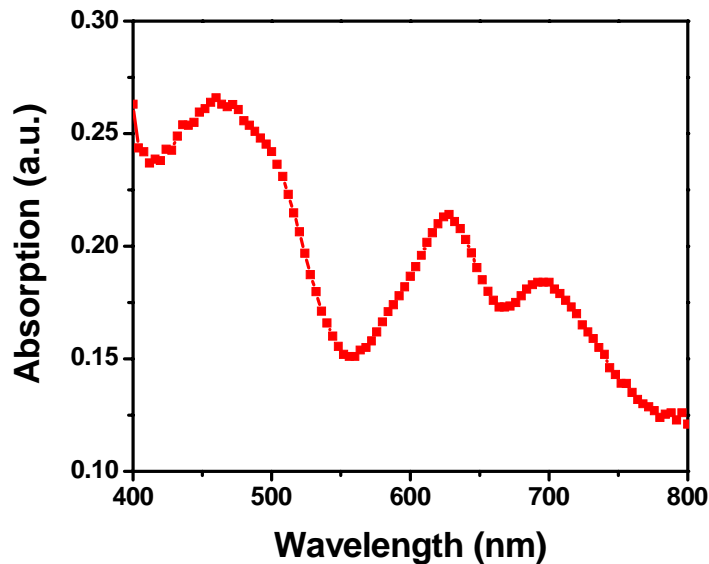
Figure 8-2 Absorption spectra of the C60 and CuPc used for the fabrication of the organic solar cell. The peaks at 470 nm and 620 nm correspond to the absorption of C60 and CuPc, respectively.

The absorption of the organic material used at 570 nm where EQE enhancement occurs is very low. Thus, the device fabricated in this work did not fully utilize the absorption of the material. Even though we could not utilize the absorption of the material using SPR, we achieved 35 % PCE enhancement. This indicated that once we

match the EQE enhancement to the absorption peak of the organic materials we can achieve PCE enhancement greater than 35 %. This can be done by using different organic materials which have an absorption peak at 570 nm or by using a different period of grating which will have EQE enhancement at wavelengths other than 570 nm. In case of the Ag grating period change, more simulation works are needed to find the optimum period of grating which allows the EQE enhancement to be matched with the absorption of the materials used.

Bibliography

[1]   C. W. Tang and S. A. VanSlyke, "Organic electroluminescent diodes," *Appl. Phys. Lett.,* vol. 51, p. 913, 1987.

[2]   J. H. Burroughes, D. D. C. Bradley, A. R. Brown, R. N. Marks, K. Mackay, R. H. Friend, P. L. Burns, and A. B. Holmes, "Light-emitting diodes based on conjugated polymers," *Nature,* vol. 347, p. 539, 1990.

[3]   P. E. Burrows, G. Gu, V. Bulovic, Z. Shen, S. R. Forrest, and M. E. Thompson, "Achieving full-color organic light-emitting devices for lightweight, flat-panel displays," *IEEE Transactions on Electron Devices,* vol. 44, p. 1188, 1997.

[4]   H. H. a. N. S. Sariciftci, "Organic solar cells: An overview," *J. Mater. Res.,* vol. **19**, p. 1924, 2004.

[5]   S. K. Park, J. I. Han, W. K. Kim, and M. G. Kwak, "Deposition of indium-tin-oxide films on polymer substrates for application in plastic-based flat panel displays," *Thin Solid Films,* vol. 397, p. 49, 2001.

[6]   F. L. Wong, M. K. Fung, S. W. Tong, C. S. Lee, and S. T. Lee, "Flexible organic light-emitting device based on magnetron sputtered indium-tin-oxide on plastic substrate," *Thin Solid Films,* vol. 466, p. 225, 2004.

[7]   J. Szczyrbowski, A. Dietrich, and H. Hoffmann, "Optical and electrical properties of RF-sputtered indium-tin oxide films," *Phys. Stat. Sol. A,* vol. 78, p. 243, 1983.

[8]   K. Sreenivas, T. S. Rao, A. Mansingh, and S. Chandra, "Preparation and characterization of rf sputtered indium tin oxide films," *J. Appl. Phys.,* vol. 57, p. 384, 1985.

[9]   M. Higuchi, S. Uekusa, R. Nakano, and K. Yokogawa, "Postdeposition Annealing Influence on Sputtered Indium Tin Oxide Film Characteristics," *Jpn. J. Appl. Phys.,* vol. 1, p. 302, 1994.

[10]   J. R. Sheats and D. B. Roitman, "Failure modes in polymer-based light-emitting diodes," *Synth. Met.,* vol. 95, p. 79, 1998.

[11]   M. P. De Jong, D. P. L. Simons, M. A. Reijme, L. J. van Ijzendoorn, A. W. Denier van der Gon, M. J. A. de Voigt, H. H. Brongersma, and R. W. Gymer, "Indium diffusion in model polymer light-emitting diodes," *Synth. Met.,* vol. 110, p. 1,

2000.

[12] H. Kim, A. Pique, J. S. Horwitz, H. Mattoussi, H. Murata, Z. H. Kafafi, and D. B. Chrisey, "Indium tin oxide thin films for organic light-emitting devices," *Appl. Phys. Lett.,* vol. 74, p. 3444, 1999.

[13] J. S. Kim, M. Granstrom, R. H. Friend, N. Johansson, W. R. Salaneck, R. Daik, W. J. Feast, and F. Cacialli, "Indium--tin oxide treatments for single- and double-layer polymeric light-emitting diodes: The relation between the anode physical, chemical, and morphological properties and the device performance," *J. Appl. Phys.,* vol. 84, p. 6859, 1998.

[14] K. Lin, R. S. Kumar, C. Peng, S. Lu, C. Soo-Jin, and A. P. Burden, "Au-ITO anode for efficient polymer light-emitting device operation," *IEEE Photonics Technol. Lett.,* vol. 17, p. 543, 2005.

[15] G. Gu and S. R. Forrest, "Design of flat-panel displays based on organic light-emitting devices," *IEEE J. Sel. Top. Quantum Electron.,* vol. 4, p. 83, 1998.

[16] W. S. Jahng, A. H. Francis, H. Moon, J. I. Nanos, and M. D. Curtis, "Is indium tin oxide a suitable electrode in organic solar cells? Photovoltaic properties of interfaces in organic p/n junction photodiodes," *Appl. Phys. Lett.,* vol. 88, p. 093504, 2006.

[17] Z. Chen, B. Cotterell, W. Wang, E. Guenther, and S.-J. Chua, "A mechanical assessment of flexible optoelectronic devices," *Thin Solid Films,* vol. 394, p. 202, 2001.

[18] A. Andersson, N. Johansson, P. Bröms, N. Yu, D. Lupo, and W. R. Salaneck, "Fluorine Tin Oxide as an Alternative to Indium Tin Oxide in Polymer LEDs," *Adv. Mater.,* vol. 10, p. 859, 1998.

[19] F. Yang and S. R. Forrest, "Organic Solar Cells Using Transparent SnO2-F Anodes," *Adv. Mater.,* vol. 18, p. 2018, 2006.

[20] B. O'Regan and M. Grätzel, "A low-cost, high-efficiency solar cell based on dye-sensitized colloidal TiO2 films," *Nature,* vol. 353, p. 737, 1991.

[21] X. Jiang, F. L. Wong, M. K. Fung, and S. T. Lee, "Aluminum-doped zinc oxide films as transparent conductive electrode for organic light-emitting devices," *Appl. Phys. Lett.,* vol. 83, p. 1875, 2003.

[22] H. Kim, C. M. Gilmore, J. S. Horwitz, A. Pique, H. Murata, G. P. Kushto, R. Schlaf, Z. H. Kafafi, and D. B. Chrisey, "Transparent conducting aluminum-doped zinc oxide thin films for organic light-emitting devices," *Appl. Phys. Lett.,* vol. 76, p. 259, 2000.

[23] T. Minami, "Transparent conducting oxide semiconductors for transparent

electrodes," *Semicond. Sci. Technol.,* vol. 20, p. S35, 2005.

[24]   S. Iijima, "Helical microtubules of graphitic carbon," *Nature,* vol. 354, p. 56, 1991.

[25]   R. H. Baughman, A. A. Zakhidov, and W. A. de Heer, "Carbon Nanotubes--the Route Toward Applications," *Science,* vol. 297, p. 787, 2002.

[26]   V. N. Popov, "Carbon nanotubes: properties and application," *Materials Science and Engineering: R: Reports,* vol. 43, p. 61, 2004.

[27]   Z. Wu, Z. Chen, X. Du, J. M. Logan, J. Sippel, M. Nikolou, K. Kamaras, J. R. Reynolds, D. B. Tanner, A. F. Hebard, and A. G. Rinzler, "Transparent, Conductive Carbon Nanotube Films," *Science,* vol. 305, p. 1273, 2004.

[28]   D. Tasis, N. Tagmatarchis, A. Bianco, and M. Prato, "Chemistry of Carbon Nanotubes," *Chemical Reviews,* vol. 106, p. 1105, 2006.

[29]   J. van de Lagemaat, T. M. Barnes, G. Rumbles, S. E. Shaheen, T. J. Coutts, C. Weeks, I. Levitsky, J. Peltola, and P. Glatkowski, "Organic solar cells with carbon nanotubes replacing In[sub 2]O[sub 3]:Sn as the transparent electrode," *Appl. Phys. Lett.,* vol. 88, p. 233503, 2006.

[30]   M. A. T. M. W. Rowell, M. D. McGehee, H.-J. Prall, G. Dennler, N. S. Sariciftci, L. Hu, and G. Gruner, "Organic solar cells with carbon nanotube network electrodes," *Appl. Phys. Lett.,* vol. 88, p. 233506, 2006.

[31]   C. J. Lee, R. B. Pode, D. G. Moon, and J. I. Han, "Realization of an efficient top emission organic light-emitting device with novel electrodes," *Thin Solid Films,* vol. 467, p. 201, 2004.

[32]   Q. Chengfeng, P. Huajun, C. Haiying, X. Zhiliang, W. Man, and K. Hoi Sing, "Top-emitting OLED using praseodymium oxide coated platinum as hole injectors," *IEEE Transactions on Electron Devices,* vol. 51, p. 1207, 2004.

[33]   Z. Wu, S. Chen, H. Yang, Y. Zhao, J. Hou, and S. Liu, "Top-emitting organic light-emitting devices based on silicon substrate using Ag electrode," *Semicond. Sci. Technol.,* vol. 19, p. 1138, 2004.

[34]   H. Peng, X. Zhu, J. Sun, Z. Xie, S. Xie, M. Wong, and H.-S. Kwok, "Efficient organic light-emitting diode using semitransparent silver as anode," *Appl. Phys. Lett.,* vol. 87, p. 173505, 2005.

[35]   M.-G. Kang and L. J. Guo, "Nanoimprinted Semitransparent Metal Electrodes and Their Application in Organic Light Emitting Diodes," *Adv. Mater.,* vol. 19, p. 1391, 2007.

[36]   L. J. Guo, "Nanoimprint Lithography: Methods and Material Requirements," *Adv. Mater.,* vol. 19, p. 495, 2007.

[37]   M.-G. Kang, M.-S. Kim, J. Kim, and L. J. Guo, "Organic Solar Cells Using

Nanoimprinted Transprent Metal Electrodes," *Adv. Mater.,* vol. 20, p. 4408, 2008.

[38]   S. Y. Chou, P. R. Krauss, and P. J. Renstrom, "Imprint Lithography with 25-Nanometer Resolution," *Science,* vol. 272, p. 85, 1996.

[39]   http://www.gsolver.com/.

[40]   C. W. Tang, "Two-layer organic photovoltaic cell," *Appl. Phys. Lett.,* vol. 48, p. 183, 1986.

[41]   P. Peumans, A. Yakimov, and S. R. Forrest, "Small molecular weight organic thin-film photodetectors and solar cells," *J. Appl. Phys.,* vol. 93, p. 3693, 2003.

[42]   K. M. Coakley and M. D. McGehee, "Conjugated Polymer Photovoltaic Cells," *Chem. Mater.,* vol. 16, p. 4533, 2004.

[43]   G. Yu, J. Gao, J. C. Hummelen, F. Wudl, and A. J. Heeger, "Polymer Photovoltaic Cells: Enhanced Efficiencies via a Network of Internal Donor-Acceptor Heterojunctions," *Science,* vol. 270, p. 1789, 1995.

[44]   W.-F. Wu and B.-S. Chiou, "Deposition of indium tin oxide films on polycarbonate substrates by radio-frequency magnetron sputtering," *Thin Solid Films,* vol. 298, p. 221, 1997.

[45]   S. Yamamoto, T. Yamanaka, and Z. Ueda, "Properties of Sn-doped In[sub 2]O[sub 3] by reactive magnetron sputtering and subsequent annealing," *J. Vac. Sci. Technol. A,* vol. 5, p. 1952, 1987.

[46]   B. Maennig, J. Drechsel, D. Gebeyehu, P. Simon, F. Kozlowski, A. Werner, F. Li, S. Grundmann, S. Sonntag, M. Koch, K. Leo, M. Pfeiffer, H. Hoppe, D. Meissner, N. S. Sariciftci, I. Riedel, V. Dyakonov, and J. Parisi, "Organic p-i- n solar cells," *Appl. Phys. A,* vol. 79, p. 1, 2004.

[47]   M.-G. Kang and L. J. Guo, "Semitransparent Cu electrode on a flexible substrate and its application in organic light emitting diodes," *J. Vac. Sci. Technol. B,* vol. 25, p. 2637, 2007.

[48]   Y.-L. Loo, R. L. Willett, K. W. Baldwin, and J. A. Rogers, "Additive, nanoscale patterning of metal films with a stamp and a surface chemistry mediated transfer process," *Appl. Phys. Lett.,* vol. 81, p. 562, 2003.

[49]   D.-Y. K. S.-H. Hur, C. Kocabas, J. A. Rogers, "Nanotransfer printing by use of noncovalent surface forces," *Appl. Phys. Lett.,* vol. 83, p. 5730, 2004.

[50]   D. W. V. Krevelen, *Properties of Polymers*. Amsterdam: Elsevier, 1997.

[51]   C. Pina-Hernandez, J.-S. Kim, L. J. Guo, and P.-F. Fu, "High-Throughput and Etch-Selective Nanoimprinting and Stamping Based on Fast-Thermal-Curing Poly(dimethylsiloxane)s," *Adv. Mater.,* vol. 19, p. 1222, 2007.

[52]   W. T. S. Huck, N. Bowden, P. Onck, T. Pardoen, J. W. Hutchinson, and G. M.

Whitesides, "Ordering of Spontaneously Formed Buckles on Planar Surfaces," *Langmuir,* vol. 16, p. 3497, 2000.

[53]   S. H. Ahn and L. J. Guo, "High-Speed Roll-to-Roll Nanoimprint Lithography on Flexible Plastic Substrates," *Adv. Mater.,* vol. 20, p. 2044, 2008.

[54]   S. H. Ahn and L. J. Guo, "Large-Area Roll-to-Roll and Roll-to-Plate Nanoimprint Lithography: A Step toward High-Throughput Application of Continuous Nanoimprinting," *ACS Nano,* 2009.

[55]   B. D. Lucas, J.-S. Kim, C. Chin, and L. J. Guo, "Nanoimprint Lithography Based Approach for the Fabrication of Large-Area, Uniformly Oriented Plasmonic Arrays," *Adv. Mater.,* vol. 20, p. 1129, 2008.

[56]   Y. Xia and G. M. Whitesides, "Soft Lithography," *Annu. Rev. Mater. Sci.,* vol. 28, p. 153, 1998.

[57]   A. Kumar, H. Biebuyck, and G. M. Whitesides, "Patterning Self-Assembled Monolayers: Applications in Materials Science," *Langmuir,* vol. 10, p. 1498, 1994.

[58]   Y. Xia, X.-M. Zhao, E. Kim, and G. M. Whitesides, "A Selective Etching Solution for Use with Patterened Self-Assembled Monolayers of Alkanethiolates on Gold," *Chem. Mater.,* vol. 7, p. 2332, 1995.

[59]   T. Li, Z. Huang, Z. Suo, S. P. Lacour, and S. Wagner, "Stretchability of thin metal films on elastomer substrates," *Appl. Phys. Lett.,* vol. 85, p. 3435, 2004.

[60]   L. J. G. Xing Cheng, "One-step lithography for various size patterns with a hybrid mask-mold," *Microelectron. Eng,* vol. 71, p. 288, 2004.

[61]   Y. D. Jin, X. B. Ding, J. Reynaert, V. I. Arkhipov, G. Borghs, P. L. Heremans, and M. Van der Auweraer, "Role of LiF in polymer light-emitting diodes with LiF-modified cathodes," *Organic Electronics,* vol. 5, p. 271, 2004.

[62]   V. Adamovich, A. Shoustikov, and M. E. Thompson, "TiN as an Anode Material for Organic Light-Emitting Diodes," *Adv. Mater.,* vol. 11, p. 727, 1999.

[63]   J. Cui, A. Wang, N. L. Edleman, J. Ni, P. Lee, N. R. Armstrong, and T. J. Marks, "Indium Tin Oxide Alternatives-High Work Function Transparent Conducting Oxides as Anodes for Organic Light-Emitting Diodes," *Adv. Mater.,* vol. 13, p. 1476, 2001.

[64]   K. Lee, Z. Wu, Z. Chen, F. Ren, S. J. Pearton, and A. G. Rinzler, "Single Wall Carbon Nanotubes for p-Type Ohmic Contacts to GaN Light-Emitting Diodes," *Nano Lett.,* vol. 4, p. 911, 2004.

[65]   J.-S. Kim, P. K. H. Ho, N. C. Greenham, and R. H. Friend, "Electroluminescence emission pattern of organic light-emitting diodes: Implications for device efficiency calculations," *J. Appl. Phys.,* vol. 88, p. 1073, 2000.

[66] C. Liu, V. Kamaev, and Z. V. Vardeny, "Efficiency enhancement of an organic light-emitting diode with a cathode forming two-dimensional periodic hole array," *Appl. Phys. Lett.,* vol. 86, p. 14301, 2005.

[67] J.M. Ziebarth, A. K Saafir, S. Fan, and M. D. McGehee, "Extracting Light from Polymer Light-Emitting Diodes Using Stamped Bragg Gratings," *Adv. Funct. Mater.,* vol. 14, p. 451, 2004.

[68] S. Sohn, K. Park, D. Lee, D. Jung, H. M. Kim, U. Manna, J. Yi, J. Boo, H. Chae, and H. Kim, "Characteristics of Polymer Light Emitting Diodes with the LiF Anode Interfacial Layer," *J.J. Appl. Phys.,* vol. 45, p. 3733, 2006.

[69] C. Stephane, P. Fabrice, T. Roland, and P. Jean-Luc, "Efficient light absorption in metal--semiconductor--metal nanostructures," *Appl. Phys. Lett.,* vol. 85, p. 194, 2004.

[70] J. Y. Kim, K. Lee, N. E. Coates, D. Moses, T.-Q. Nguyen, M. Dante, and A. J. Heeger, "Efficient Tandem Polymer Solar Cells Fabricated by All-Solution Processing," *Science,* vol. 317, p. 222, 2007.

[71] G. Li, V. Shrotriya, J. Huang, Y. Yao, T. Moriarty, K. Emery, and Y. Yang, "High-efficiency solution processable polymer photovoltaic cells by self-organization of polymer blends," *Nature Mater.,* vol. 4, p. 864, 2005.

[72] G. Li, V. shrotriya, Y. Yao, and Y. Yang, "Investigation of annealing effects and film thickness dependence of polymer solar cells based on poly(3-hexylthiophene)," *J. Appl. Phys.,* vol. 98, p. 043704, 2005.

[73] W. Ma, C. Yang, X. Gong, K. Lee, and A. J. Heeger, "Thermally Stable, Efficient Polymer Solar Cells with Nanoscale Control of the Interpenetrating Network Morphology," *Adv. Funct. Mater.,* vol. 15, p. 1617, 2005.

[74] A. J. Anthony, R. A. Hatton, G. Y. Chen, and S. R. P. Silva, "Carbon nanotubes grown on In[sub 2]O[sub 3]:Sn glass as large area electrodes for organic photovoltaics," *Appl. Phys. Lett.,* vol. 90, p. 023105, 2007.

[75] A. J. Miller, R. A. Hatton, and S. R. P. Silva, "Interpenetrating multiwall carbon nanotube electrodes for organic solar cells," *Appl. Phys. Lett.,* vol. 89, p. 133117, 2006.

[76] K. Tvingstedt and O. Inganäs, "Electrode Grids for ITO Free Organic Photovoltaic Devices," *Adv. Mater.,* vol. 19, p. 2893, 2007.

[77] J.-Y. Lee, S. T. Connor, Y. Cui, and P. Peumans, "Solution-Processed Metal Nanowire Mesh Transparent Electrodes," *Nano Lett.,* vol. 8, p. 689, 2008.

[78] L. S. Roman, O. Inganäs, T. Granlund, T. Nyberg, M. Svensson, M. R. Andersson, and J. C. Hummelen, "Trapping Light in Polymer Photodiodes with Soft

Embossed Gratings," *Adv. Mater.,* vol. 12, p. 189, 2000.

[79]   S.-I. Na, S.-S. Kim, S.-S. Kwon, J. Jo, J. Kim, T. Lee, and D.-Y. Kim, "Surface relief gratings on poly(3-hexylthiophene) and fullerene blends for efficient organic solar cells," *Appl. Phys. Lett.,* vol. 91, p. 173509, 2007.

[80]   C. Cocoyer, L. Rocha, L. Sicot, B. Geffroy, R. de Bettignies, C. Sentein, C. Fiorini-Debuisschert, and P. Raimond, "Implementation of submicrometric periodic surface structures toward improvement of organic-solar-cell performances," *Appl. Phys. Lett.,* vol. 88, p. 133108, 2006.

[81]   M.-S. Kim, J.-S. Kim, J. C. Cho, M. Shtein, L. J. Guo, and J. Kim, "Flexible conjugated polymer photovoltaic cells with controlled heterojunctions fabricated using nanoimprint lithography," *Appl. Phys. Lett.,* vol. 90, p. 123113, 2007.

[82]   A. Cravino, P. Schilinsky, and C. J. Brabec, "Characterization of Organic Solar Cells: the Importance of Device Layout," *Adv. Funct. Mater.,* vol. 17, p. 3906, 2007.

[83]   M.-S. Kim, M.-G. Kang, L. J. Guo, and J. Kim, "Choice of electrode geometry for accurate measurement of organic photovoltaic cell performance," *Appl. Phys. Lett.,* vol. 92, p. 133301, 2008.

[84]   V. D. Mihailetchi, L. J. A. Koster, and P. W. M. Blom, "Effect of metal electrodes on the performance of polymer:fullerene bulk heterojunction solar cells," *Appl. Phys. Lett.,* vol. 85, p. 970, 2004.

[85]   S. H. Park, A. Roy, S. Beaupre, S. Cho, N. Coates, J. S. Moon, D. Moses, M. Leclerc, K. Lee, and A. J. Heeger, "Bulk heterojunction solar cells with internal quantum efficiency approaching 100%," *Nature Photon.,* vol. 3, p. 297, 2009.

[86]   G. Li, V. Shrotriya, Y. Yao, J. Huang, and Y. Yang, "Manipulating regioregular poly(3-hexylthiophene) : [6,6]-phenyl-C61-butyric acid methyl ester blends--route towards high efficiency polymer solar cells," *J. Mater. Chem.,* vol. 17, p. 3126, 2007.

[87]   P. W. M. Blom, V. D. Mihailetchi, L. J. A. Koster, and D. E. Markov, "Device Physics of Polymer:Fullerene Bulk Heterojunction Solar Cells," *Adv. Mater.,* vol. 19, p. 1551, 2007.

[88]   S.-B. Rim, S. Zhao, S. R. Scully, M. D. McGehee, and P. Peumans, "An effective light trapping configuration for thin-film solar cells," *Applied Physics Letters,* vol. 91, p. 243501, 2007.

[89]   D.-H. Ko, J. R. Tumbleston, L. Zhang, S. Williams, J. M. DeSimone, R. Lopez, and E. T. Samulski, "Photonic Crystal Geometry for Organic Solar Cells," *Nano Letters,* vol. 9, p. 2742, 2009.

[90]   P. R. Barry, P. Peter, and R. F. Stephen, "Long-range absorption enhancement in organic tandem thin-film solar cells containing silver nanoclusters," *J. Appl. Phys.,* vol. 96, p. 7519, 2004.

[91]   T. D. Heidel, J. K. Mapel, M. Singh, K. Celebi, and M. A. Baldo, "Surface plasmon polariton mediated energy transfer in organic photovoltaic devices," *Appl. Phys. Lett.,* vol. 91, p. 093506, 2007.

[92]   J. K. Mapel, M. Singh, M. A. Baldo, and K. Celebi, "Plasmonic excitation of organic double heterostructure solar cells," *Appl. Phys. Lett.,* vol. 90, p. 121102, 2007.

[93]   A. J. Morfa, K. L. Rowlen, T. H. Reilly III, M. J. Romero, and J. van de Lagemaat, "Plasmon-enhanced solar energy conversion in organic bulk heterojunction photovoltaics," *Appl. Phys. Lett.,* vol. 92, p. 013504, 2008.

[94]   S.-S. Kim, S.-In. Na, J. Jo, D.-Yu. Kim, and Y.-C. Nah, "Plasmon enhanced performance of organic solar cells using electrodeposited Ag nanoparticles," *Appl. Phys. Lett.,* vol. 93, p. 073307, 2008.

[95]   T. H. Reilly III, J. van de Lagemaat, R. C. Tenent, A. J. Morfa, and K. L. Rowlen, "Surface-plasmon enhanced transparent electrodes in organic photovoltaics," *Appl. Phys. Lett.,* vol. 92, p. 243304, 2008.

[96]   N. C. Lindquist, W. A. Luhman, S.-H. Oh, and R. J. Homes, "Plasmonic nanocavity arrays for enhanced efficiency in organic photovoltaic cells," *Appl. Phys. Lett.,* vol. 93, p. 123308, 2008.

[97]   W. N. Willie, H. Chi-Shain, and A. Yariv, "Holographic interference lithography for integrated optics," *Electron Devices, IEEE Transactions on,* vol. 25, p. 1193, 1978.